



저작자표시-비영리-변경금지 2.0 대한민국

이용자는 아래의 조건을 따르는 경우에 한하여 자유롭게

- 이 저작물을 복제, 배포, 전송, 전시, 공연 및 방송할 수 있습니다.

다음과 같은 조건을 따라야 합니다:



저작자표시. 귀하는 원저작자를 표시하여야 합니다.



비영리. 귀하는 이 저작물을 영리 목적으로 이용할 수 없습니다.



변경금지. 귀하는 이 저작물을 개작, 변형 또는 가공할 수 없습니다.

- 귀하는, 이 저작물의 재이용이나 배포의 경우, 이 저작물에 적용된 이용허락조건을 명확하게 나타내어야 합니다.
- 저작권자로부터 별도의 허가를 받으면 이러한 조건들은 적용되지 않습니다.

저작권법에 따른 이용자의 권리는 위의 내용에 의하여 영향을 받지 않습니다.

이것은 [이용허락규약\(Legal Code\)](#)을 이해하기 쉽게 요약한 것입니다.

[Disclaimer](#)

공학박사학위논문

삼성분계 산화물에서의 전기장에 의한 현상

동역학적 조성분리, 상분리 그리고 형성반응

**Electric Field-induced Processes in Ternary Oxides
- Kinetic Unmixing, Decomposition and Formation**

2015 년 8 월

서울대학교 대학원

재료공학부

전 자 규

Ph. D dissertation

Electric Field-induced Processes in Ternary Oxides

- Kinetic Unmixing, Decomposition and Formation

삼성분계 산화물에서의 전기장에 의한 현상
동역학적 조성분리, 상분리 그리고 형성반응

August, 2015

Seoul National University

Department of Materials Science and Engineering

Jakyu Chun

Abstract

When a multicomponent material such as ternary oxides, which are used throughout the industry in the form of solid oxide fuel cells, multilayered ceramic capacitors, thermoelectrics and so on, are put under working conditions (i.e. under driving forces) degradative phenomena of kinetic unmixing and/or decomposition arises. These phenomena have their origin in the difference of diffusion coefficient (or mobility) of the constituent *cations*. Even if the compound is in its thermodynamically stable regime, this type of unmixing and decomposition may still occur, regardless of the compound being an electrolyte or a semiconductor. As it is caused by the diffusion coefficient difference, the phenomena are termed "kinetic."

Many works have been done for kinetic unmixing under P_{O_2} gradient. Fewer works have been done for kinetic decomposition under P_{O_2} gradient and unmixing under electric field. No literature reports results for kinetic decomposition under electric field. Work by Yoo et al. on $BaTiO_3$ showed neither unmixing nor decomposition even when large electric field was applied. One must therefore wonder (i) whether kinetic unmixing and decomposition occur under electric field and (ii) if they occur, would they occur always; or is there a certain threshold for these phenomena to occur. This kind of analysis was never done under electric field. Also, electric field does not affect only these reactions. Rather, it can affect other reactions as well, such as formation reaction, which is the reverse reaction of decomposition, acting as a secondary driving force (the primary driving force being the concentration gradient of a component). The formation kinetics under electric field should also be found.

To answer these questions, a model ternary system was selected. Observations were made on the system $NiTiO_3$, which is the only intermediate compound in the NiO - TiO_2 system at $1300^\circ C$ in air. Constant current was applied to $NiTiO_3$ pellets and the applied current values were converted into applied voltage by conductivity measurement. Different levels of current were applied to the pellets. For specimens

exposed to voltage less than a threshold value, only kinetic unmixing was observed while for pellets exposed to voltage higher than the threshold value both kinetic unmixing and decomposition were observed. The investigation was done by electron probe microanalysis to obtain the concentration profile between the anode and the cathode. X-ray diffraction was also done at the electrodes to check the existence of NiO and TiO₂. Both the EPMA and XRD results confirmed kinetic unmixing and decomposition of NiTiO₃.

The master equation for estimating the threshold voltage (or critical decomposition voltage) U_d is important in estimating the degradative behavior of the compound and is here derived. Two conditions were applied, (i) steady state and (ii) closed circuit condition. The resulting master equation showed that the diffusion coefficient ratio of cations A and B is the critical factor in determining U_d , as expected. To obtain this ratio, a diffusion couple of NiO-TiO₂ was made, meanwhile applying Pt inert markers at the starting interface of NiO/TiO₂. After heat treatment, the ratio of distance from the inert markers to the respective interfaces (NiO/NiTiO₃, NiTiO₃/TiO₂) corresponds to the diffusion coefficient ratio. From this diffusion couple a diffusion coefficient ratio of $D_B/D_A=0.21 \pm 0.07$ was obtained. The range of U_d from the kinetic unmixing/decomposition experiment and the range expected from the master equation coincided within error bounds, indicating that the master equation is indeed valid. Also, the possible reasons for the anomalous behavior of BaTiO₃ mentioned above are suggested.

For the effect of electric field on the formation reaction, the master equation was derived by Korte et al., but experimental confirmation was not given. Therefore in this thesis quantitative analysis of the formation kinetics under electric field and microstructure characteristics are introduced. It is shown that the thickness and microstructure of the system is greatly affected by electric field, a fact which can be used in industries.

Keywords: Kinetic unmixing, Kinetic decomposition, Cation mobility (diffusion

coefficient) ratio, Decomposition voltage, Ternary ABO_3 compounds, Electric field,
Formation reaction

Student ID: 2008-20680

Table of contents

List of Figures	i
List of Tables	xi
List of Symbols	xii
1. Introduction	1
2. Literature survey	7
(1) The definition of kinetic unmixing and decomposition	7
(2) The history of kinetic unmixing and decomposition	20
(a) Chemical potential gradient	20
(b) Electric field	48
(c) Temperature gradient and stress field	62
3. Experimental results on kinetic unmixing, decomposition and solid state reaction (diffusion couples)	64
(1) The literature on the ternary system - NiTiO₃	64
(2) The literature on solid state reaction and inert markers	74
(3) Specimen preparation and experimental results	85
(a) Specimen preparation	85
(b) The total conductivity of NiTiO₃	91
(c) Kinetic unmixing and decomposition in NiTiO₃	91
(d) Solid state reaction of NiO-TiO₂ and inert markers	109

4. Analysis of the experimental results	113
(1) Kinetic decomposition under μ_{O_2} gradient	113
(2) Kinetic decomposition under electric field	121
(a) The Gibbs Theorem – its derivation and limitations	121
(b) Novel derivation of decomposition voltage U_d	128
(3) Solid state reaction (diffusion couple) and inert markers	137
(4) Justification of theory	143
(5) Proposal of effect of thermodynamic factor - BaTiO_3	146
5. The effect of electric field on formation reaction	160
(1) The literature on electric field and formation reaction	160
(2) Theoretical derivation of formation kinetics under electric field	168
(3) Experimental results and discussion	173
6. Summary and future work	184
Reference	187
Appendix	202
Message of Gratitude	223
Abstract (in Korean)	228

List of Figures

Fig. 2-1. Thermodynamic phase diagrams of (a) CoO-MgO[30], (b) CoO-CaO[31] and (c) MgO-NiO[32], all showing complete miscibility of the end members AO-BO.

Fig. 2-2. Thermodynamic phase diagrams of (a) CoO-TiO₂ [28] and (b) Y₂O₃-BeO [29] systems. (a) is the general behavior for heterovalent systems.

Fig. 2-3. Schematic diagram of (a) the $\langle 110 \rangle$ path for migration of B-site Mn and (b) the curved, lower energy path for migration in the direction $\langle 100 \rangle$, shown on the $\{100\}$ plane. From De Souza et al.[34]

Fig. 2-4. Schematic diagram of the progress of kinetic unmixing and decomposition. Large ξ corresponds to complete miscibility of the end members while small ξ corresponds to narrow stability regime of the compound.

Fig. 2-5. Schematic diagram of the ionic movements when kinetic unmixing and/or decomposition occurs, for the case of $b_A > b_B$. (b_k : mechanical mobility of species k) With cation flow, lattice shift or crystal shift occurs along with kinetic unmixing and/or decomposition.

Fig. 2-6. The unmixing result of Schmalzried et al. for the system (Co,Mg)O. From Schmalzried et al. [40]

Fig. 2-7. The experimental unmixing profile for (Ni_{1-x}Ti_{x/2})O with initial concentration of Ti=14 w/o, from Schmalzried and Laqua [43].

Fig. 2-8. The decomposition profiles under P_{O_2} gradient for the systems (a) $NiTiO_3$ and (b) Co_2TiO_4 . From Schmalzried and Laqua [43].

Fig. 2-9. The concentration profile of Mn after exposure of $(Mn_{0.6}Fe_{0.4})_{1-\delta}O$ to P_{O_2} gradients. The high P_{O_2} side (left side) is exposed to air while the low P_{O_2} side differed as follows: (a) $P_{O_2}=3.1 \times 10^{-5}$ atm, 8 hours; (b) $P_{O_2}=1.0 \times 10^{-5}$ atm, 3 hours; (c) $P_{O_2}=1.6 \times 10^{-6}$ atm, 1 hour. (●): spinel; (○): wustite. From Ueshima et al. [46]

Fig. 2-10. Ratio of the demixing parameters κ ($L_{AB} \neq 0$) and κ_0 ($L_{AB} = 0$) as function of x_B for different ratios ω_A / ω_B . From Martin and Schmackpfeffer [48].

Fig. 2-11. The local unmixing ratio, κ , in a heterovalent doped oxide (a) as function of the binding energy ε for $x_B=0.01$ and different ratios ω_0 / ω_2 and (b) as function of the dopant fraction x_B for $\varepsilon=2$ and different ratios ω_0 / ω_2 . From Martin and Schmackpfeffer [48].

Fig. 2-12. Composition profile across the Ni_2SiO_4 disk after kinetic decomposition obtained by EPMA. From Jacob and Shukla [63]. Actual experimental conditions not indicated.

Fig. 2-13. The experimental steady state demixing profiles of (a) fayalite at $1130^\circ C$ and $a''_{O_2} / a'_{O_2} = 390$ and (b) olivine $(Fe_xMg_{1-x})_{2-\delta}SiO_4$ at $1130^\circ C$ and $a''_{O_2} / a'_{O_2} = 150$. From Weghöft and Schmalzried [66].

Fig. 2-14. Multiphase layer formed by exposing a single-phase NiTiO_3 to an oxygen potential gradient between 2.13×10^4 Pa (left) and 7.234 Pa (right) at 1450°C . From Azubike et al. [69]

Fig. 2-15. SEM backscattered image of the (a) high Po_2 side and (b) low Po_2 side of the La_2NiO_4 membrane after annealing at 1000°C for 800 hours. The dark spots in (a) represent the decomposition product NiO . The dark spots in (b) are pores and no phase change was detected. From Cebasek et al. [72]

Fig. 2-16. Schematic illustration of the formation of different zones at the oxygen lean-side of permeated $\text{La}_{0.3}\text{Sr}_{0.7}\text{CoO}_{3-\delta}$ disks. (a) Disk permeated during 120 hours at 900°C in a gradient of air vs. 1.4% O_2 and (b) permeated for more than 500 hours at temperatures $900\sim 1100^\circ\text{C}$. From Van Doorn et al. [74]

Fig. 2-17. The composition profiles of (a) $(\text{Co,Mg})\text{O}$ and (b) YSZ under electric field. From Monceau et al. [82]

Fig. 2-18. Unmixing profile of Co and Ni in $(\text{Co,Ni})\text{O}$ under electric field of 275 mV for 480 hours. Left side is anode and right side is cathode. From Teller and Martin [83].

Fig. 2-19. Unmixing profile of Ga in $(\text{Co,Ga})\text{O}$ at (a) 225 mV and $\bar{z}_B = -0.1$, and (b) 450 mV and $\bar{z}_B = -0.07$. From Teller and Martin [86].

Fig. 2-20. Composition distribution (Mn) vs. relative distance from the cathode to the anode. From Hong and Yoo [87].

Fig. 2-21. (a) The cathode vicinity of La-doped BaTiO₃, after passing 703 C at 1200°C in air. (b) The anode vicinity of La-doped BaTiO₃, after passing 1161 C at 1200°C in air. One can see that in (a) the novel lattice grows around the Pt cathode, while in (b) the Pt anode penetrates into the lattice. From Yoo et al. [26]

Fig. 2-22. (a) The electron probe microanalysis (EPMA) profile showing the distribution of Ba, Ti, O and La as measured from anode to cathode, along the white arrow in Fig. 2-21 (a). (b) The x-ray diffraction pattern obtained from the cathode surface of the oxide in Fig. 2-21. All the peaks are assigned to the perovskite BaTiO₃. There is virtually no gradient in the EPMA profile and no decomposed phase in the XRD pattern. From Yoo et al. [26]

Fig 3-1. The crystal structure of ilmenite FeTiO₃, showing hexagonally close-packed oxygen anions and alternating cation layers filling 2/3 of octahedral sites.

Fig. 3-2. The ilmenite structure as viewed from [0001] direction. The oxygen ions form hexagonally close-packed layer, with cations filling 2/3 of octahedral sites, forming hexagonal rings.

Fig. 3-3. The order parameter η of NiTiO₃ calculated from conductivity data (solid line) and neutron scattering (circles). From Stüber et al. [104]

Fig. 3-4. The high temperature phase diagram of NiO-TiO₂ system. NT resembles the ilmenite NiTiO₃. From Laqua et al. [44]

Fig. 3-5. The compiled values of $-\Delta G_f^\circ$ from literature as function of temperature in NiTiO₃ for the reaction NiO(s)+TiO₂(s)=NiTiO₃(s).

Fig. 3-6. The proposed possible mechanisms of spinel oxide formation. Taken from Schmalzried. [112]

Fig. 3-7. A typical concentration profile according to secondary ion mass spectroscopy. The fluctuating lines represent radioactive Co tracers after various annealing conditions in La₂NiO_{4+δ}. From Cebasek et al. [113]

Fig. 3-8. A sketch of a cross section of a bar-shaped specimen from the paper by Smigelskas and Kirkendall. Taken from Nakajima [116].

Fig. 3-9. The annealing time dependence of the interface shift (the distance between the molybdenum wires on the opposite surfaces). From Nakajima [116].

Fig 3-10. Schematics of the as-constructed (a) unmixing cell involving NiTiO₃ and the (b) as-constructed reaction couple NiO|TiO₂ for NiTiO₃ formation. ××××: platinum gauze; ••••: inert platinum markers; ———: platinum foil.

Fig. 3-11. Optical images of (a) NiO, (b) TiO₂ and (c) NiTiO₃ after thermal etching.

Fig. 3-12. The Arrhenius plot of the total conductivity of NiTiO₃ in air, compared with the literature values reported by Stüber et al. [104]

Fig. 3-13. Temporal variation of the voltage drop between the potential probes,

3.56 mm apart, of the ca. 6.289 mm long, 4-probe specimen $\text{NiTi}_{1+\xi}\text{O}_{3+\delta}$ while passing a constant current 20 mA at 1300°C in air atmosphere which has eventually caused a compositional unmixing $\Delta\xi\approx 0.171$ (shown later). Note that the voltage drop remains unchanged within 0.05 % for ca. 5 hrs.

Fig. 3-14. The scanning electron microscopy images of the (a) overall specimen, (b) the anode and (c) the cathode, for specimen 6 which was put under $I=24.1$ mA for 60 hours at 1300°C. The exploded views of the boxed regions are shown in (b) and (c). The dotted arrows indicate the path in which the electron probe microanalysis was done.

Fig. 3-15. The electron probe microanalysis (EPMA) scan results of the (a) overall specimen, (b) the anode and (c) the cathode, for specimen 6 which was put under $I=24.1$ mA for 60 hours at 1300°C. The scan paths correspond to the dotted arrows in Fig 3-14.

Fig 3-16. The scanning electron microscopy images of the (a) overall specimen, (b) the anode and (c) the cathode, for specimen 1 which was put under $I=546$ mA for 160 minutes at 1300°C. The exploded views of the boxed regions are shown in (b) and (c). The dotted arrows indicate the path in which the electron probe microanalysis was done.

Fig. 3-17. The electron probe microanalysis (EPMA) scan results of the (a) overall specimen, (b) the anode and (c) the cathode, for specimen 1 which was put under $I=546$ mA for 160 minutes at 1300°C. The scan paths correspond to the dotted arrows in Fig. 3-16.

Fig. 3-18. X-ray diffraction patterns taken from (a) the anode vicinity and (b) the cathode vicinity of the electrotransported NiTiO_3 in Fig 3-16. Note that in

addition to the peaks for the mother matrix NiTiO_3 , only TiO_2 peaks are seen in the anode vicinity and only NiO peaks in the cathode vicinity.

Fig. 3-19. The EPMA profile for the whole specimen in specimen 2. Like Fig. 3-17 (a), kinetic unmixing is visible and the extent of unmixing is also similar.

Fig. 3-20. Backscattered images of the reaction couple (a) with Pt-markers (bright spots) embedded and (b) the other blank, simultaneously reacted in the identical surrounding for 120 hrs at 1300°C . Note that the reaction layer thicknesses are the same within experimental error. NiO is written in parentheses to note that it had been there but had spontaneously fallen off.

Fig. 3-21. (a) The overall reaction layer thickness and (b) the partial reaction layer thickness ratio vs. reaction duration time of the reaction couple $\text{NiO}|\text{TiO}_2$ at 1300°C in air. Dotted lines are the best fits to the theory which will be discussed in upcoming sections.

Fig. 4-1. Schematic configuration of the decomposition cell. According to quasi-binary approach, AO is in equilibrium with AB_2O_4 at interface ' and B_2O_3 in equilibrium with AB_2O_4 at interface ". ℓ is the thickness of the specimen.

Fig. 4-2. Schematic diagram of ABO_3 under electric field undergoing kinetic decomposition.

Fig. 4-3. The values of $f(\psi) = |(2 + 2\psi)/(1 - 2\psi)|$ as function of ψ . As ψ approaches $1/2$, one can see that the function explodes to infinity.

Fig. 4-4. Schematic diagram of AO-BO₂ diffusion couple employing inert markers. The positions are marked by ', " and "'. Figure not drawn to scale. The expected placement of inert markers (•) are shown for $D_A > D_B$ and $D_B > D_A$ in the bottom half.

Fig. 4-5. The comparison of experimentally obtained range of U_d and that expected from the theoretical treatment for NiTiO₃ at 1300°C in air. The x-axis is the full range of ψ obtained from inert marker experiment.

Fig. 4-6. Phase diagram of the system BaO-TiO₂. Unlike the phase diagram of the system NiO-TiO₂ (Fig. 3-4), various intermediate compounds exist around BaTiO₃. From Rase and Roy. [157]

Fig. 4-7. (a) The SIMS analysis result of LSGM from Schulz et al. La and Sr are A-site dopants while Mg is a B-site dopant. The SIMS analysis shows practically equal diffusion coefficients for both sites. (b) The proposed vacancy cluster mechanism. The clustered vacancies migrate through a sequence of vacancy jumps. After a sequence is completed, the whole vacancy cluster is migrated. From Schultz et al. [166]

Fig. 4-8. A schematic representation of (a) the curvature of ΔG^M , (b) the slope of composition of the intermediate compound would be $A_{0.5}B_{0.5}O_{1.5}$, so the formation ΔG^M and (c) ΔG^M itself. Illustrations not to scale. In (c), the strong and weak restoration for systems with large/small thermodynamic factor is shown when the composition of the system is moved from its equilibrium composition x_B^{eq} to x_B^{df} .

Fig. 4-9. The relationship between the integral mixing free energy and the

width of the stability limit.

Fig. 5-1. The elemental line scans across the reactions zone of CaO-Al₂O₃ diffusion couples, (a) (-)CaO-Al₂O₃(+), (b) (+)CaO-Al₂O₃(-) and (c) unelectrolyzed, reacted at 1250°C for 4 hours under electric field of 6.0×10^4 V/m. From Mackenzie et al. [169]

Fig. 5-2. Diffusion profiles of Mg in electrolyzed and unelectrolyzed MgO/Al₂O₃ couples at various temperatures, annealed for 48 hours with mean electric field strength of 4.93×10^4 V/m. -○-: unelectrolyzed, -x-: (-)MgO-Al₂O₃(+), -●-: (+)MgO-Al₂O₃(-). From Mackenzie et al. [171]

Fig. 5-3. The thickness of the spinel layer as a function of time. From Korte et al. [175]

Fig. 5-4. Schematic diagram of how the layer thickness will be affected by electric field, with A=Ni and B=Ti, drawn for $D_{Ni} > D_{Ti}$. The circles represent inert markers.

Fig. 5-5. The thickness of the formed NiTiO₃ layer according to the polarity as function of time. The "no current" case is equivalent to Fig. 3-21 (a). The dotted lines are best fit to eq. (5-9).

Fig. 5-6. Microstructure of the NiTiO₃ layer after formation under constant current of 0.4 A in the configuration (+)NiO-TiO₂(-) (a) for 24 hours and (b) for 12 hours at 1300°C. The NiO pellet fell off spontaneously and therefore is written in parentheses. One can see that the microstructure is very rough.

Fig. 5-7. The voltage-time plot under constant current of 0.4 A at 1300°C, for durations of 12, 36 and 60 hours in the configuration (+)NiO-TiO₂(-). All cases show an abrupt increase in the voltage lasting for about 20~30 ks.

Fig. 5-8. Microstructure of the NiTiO₃ layer after formation under constant current of 0.4 A in the configuration (-)NiO-TiO₂(+) for 48 hours, with (a) the enlarged view of the reaction zone and (b) the overall specimen. The NiO pellet was intact. The white particles in NiTiO₃ shown in (a) are platinum inert markers.

Fig. 5-9. (a) Enlarged view of the channels formed, (b) schematic illustration of the formation of vacancy channels or pinholes in NiTiO₃ and NiO for the configuration (-)NiO-TiO₂(+). The cation vacancies pile up at the NiTiO₃/TiO₂ boundary, then grow along the grain boundaries.

Fig. 5-10. The total layer thickness (top) and the placement of platinum inert markers (bottom) for NiO-TiO₂ diffusion couple at 1300°C for 72 hours.

List of Tables

Table 2-1. The migration energy of A-site La for the $\langle 100 \rangle$ path and B-site Mn for the $\langle 110 \rangle$ path and $\langle 100 \rangle$ curved path for each perovskite structure. One can see that for the B-site migration the migration energy is reduced greatly by the curved path. From De Souza et al. [34]

Table 3-1. Crystal structure of ABO_3 type compound according to Goldschmidt tolerance factor.

Table 3-2. Various inert marker elements and forms.

Table 3-3. Summary of the unmixing/decomposition experiments on $NiTiO_3$ at 1300°C . Specimens 1~5 exhibited both kinetic unmixing and decomposition while specimens 6 and 7 showed only kinetic unmixing.

Table 5-1. The fitted parameters according to eq. (5-9) for the data points shown in Fig. 5-6. It should be noted that the k_{elf} value for (+)NiO-TiO₂(-) may be overestimated.

List of Symbols

a_k	thermodynamic activity of component k
b_k	mechanical mobility of component k
c_k	concentration of component k
D_k	self diffusion coefficient of component k
$\overline{D_{Me}}$	average self diffusion coefficient of cations
D_k^*	tracer diffusion coefficient of component k
E	electromotive force of a galvanic cell
F	Faraday constant (=96485 C/mol)
ϕ	electrostatic potential
f_i	partial correlation factor
f_θ	thermodynamic factor of a system
g	geometrical factor
ΔG	Gibbs free energy change
$\Delta G_{f,k}^\circ$	Gibbs free energy of formation of component k
ΔG^M	Gibbs free energy of mixing
$\overline{\Delta G_k^M}$	relative partial molar Gibbs free energy of mixing of component k
i	current density
i_{appl}	externally applied current density
I	current
I_{appl}	externally applied current
j_k	matter flux of component k
j_{tot}	total flux
κ	unmixing ratio
k_B	Boltzmann constant (1.38×10^{-23} J/atom·K)
k_{elf}	fitting parameter reflecting the effect of electric field

k_p	Tamman constant
l	length of the specimen
L_{ij}	Onsager transport coefficient of components i and j
μ_k	chemical potential of component k
μ_k^0	standard chemical potential of component k
P_{O_2}	partial pressure of oxygen gas
R	gas constant (8.3145 J/mol·K)
r_k	ionic radius of component k
s	atomic jump distance
σ_k	partial electrical conductivity of component k
σ_{tot}	total electrical conductivity
t	time
T	absolute temperature in K
t_k	transference number of component k
U	voltage
U_d	decomposition voltage
v_k	velocity of component k
V_m	molar volume
v_{st}	steady state velocity
ω_k	atomic jump rate
ξ	position
x_k	molar fraction of component k
Δx_k	thickness of layer formed by component k
Δx_k^{max}	maximum range of molar fraction of component k
ψ	cation mobility (or diffusion coefficient) ratio
z_k	formal charge of component k
\bar{z}_k	effective charge of component k

1. Introduction

Ever since our primal ancestors started to use the most basic tools, beginning with the Stone Age, humans had the innate desire to better the tools they used. This resulted in the emergence of the Bronze Age, followed by the Iron Age that we live in today. With revolution from one age to another, our needs grew bigger and consequently the tools we used became more complex, and with the findings of more complex materials novel fields of application emerged, depending on what kind of driving forces we use to facilitate the devices incorporating these materials.

Such novel fields nowadays include solid oxide fuel cells, which is regarded as one of the prominent candidates to solve the human dependence on fossil fuels and the environmental crisis that could be looming just around the wall. Also, ever since transistors were used in the first computers, the capacity of computers has grown exponentially, thanks to better-performing dielectrics (multilayered ceramic capacitors) that are much smaller in size. Others may include thermoelectric devices, piezoelectric devices, et cetera.

When we look into these devices and fields more closely, we can immediately see how complex the materials we use today are. In solid oxide fuel cells, the following oxide compounds are used for respective components - yttria-stabilized zirconia (i.e. $Zr_{0.84}Y_{0.16}O_{1.92-\delta}$, YSZ)[1] or gadolinia-doped ceria (i.e. $Ce_{0.9}Gd_{0.1}O_{1.95-\delta}$, GDC)[2] as electrolytes; doped lanthanum chromium oxide ($LaCrO_3$)[3] as interconnects; lanthanum cobalt oxide doped with strontium and iron (i.e. $La_{0.6}Sr_{0.4}Co_{0.2}Fe_{0.8}O_{3-\delta}$, LSCF)[4], lanthanum manganese oxide doped with strontium (i.e. $La_{0.8}Sr_{0.2}MnO_{3-\delta}$, LSM)[5-7] or lanthanum nickel oxide (La_2NiO_4)[8] as cathode materials. Basically, all the components are made of complex oxides, with the exception of anodes which are mainly made of porous Ni-YSZ cermets. Solid oxide fuel cells are prime examples of complex device working under PO_2 gradient (or in more general terms, chemical potential gradient of a component

species).

With electric field as driving force, the following applications can be used as examples. Multilayered ceramic capacitors (MLCCs) are essential in our everyday devices - computers, smart phones and every device that calls itself electronic. The most famous compound is barium titanate (BaTiO_3) and it has been studied extensively[9-11]. Oxygen permeation membranes, which basically function in the reverse direction of solid oxide fuel cells, employ the following materials: barium cobalt oxide doped with strontium and iron (i.e. $\text{Ba}_{0.5}\text{Sr}_{0.5}\text{Co}_{0.8}\text{Fe}_{0.2}\text{O}_{3-\delta}$, BSCF)[12] or barium cobalt oxide doped with iron and niobium (i.e. $\text{Ba}_{0.7}\text{Co}_{0.3}\text{Fe}_{0.22}\text{Nb}_{0.08}\text{O}_{3-\delta}$, BCFN)[13]. Phase change random access memories also employ chalcogenides consisting of germanium, antimony and tellurium, such as GeSeTe_2 [14].

Thermoelectric devices or thermoelectrics basically convert the applied thermal gradient into electric work. Thermoelectrics also are consisted mainly of complex ionic compounds, although relatively simple chalcogenides also exist. For example, bismuth tellurides (Bi_2Te_3) and antimony tellurides (Sb_2Te_3) are the most prominent with high figure of merits[15]. Oxides with perovskite structures are also used, such as strontium titanates (SrTiO_3)[16,17], strontium ruthenates (SrRuO_3)[18] and calcium manganates (CaMnO_3)[19], along with sodium conductors such as Na_xCoO_2 [20] and other cobalt-based materials such as NaCo_2O_4 [21] and $\text{Ca}_3\text{Co}_4\text{O}_9$ [22]. Piezoelectric devices which convert the applied stress into electric work employ lithium niobate (LiNbO_3)[23], barium titanate[24] or lead zirconate titanate ($\text{PbZr}_x\text{Ti}_{1-x}\text{O}_3$, PZT)[25] as their prime materials.

There are more fields than the ones mentioned, but the point is made. Complex compounds (especially oxides) are essential in our current technology. These compounds are made up of ions that are arrayed in an ordered way according to their charges. When external driving force is applied to these compounds, because the ions all have different characteristics their response to the driving force is

different. Here an external driving force may refer to the following: (i) thermodynamic activity gradient (or conversely, chemical potential gradient) of any component consisting the material, (ii) electric potential gradient or electric field, (iii) thermal gradient or temperature gradient and (iv) nonhydrostatic stress, as shown previously.

Let us for now limit our discussion to complex oxides, such as AB_2O_4 (spinel) or ABO_3 (perovskites or ilmenites). As our atmosphere is filled with oxygen the oxides constantly strive to achieve equilibrium with their surrounding atmosphere according to thermodynamic principles. Oxygen is incorporated into the material in the form of oxygen anion by surface reaction. In a complex oxide ABO_3 , there basically are four charge carriers, namely A^{z_A+} , B^{z_B+} , O^{2-} and e^- (or, if electron holes are dominant, h^+), with z_A and z_B representing the formal charge of cations A and B. A crystal shift occurs only when cationic flow occurs. Oxygen incorporation and transport itself does not affect the overall lattice of the material, as oxygen can be supplied from or exhausted to the surrounding atmosphere, provided that the surface reaction proceeds fast enough. However, if the cations become more mobile, i.e. at high temperatures, the cations also begin to migrate, meaning that the overall lattice may shift. The cations will migrate in the same direction as they have the same type of polarity. If the cations constituting the material migrate in the same velocity with one another, then only the shift of crystal lattice occurs. No relative concentration gradient of cations would occur. This however is generally not the case. Because of their individual properties such ionic radii and valence, cations move at different velocities, in other words they have different mobility. As one cation moves faster in one direction and the other moves slower in the same direction when the driving force is applied, the originally homogeneous material becomes inhomogeneous, i.e. concentration gradient of cations build up inside the material in opposite directions.

Since electrochemical properties of a material are sensitive to their local

composition it can be easily estimated that with the build-up of concentration gradients the material may not function in the way it was intended to function. This becomes more obvious when the concentration gradient reaches a level wherein the material is no more thermodynamically stable. It then decomposes into constituent oxides, i.e. $ABO_3=AO+BO_2$ (with $z_A=2$ and $z_B=4$). This is a very simple example. The decomposition reaction may occur differently, resulting in other intermediate compounds in the system AO-BO₂). These degradative phenomena are termed kinetic unmixing and kinetic decomposition, respectively. They are known to occur in ternary or more complex oxides under various types of driving forces at high enough temperatures wherein the cations are sufficiently mobile, regardless of them being semiconductors or ionic conductors (electrolytes). A concise literature survey on kinetic unmixing and decomposition will be given in Chapter 2.

These degradative phenomena are generally considered as long-term issues, as cations generally migrate very slowly compared to other charge carriers (this however would depend on the type of crystal structure of the material). As the devices nowadays are applied to long-term operation (i.e. solid oxide fuel cells) under higher driving forces (i.e. multilayered ceramic capacitors, as they become thinner) these issues concerning kinetic unmixing and decomposition cannot be neglected and should be thoroughly researched. For example the electrolyte and electrodes in solid oxide fuel cells are exposed to high temperature (generally above 800°C) and Po₂ gradient while the interconnect is exposed to electric field. Long-term operation under these conditions will result in kinetic unmixing and even decomposition, and empirical results have been reported, as will be mentioned in Chapter 2.

As will be shown in Chapter 2, numerous literature report kinetic unmixing under both Po₂ gradient and electric field. However, it is obvious that kinetic decomposition affects the device property in a more serious way than kinetic unmixing, as the decomposed products generally have completely different

material properties compared to the original material. In case of kinetic decomposition, only few reports had been published with P_{O_2} gradient as driving force. However, no such phenomenon had been reported under electric field. In the work by Yoo et al. on $BaTiO_3$ [26], neither kinetic unmixing nor decomposition was observed even under large electric field. Since the phenomenon of decomposition under electric field had not yet been reported, no theoretical basis has yet been given either. In other words no research had been done on the critical magnitude of electric field that one must apply to the system for kinetic decomposition to occur, perhaps with the exception of the classic Gibbs theorem ($\Delta G = -nFE$), which links the Gibbs free energy of a reaction with the electric work done by the system. It will be shown in Chapters 2 and 4 that this equation, however, does not explain the phenomena.

Therefore, in this thesis kinetic unmixing and decomposition phenomena, with slightly more emphasis on decomposition, under electric field are reported for a model ternary oxide system. Since the reason for kinetic unmixing and decomposition is the difference in mobilities of the constituent cations as previously mentioned, one must obtain this mobility ratio for the system. The methods and literature on how to obtain the cation mobility ratios are introduced in Chapter 3.

Chapter 3 also reports the experimental results on kinetic unmixing and decomposition in a model ternary oxide $NiTiO_3$, followed by the results on the cation mobility ratio of the system $NiO-TiO_2$. In Chapter 4 a novel equation for obtaining the critical voltage required for decomposition (denoted U_d) is derived from steady state condition and closed circuit condition, and is compared with the experimental results obtained in Chapter 3. The issues concerning $BaTiO_3$, a ternary perovskite system where neither unmixing nor decomposition occurred under electric field, are taken into account and proposals on the thermodynamic reason for its behavior are suggested.

There is no question that electric field is the most abundant driving force available nowadays. As will be shown, electric field can affect solid state reactions - not just kinetic unmixing and decomposition, which are discussed thoroughly in Chapters 2 to 4, but also formation reaction, which is the reverse reaction of decomposition, because electric field can work as a secondary driving force in interdiffusion. Electric field can, in effect, affect the formation kinetics to change the thickness ratio and even microstructure of the formed product. This effect is shown, albeit qualitatively, in Chapter 5 with experimental results for the system NiO-TiO₂, along with literature.

2. Literature survey

(1) The definition of kinetic unmixing and decomposition

As mentioned in the introduction, when thermodynamic driving forces are applied to an ionic compound, the constituting ions migrate according to their respective valence charges. One should note that the term "ionic compound" here does not refer to compounds in which ionic partial conductivities are dominant, such as YSZ where oxygen ion partial conductivity is dominant[1], or silver iodide (AgI)[27] which is a silver ion conductor, i.e. an electrolyte. The term rather refers to compounds formed predominantly by ionic bonding, in contrast to metallic or covalent bonding. Therefore these "ionic compounds" may either be ionic conductors or semiconductors, or mixed ionic electronic conductors (MIECs).

Let us again focus on ternary oxides, consisted of two cation species and oxygen. The oxide may be a complete solution of two end members - the two oxides that make up the ternary oxide - i.e. AO and BO, so that it has the chemical formula (A,B)O, such as (Co,Ni)O or (Co,Mg)O, or it may be an intermediate compound ABO_3 , such as $BaTiO_3$ ($AO+BO_2$), or AB_2O_4 , such as $MgAl_2O_4$ ($AO+B_2O_3$). As one can see, complete solutions are usually made when the two end members have homovalent cations. This is because when the two end members mix, their miscibility is enhanced when the end members have identical crystal structure, as additional energy required for the distortion of one end member to be incorporated into the other end member is reduced by the identical crystal structure. For example, a rock salt structured material will mix better with another rock salt structured material. Here, rock salt structure which is a close-packed structure is used as an example as ionic compounds tend to form themselves into close-packed structures (face-centered cubic or hexagonal close-packing). Therefore, oxides with homovalent cations, i.e. CoO, MgO, CaO and NiO (which all form rock salt structure), mix well and produce complete solid solutions, as shown in Fig. 2-1.

On the other hand, it generally becomes difficult for end members with heterovalent cations, i.e. CoO-TiO₂ or MgO-Al₂O₃, to form such complete solution. As a result, these oxides create various intermediate compounds in which the end members combine in specific stoichiometric ratios. A good example is CoO-TiO₂ system, with intermediate compounds of CoTi₂O₅, CoTiO₃ and Co₂TiO₄[28]. These compounds are nearly stoichiometric and have very narrow stability regime, and are usually represented as a single line in many thermodynamic phase diagrams, as shown in Fig. 2-2 (a). Of course, there are some exceptions, such as in the system BeO-Y₂O₃[29] (Fig. 2-2 (b)), but the general trend is as given in Fig. 2-2 (a).

When an external thermodynamic driving force is applied, the cations migrate in one direction and the anion (oxygen ion) migrates in the opposite direction. When the cations migrate, the two cations generally do not migrate at the same rate because they have different mobility or diffusion coefficient. This is because either their atomic jump frequencies or their migration paths are different. The jump frequencies are related to the self diffusion coefficients. The difference of migration path can be visualized by the following example.

For example, in perovskites represented by the formula ABO₃, the A cation migrates through A-site migration path and B cation through B-site migration path, provided that the sites are well-ordered and not mixed. These migration paths have very different migration activation energies. Assuming vacancy mechanism for cation migration (because perovskites are of close-packed nature, vacancy mechanism is preferred to interstitial mechanism) and pseudocubic lattice (as perovskites can be cubic, orthorhombic or rhombohedral), the A-site cations migrate by vacancy migration between neighboring sites, in the <100> direction. B-site cations are expected to travel diagonally in <110> direction to reach the nearest B-site, or they may move also in <100> direction, but around the oxygen anion, as shown in Fig. 2-3. Since the B-site cations must travel longer distance and through narrower space, more energy is required for their migration. This has

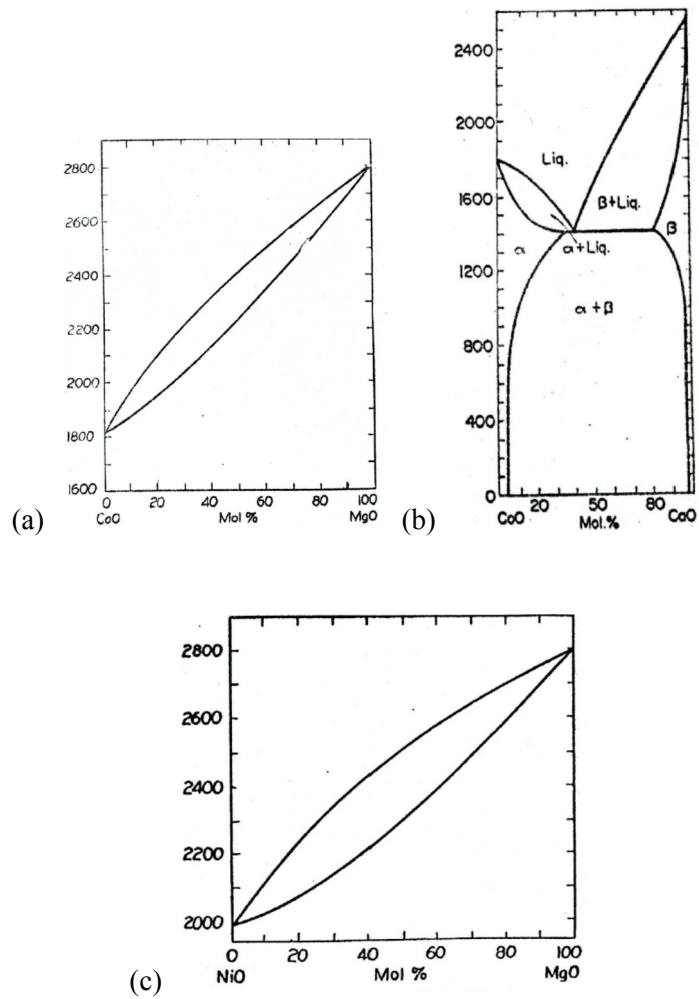
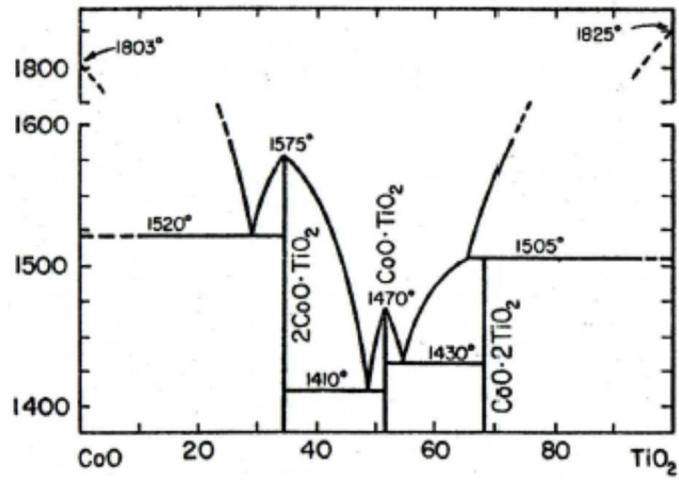
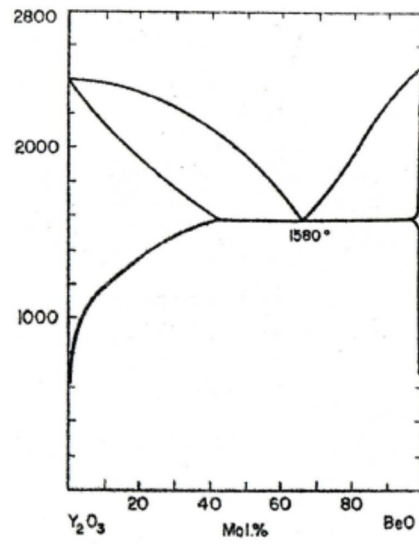


Fig. 2-1. Thermodynamic phase diagrams of (a) CoO-MgO[30], (b) CoO-CaO[31] and (c) MgO-NiO[32], all showing complete miscibility of the end members AO-BO.



(a)



(b)

Fig. 2-2. Thermodynamic phase diagrams of (a) CoO-TiO_2 [28] and (b) $\text{Y}_2\text{O}_3\text{-BeO}$ [29] systems. (a) is the general behavior for heterovalent systems.

been shown by computer modeling techniques. De Souza and Maier[33] showed for LaGaO₃-type perovskite that the B-site migration energy is about two to three times larger than the A-site migration energy, depending on the path and element. Similar results have been reported by De Souza et al.[34] and Islam[35] in LaMnO₃ perovskite and are shown in Table 2-1.

Due to the different mobility, the cations migrate at a different rate. Therefore, one side of the material becomes enriched with one species while the opposite side is enriched with the other species. In other words, the originally homogeneous material now becomes inhomogeneous and cation concentration gradients are formed within the material in the opposite directions. This is termed *unmixing*. As the unmixing continues, provided that the driving force is large enough, the gradients become larger and at some point will become too large for the material to be stable in the current thermodynamic phase. In this case the material begins to decompose into its end members and this consequently is termed *decomposition*. These phenomena are schematically shown in Fig. 2-4.

For complete solid solution, only kinetic unmixing occurs as there is no solubility limit (although one can state that, if the unmixing occurs to the extent that the compositions of end members are reached, it can be called decomposition). If the material is an ideal intermediate compound so that it exists only at an exact stoichiometric ratio (i.e. AO:BO≡1:1), then upon the application of thermodynamic driving force it will immediately undergo kinetic decomposition. However, intermediate compounds always exist in a range of composition, however narrow it may be, so they would first be kinetically unmixed, then as the concentration gradient exceeds the stability limit they will undergo kinetic decomposition.

When dealing with chemical reactions, one must take into account two fields of studies, namely thermodynamics, which tells us whether the reaction would occur

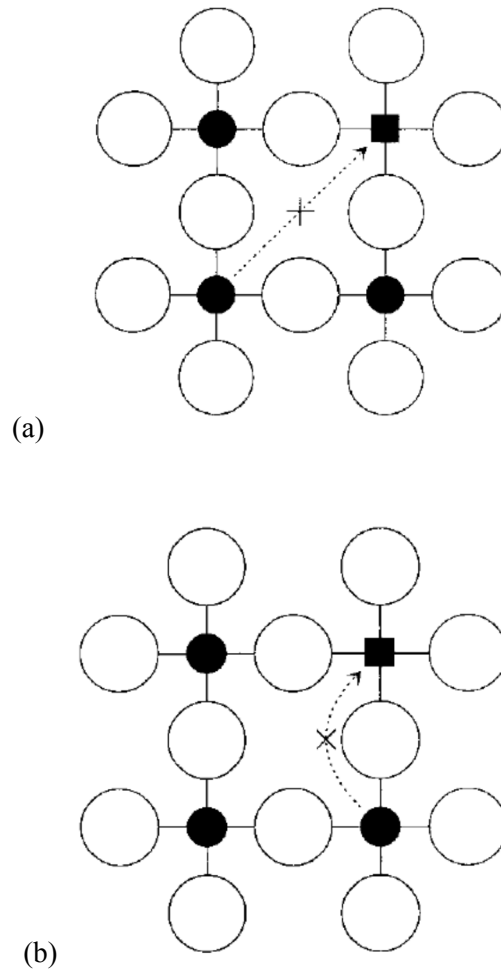


Fig. 2-3. Schematic diagram of (a) the $\langle 110 \rangle$ path for migration of B-site Mn and (b) the curved, lower energy path for migration in the direction $\langle 100 \rangle$, shown on the $\{100\}$ plane. From De Souza et al.[34]

Crystal system	E_m^{La} / eV	E_m^{Mn} / eV	
		$\langle 110 \rangle_{cubic}$	$\langle 100 \rangle_{cubic}$
Cubic	3.93	14.71	7.73
Rhombohedral	4.14	14.00, 15.73	8.82
Orthorhombic	4.22, 4.26, 4.32	14.11, 14.73	9.94, 10.64

Table 2-1. The migration energy of A-site La for the $\langle 100 \rangle$ path and B-site Mn for the $\langle 110 \rangle$ path and $\langle 100 \rangle$ curved path for each perovskite structure. One can see that for the B-site migration the migration energy is reduced greatly by the curved path. From De Souza et al. [34]

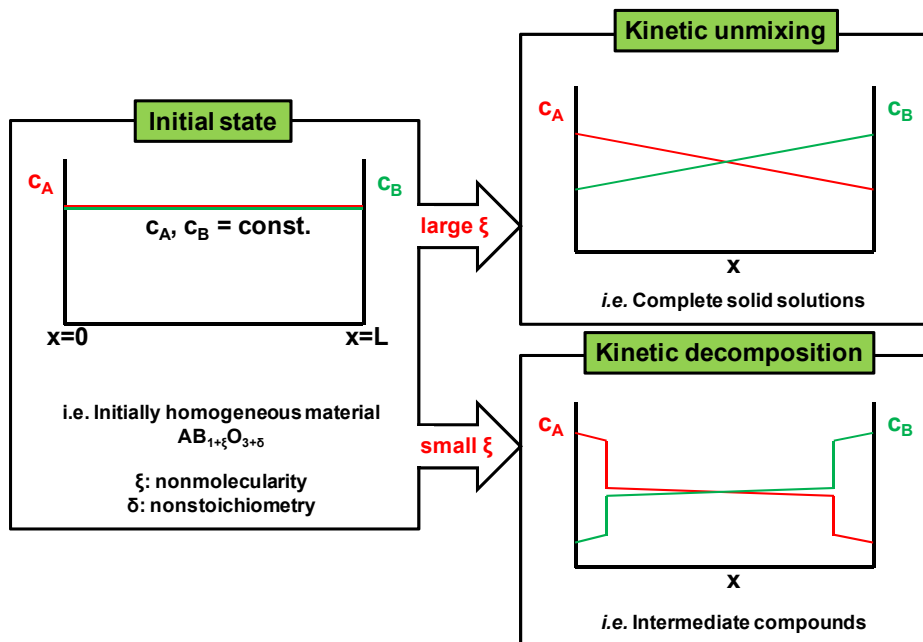


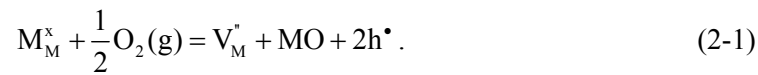
Fig. 2-4. Schematic diagram of the progress of kinetic unmixing and decomposition. Large ξ corresponds to complete miscibility of the end members while small ξ corresponds to narrow stability regime of the compound.

or not based on the gain or loss of energy, and kinetics, which describes how fast the given reaction would occur. A useful analogy would be that thermodynamics decide the initial and final states while kinetics decide the path. The term *kinetic* signifies that these phenomena occur by kinetic reasons. The origin of these phenomena is purely the difference in the cation mobilities. No thermodynamic factors affect these phenomena; only the cation mobilities, or their reactivity to thermodynamic driving forces, govern these phenomena. Due to this origin, even when the material is thermodynamically stable under the given thermodynamic conditions (which is decided by, for example, temperature and P_{O_2}), it may still undergo kinetic unmixing or decomposition (again, the reason these phenomena are termed *kinetic*). This will again be discussed later with experimental results in literature.

Kinetic decomposition is different from thermodynamic decomposition in that its products always appear at opposite surfaces - they can never appear at the same surface. In case of thermodynamic decomposition, the products generally appear in a mixed matrix or they coexist on the same surface[36], while for kinetic decomposition the products can only appear on the opposite surfaces, where the driving force is applied (i.e. AO at the high P_{O_2} surface and BO_2 at the low P_{O_2} surface).

Now let us look at these phenomena from a more microscopic sense. Let us assume that the system in consideration is a semiconducting $(A,B)_{1-\delta}O$, a complete solution where the cations migrate by vacancy mechanism and are compensated by electron holes (therefore the majority defects are $V_A^{z_A/}$, $V_B^{z_B/}$ and h^\bullet . The rules for notation are given below). Also, let us assume that oxygen ions are practically immobile compared to the cations. This lets us set the laboratory reference frame as the oxygen sublattice. Two kinds of driving force are taken into account - P_{O_2} gradient and electric field, which are the most common.

When we apply P_{O_2} gradient to this specimen, shaped as a flat plate for simplicity (therefore we consider diffusion in one direction only), that is at equilibrium under given thermodynamic conditions, the following occurs. At the higher P_{O_2} side, oxygen from the gas atmosphere arrives at the surface and combines with metal A or B to create new lattice molecule MO at the surface, while generating metal vacancy and electron holes. To write this reaction concerning point defects, Kröger-Vink notation[37] is utilized. A structure element, regular or irregular, is denoted as S_p^C , where S is the structure element type, written in either elemental symbol or V for vacancy; P the position or site wherein the structure element is situated, written in either elemental symbol or i for interstitial sites; C the effective charge, given as (absolute charge of the structure element) - (absolute charge of the site) and denoted by \bullet for positive, $'$ for negative and \times for neutral charge. For example, a vacancy on cation site is denoted as $V_M^{z_M'}$ (with $M=A$ or B). Using this notation system, the oxygen incorporation reaction can be written as



At the lower P_{O_2} side, the opposite reaction occurs. The metal vacancies and electron holes combine with MO at the surface and oxygen is released to the low P_{O_2} atmosphere. Consequently, metal vacancies migrate from the high P_{O_2} side to the low P_{O_2} side, resulting in metal cation flux in the opposite direction. Therefore lattice is annihilated at the lower P_{O_2} side and is created at the higher P_{O_2} side, and the whole material moves in the direction of higher P_{O_2} side.

When the cations migrate, as mentioned before, they migrate by different path and therefore generally have different mobility. Assuming cation A to be faster than B, as time passes A will slowly be more accumulated at the higher P_{O_2} side while B will be stagnated at the lower P_{O_2} side, resulting in kinetic unmixing. Further unmixing will result in decomposition as the composition exceeds thermodynamic

phase boundaries, as shown in Fig. 2-5. One can also think of it as two cation sublattices moving at different velocities until they reach steady state. At steady state the two sublattices migrate at the same velocity.

Let us now replace the P_{O_2} gradient with electric field, another representative thermodynamic driving force. This case would be easier to understand, as the polarities are more clearly visible. When electric field is applied to (or electric current is flown through) the specimen, cation vacancies which have relatively negative charge will migrate from (-) to (+) electrode and cations will migrate conversely from (+) to (-) electrode. The electrode reactions will be the same as those for P_{O_2} gradient, i.e. eq. (2-1) for the (-) electrode and so on. The main difference between P_{O_2} gradient and electric field is that electrodes are physically required for the electric field case.

The externally applied driving forces create uphill migration of ions, i.e. they pump the ions toward the highly-concentrated side. When this concentration gradient is formed, a diffusion flux arises to negate this concentration gradient, according to downhill diffusion as described by Fick's law. When one applies a constant external driving force, there is a limit to the concentration gradient formed by uphill migration. With time, the downhill diffusion flux becomes large enough to compensate the externally applied driving force. When at one point the diffusion flux balances the flux from external driving force, no further unmixing occurs as both cations move at the same velocity in the same direction. This state is termed "steady state," as macroscopically no change in concentration occurs except that the whole specimen migrates toward the high P_{O_2} side or the (-) electrode. The velocity of each species is defined as the flux per concentration or $v_k = j_k / c_k$, with j_k the matter flux and c_k the concentration of species k. Upon steady state both cations and therefore the crystal lattice move at the steady velocity v_{st} ,

$$v_{st} = \frac{j_A}{c_A} = \frac{j_B}{c_B} . \quad (2-2)$$

As will be shown later, all the theoretical considerations begin with eq. (2-2).

The migration of oxygen ions are neglected, as we have assumed that the majority defects are cation vacancies and electron holes and that oxygen ions are virtually immobile. This would not be the case if the material is oxygen conductor so that the majority defects are, for example oxygen interstitials and electron holes (for example La_2NiO_4 [38]; the opposite case, of oxygen vacancies and electrons as majority defects, generally occur in low P_{O_2} atmospheres, as for doped ceria[39]). The overall phenomena occurring in the material are the same, regardless of where the majority defects lie. However, in this case the cation transference number (defined as the ratio of the species flux to the total flux, $t_{k=j} = j_k/j_{\text{tot}}$) generally becomes so small that the detection of cation migration is almost impossible as tremendous amount of time is required.

The kinetic unmixing and decomposition phenomena in ternary oxides were first introduced and experimentally shown by Schmalzried et al.[40] and has been researched for various systems, although the literature so far is still quite limited in number. Of the aforementioned thermodynamic driving forces, the most abundantly researched are oxygen partial pressure gradient and electric field, probably because they are the most used in the industry and are the most easily applicable ones. In the next section the literature since Schmalzried et al. on these phenomena are introduced.

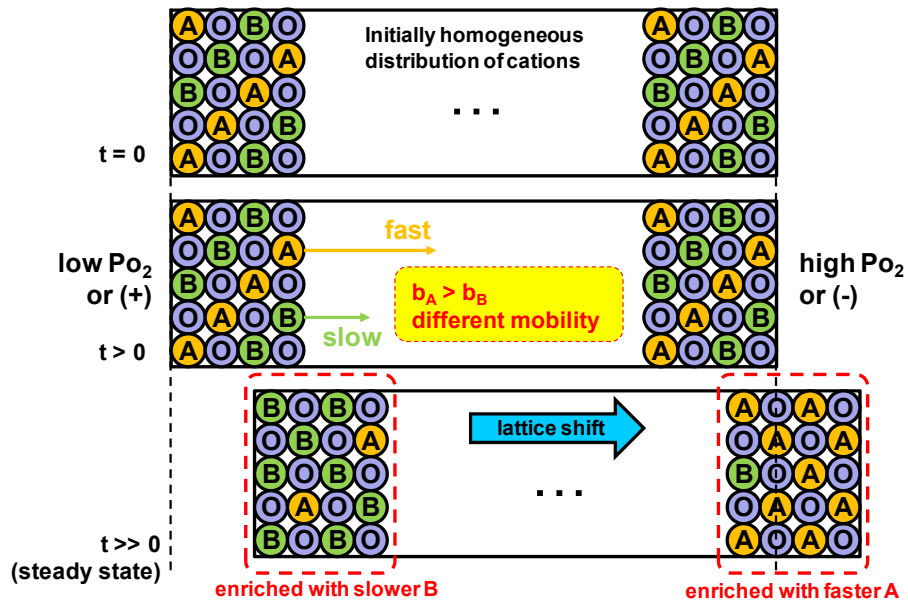


Fig. 2-5. Schematic diagram of the ionic movements when kinetic unmixing and/or decomposition occurs, for the case of $b_A > b_B$. (b_k : mechanical mobility of species k) With cation flow, lattice shift or crystal shift occurs along with kinetic unmixing and/or decomposition.

(2) The history of kinetic unmixing and decomposition

Here, a concise version of the literature on kinetic unmixing and decomposition is given in as chronological order as possible, categorized by driving forces. Kinetic unmixing and decomposition has been studied most extensively under P_{O_2} gradient, followed by electric field. The work on stress gradient and thermal gradient is quite limited in number and as they are not within the scope of this thesis, will only be discussed very briefly.

(a) Chemical potential gradient (P_{O_2} gradient)

(i) The basics

In principle, the chemical potential gradient $\nabla\mu_k$ of any component of the complex oxide (A,B)O can be applied to the oxide to induce kinetic unmixing and/or decomposition, i.e. $\nabla\mu_A$, $\nabla\mu_B$ or $\nabla\mu_O$ (can be replaced by $\nabla\mu_{O_2}$). However, since it is generally easier to measure the chemical potential of gaseous oxygen than it is to measure that of the cation components, $\nabla\mu_{O_2}$ is always applied as the driving force. Practically no literature with $\nabla\mu_A$ or $\nabla\mu_B$ as applied driving force was found, and therefore the driving force termed "chemical potential gradient" here is synonymous to $\nabla\mu_{O_2}$ (of course, the applied $\nabla\mu_{O_2}$ will cause $\nabla\mu_A$ and $\nabla\mu_B$ in the material. However, that would be an indirect effect. When discussing driving force, only the *directly applied* driving force is taken into account). $\nabla\mu_{O_2}$ is applied by exposing the opposite surfaces of the oxide to different P_{O_2} 's, since $\mu_{O_2} = \mu_{O_2}^0 + RT \ln P_{O_2}$ (assuming ideal gas behavior) and $\nabla\mu_{O_2} = RT \nabla \ln P_{O_2}$.

The first work on kinetic unmixing had been done by Schmalzried et al.[40] for the system (Co,Mg)O, shown in Fig. 2-6. The oxygen sublattice is virtually immobile in this case because the oxygen ions are close-packed into rock salt structure and the majority defects are cation vacancies and electron holes. Yurek and

Schmalzried[41] first showed for a CoO single crystal under P_{O_2} gradient that a cation vacancy concentration gradient occurs, resulting in cation vacancy flux from the high P_{O_2} side to the low P_{O_2} side and consequent cation flux in the opposite direction along with macroscopic crystal shift (the result of which is eq. (2-1) shown earlier). From this Schmalzried et al. speculated that unmixing would occur in the same manner, by cation vacancy migration.

$Co_{1-\delta}O$ and $Mg_{1-\delta}O$ both have rock salt structure and since they are homovalent they mix well and form complete solid solution (Fig. 2-1)[30]. Therefore under P_{O_2} gradient $(Co,Mg)O$ will only undergo kinetic unmixing (unless, as mentioned before, the compositions reach those of the end members, which can be deemed as decomposition). As this work sets the cornerstone for kinetic unmixing, let us go through it more specifically.

Let us assume that the molar volume of homovalent mixed oxide $(A,B)O$ remains constant and that the oxide solution is semiconducting, specifically a p-type semiconductor. Local thermodynamic equilibrium is assumed to prevail and the cross terms in Onsager's reciprocal theorem are neglected, i.e. only direct transport is taken into account (the cross terms will later be taken into account) and one-dimension transport (in ξ -direction. ξ is used instead of x to prevent confusion from molar fraction x_k) is taken for simplicity. Also, the solution $(A,B)O$ is assumed to be an ideal solution with respect to its components AO and BO . For a component its matter flux is defined by the gradient of its electrochemical potential gradient, i.e.

$$j_A = -\frac{D_A c_A}{RT} \frac{\partial \eta_{A^{2+}}}{\partial \xi} \quad (2-3)$$

where R is the gas constant, T the absolute temperature, D_k the self diffusion

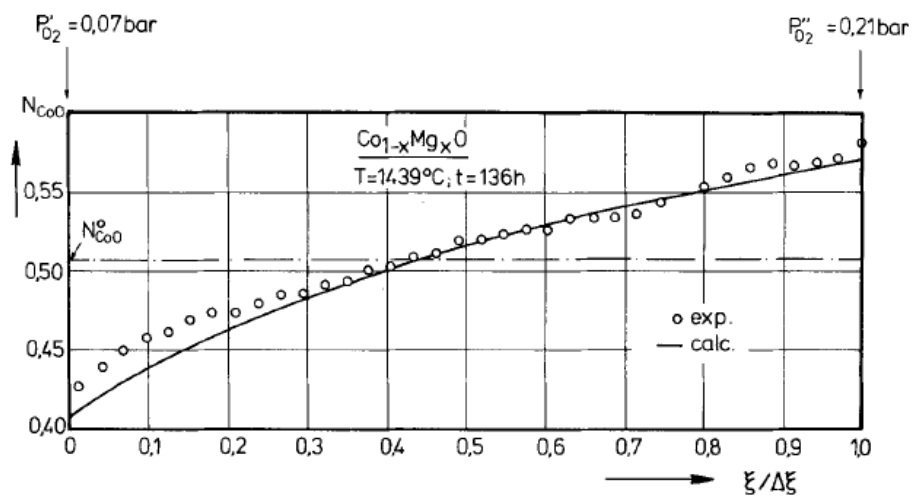


Fig. 2-6. The unmixing result of Schmalzried et al. for the system (Co,Mg)O. From Schmalzried et al. [40]

coefficient, c_k the concentration and η_k the electrochemical potential gradient (defined as $\eta_k = \mu_k + z_k F \phi$, with F the Faraday constant, μ_k the chemical potential, z_k the formal charge and ϕ the electrical potential) of species k . Because the specimen is a semiconductor ($\nabla \eta_{e^-} \approx 0$), the electrochemical potential gradient of cation can be replaced by its chemical potential gradient (by local equilibrium, $A^{2+} = A - 2e^-$ and $\nabla \eta_{A^{2+}} = \nabla \mu_A - 2\nabla \eta_{e^-} \approx \nabla \mu_A$), i.e.

$$j_A = -\frac{D_A c_A}{RT} \frac{\partial \mu_{A^{2+}}}{\partial \xi} \quad (2-4a)$$

and analogous equation can be set up for cation B as

$$j_B = -\frac{D_B c_B}{RT} \frac{\partial \mu_{B^{2+}}}{\partial \xi}. \quad (2-4b)$$

By local equilibrium, for the reactions $A+O=AO$ and $B+O=BO$ the following relations are valid:

$$\nabla \mu_A + \nabla \mu_O = \nabla \mu_{AO}, \quad (2-5a)$$

$$\nabla \mu_B + \nabla \mu_O = \nabla \mu_{BO}. \quad (2-5b)$$

Inserting eqs. (2-5a) and (2-5b) into eqs. (2-4a) and (2-4b) and using the ideal solution condition ($\mu_{AO} = \mu_{AO}^o + RT \ln x_A$, with μ_{AO}^o the chemical potential at standard state. Here, x_A is taken instead of x_{AO} meaning that all A ions exist as AO. If the solution is not ideal, the molar fraction x_A should be replaced by the activity $a_A = \gamma_A x_A$ with γ_A the activity coefficient) the following equations are obtained:

$$j_A = -\frac{D_A x_A}{V_m} \left[\frac{\partial \ln x_A}{\partial \xi} - \frac{\partial}{\partial \xi} \left(\frac{\mu_O}{RT} \right) \right], \quad (2-6a)$$

$$j_B = -\frac{D_B x_B}{V_m} \left[\frac{\partial \ln x_B}{\partial \xi} - \frac{\partial}{\partial \xi} \left(\frac{\mu_O}{RT} \right) \right] \quad (2-6b)$$

with V_m the constant molar volume of (A,B)O and $c_k = x_k/V_m$. At steady state, by inserting eqs. (2-6a) and (2-6b) into eq. (2-2) we arrive at

$$d \left(\frac{\mu_O}{RT} \right) = \frac{\gamma - x_A}{x_A (1 - x_A)} dx_A \quad (2-7)$$

with $\gamma = \frac{D_A}{D_A - D_B}$. According to Schwier et al.[42] the self diffusion coefficients

can be represented as

$$D_k = D_k^0 \times P_{O_2}^{1/n} \exp(bx_k) \quad (2-8)$$

where n and b are constants that are determined by tracer experiments. Since both A and B are migrating by the same cation vacancies (although atomistically their respective jump frequencies may be different), n and b are expected to be equal. Therefore γ becomes independent of the composition or P_{O_2} and is given as $\gamma = D_A^0 / (D_A^0 - D_B^0)$.

Eq. (2-7) can be integrated as

$$\frac{\mu_O(\xi') - \mu_O(\xi'')}{RT} = \gamma \ln \frac{x_A(\xi')}{x_A(\xi'')} - (1 - \gamma) \ln \frac{1 - x_A(\xi')}{1 - x_A(\xi'')} \quad (2-9)$$

where ξ' and ξ'' are the positions of the two opposite crystal surfaces where

$\nabla\mu_{\text{O}}$ is applied. This can be rearranged as

$$\frac{(x_A'')^\gamma}{(1-x_A'')^{\gamma-1}} = \exp\left(\frac{\mu_{\text{O}}'' - \mu_{\text{O}}'}{RT}\right) \frac{(x_A')^\gamma}{(1-x_A')^{\gamma-1}}. \quad (2-10)$$

Eq. (2-10) shows that when the applied Po_2 gradient (and therefore $\mu_{\text{O}}'' - \mu_{\text{O}}'$) and diffusion coefficient ratio γ are known, the molar fraction ratio at the interfaces x_A' and x_A'' can be calculated. However, there are two variables and only one equation, and another equation is required to solve for the two variables x_A' and x_A'' , the mass conservation equation, namely

$$x_A^{\text{O}} \Delta \xi = \int_0^{\Delta \xi} x_A d\xi = x_A'' \Delta \xi - \int_{x_A'}^{x_A''} \xi dx_A \quad (2-11)$$

where the right-hand side of eq. (2-11) is done by integration by parts. These equations cannot be solved analytically. The derivation from this point on will not be done here, as it is not the main objective of this thesis to numerically calculate the profiles. The important part is that two equations (eqs. (2-10) and (2-11)) which are derived from steady state condition and mass conservation are required to numerically calculate the concentration profiles.

The calculated concentration profile according to eqs. (2-10) and (2-11) was compared with the experimental results obtained in the (Co,Mg)O system. Steady state concentration profile was obtained for the system after exposure to Po_2 gradient and was well-fit with the calculated results, although at the anode the concentration profile deviated to some extent (Fig. 2-6). Schmalzried et al. explained this discrepancy by the unstable morphology of the anode side. The annihilation of lattice molecules does not proceed in a planar manner; rather, they proceed selectively from any disturbance on the surface, such as grain boundaries

(although in this experiment the sample was single crystal so this would be neglected) or mechanical indentations or surface pores. This indentation would grow toward the cathode and will be accelerated more as it is grown (termed the "self-acceleration process"). Due to this the mean oxygen potential gradient becomes smaller in the anode region as the low P_{O_2} boundary condition takes effect deeper in the lattice and therefore the extent of unmixing is smaller, thus the deviation toward smaller kinetic unmixing at the anode side. The influence of pore formation or indentation growth on the steady state experimental profiles would be the smallest at the early stages of steady state, as the "self-acceleration process" would become stronger with time. Schmalzried et al. also showed in the same work that this indeed is the case.

In their next work Schmalzried and Laqua[43] presented the unmixing behavior for (i) complete solid solution, (ii) solid solution with limited miscibility and (iii) ternary compound with very narrow range of homogeneity (in other words, near-stoichiometric compounds). The first case is a restatement of the previous work (Co,Mg)O so we will focus on the two latter cases. For the case of solid solution with limited miscibility, let us take an imaginary system with a miscibility gap and term the phases $(A,B)O^\alpha$ and $(A,B)O^\beta$. If the originally homogeneous oxide is in the α phase and very small P_{O_2} gradient is applied so that the compositions do not fall into the miscibility gap, then only unmixing within the α phase is observed. However, when the driving force is large enough so that the miscibility gap is reached, the α phase is split into α and β phase. The overall treatment is analogous to that of the complete solution case, but an additional equation is needed as new interface between the α and β phases is created. The continuity equation across the interface is formulated as

$$\left. \frac{j_A^\alpha}{c_A^\alpha} \right|_{\xi^{\alpha\beta}} = \left. \frac{j_A^\beta}{c_A^\beta} \right|_{\xi^{\alpha\beta}} \quad (2-12)$$

in which $\xi^{\alpha\beta}$ signifies the position or locus of the interface. Eqs. (2-10) to (2-12) can be combined to numerically solve for the concentration profiles, although more assumptions, such as the diffusion coefficient ratio of the α and β phases, are needed. The experimental results were given for the system (Ni,Ti)O. NiO has rock salt structure but titanium oxide generally exists as TiO₂, usually in the rutile form (and in brookite or anatase form depending on the thermodynamic conditions). In other words, the oxide (Ni,Ti)O is essentially NiO doped with Ti and can be written as (Ni_{1-x}Ti_{x/2})O. When it is put under Po₂ gradient, the high Po₂ side still exists as a rock salt solution but with higher Ni content while the low Po₂ side turned into ilmenite NiTiO₃. In the literature it was found that $D_{Ti} > D_{Ni}$ in this solution, so according to the theory up to now Ti should be enriched at the high Po₂ side, but it was instead enriched at the low Po₂ side ($c_{Ti}^o = 14$ w/o, $c_{Ti}^{NiTiO_3} = 39$ w/o). This was explained qualitatively by cross effect, which had so far been neglected. They explained that when Ti enters the NiO lattice it acts as $Ti_{Ni}^{\bullet\bullet}$ and strongly interacts with the cation vacancy $V_{Ni}^{//}$. With the flow of cation vacancies toward the high Po₂ side, $Ti_{Ni}^{\bullet\bullet}$ is transported with the vacancies, thus resulting in such experimental profile. However this theory was not pursued quantitatively. The results for (Ni_{1-x}Ti_{x/2})O are given in Fig. 2-7.

The same relations also apply for near-stoichiometric compounds. The difference is that there is a limit to Po₂ difference that the oxide can endure, which is related to the Gibbs energy of formation of the stoichiometric compound. As this is the main theme of this thesis, more specific explanation will be given later in section (iv) of this Chapter. Schmalzried and Laqua showed for a near-stoichiometric ilmenite NiTiO₃ that after exposure to Po₂ gradient the ilmenite kinetically decomposed into TiO₂ and NiO with NiO on the high Po₂ side, signifying that $D_{Ni} > D_{Ti}$ in the ilmenite phase assuming that cross effect is negligible. For the system Co₂TiO₄ they showed that it decomposed into a series of compounds, namely TiO₂-CoTi₂O₅-CoTiO₃-Co₂TiO₄-CoO (from low Po₂ to high Po₂ side), as shown in Fig. 2-8 (b).

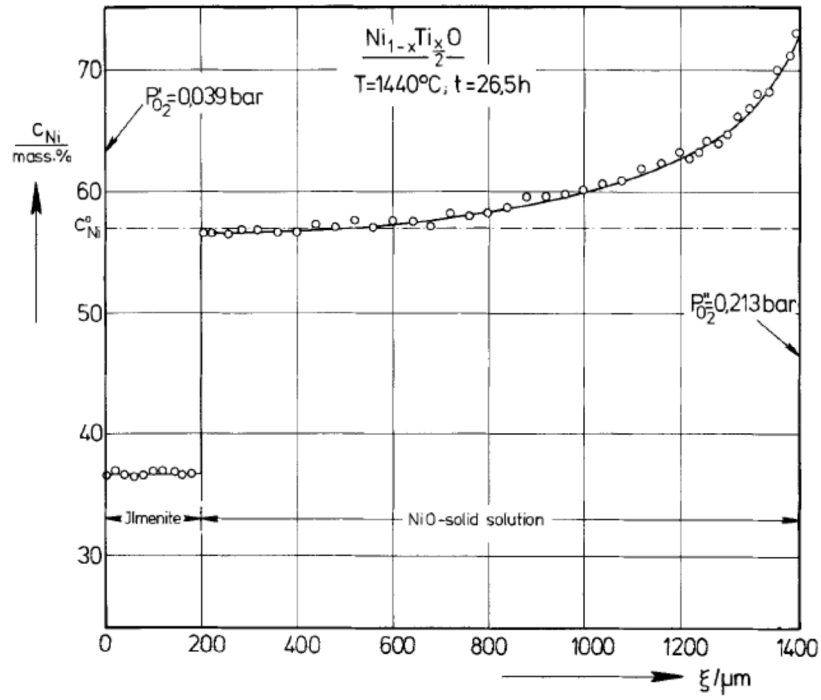
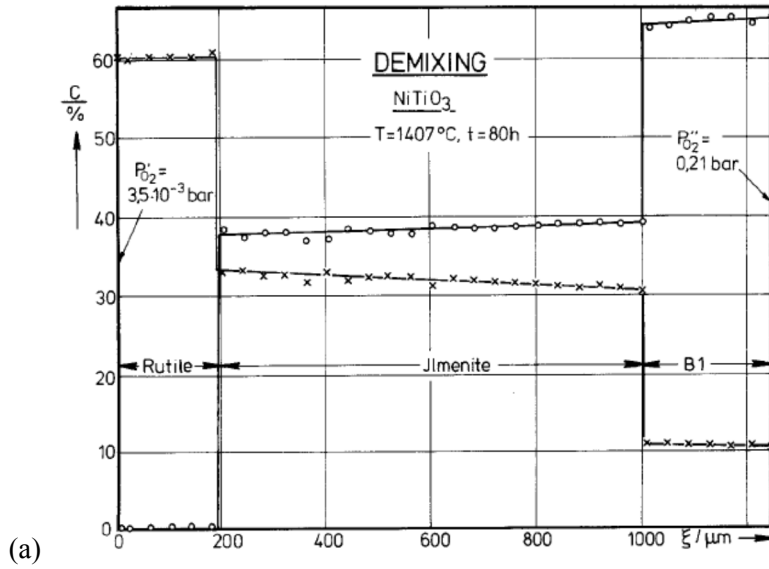
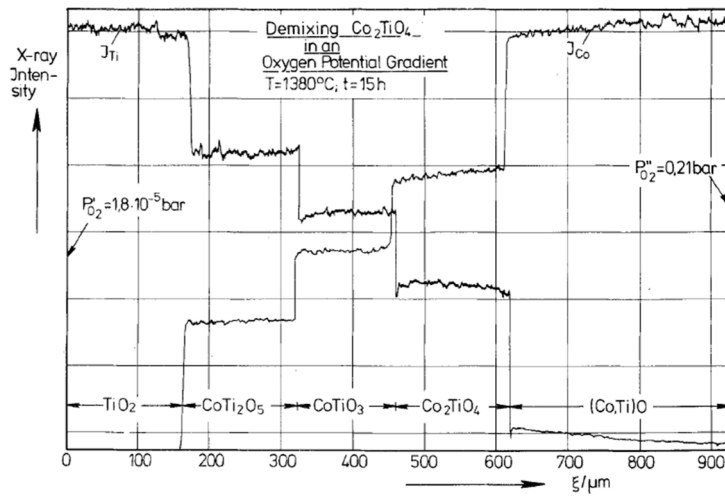


Fig. 2-7. The experimental unmixing profile for $(Ni_{1-x}Ti_x)_2O$ with initial concentration of Ti=14 w/o, from Schmalzried and Laqua [43].



(a)



(b)

Fig. 2-8. The decomposition profiles under P_{O_2} gradient for the systems (a) NiTiO_3 and (b) Co_2TiO_4 . From Schmalzried and Laqua [43].

This would mean that $D_{Co} > D_{Ti}$ in all ternary phases, although no further analysis was provided. The difference in behavior of $NiTiO_3$ and Co_2TiO_4 is due to the existence of other intermediate compounds in the quasibinary phase diagrams. $NiTiO_3$ is the sole intermediate compound in the $NiO-TiO_2$ system[44,45] while $CoO-TiO_2$ consists of various intermediate compounds (Fig. 2-2 (a))[28]. This work by Schmalzried and Laqua seems to be the first report on the kinetic decomposition of ternary compounds.

In 1989 Ueshima et al.[46] reported the unmixing of iron manganese oxide with initial composition of $(Mn_{0.6}Fe_{0.4})_{1-\delta}O$, again a p-type semiconductor with $D_{Mn}, D_{Fe} > D_O$. Using the phase diagram of second kind (this kind of phase diagram plots P_{O_2} vs. composition, compared to the first kind which shows temperature vs. composition) they analyzed the phase separation into wüstite and spinel phases and the internal unmixing of each phase. At the low P_{O_2} side wüstite was solely found, while at the high P_{O_2} side only spinel or a blend of spinel and wüstite was found (Fig. 2-9). An interesting result was that Mn was concentrated at the high P_{O_2} side in spinel while it was concentrated at the low P_{O_2} side in wüstite, signifying that the relative diffusion coefficients of Fe and Mn have opposite tendencies in the two phases. They also successfully explained the spinel-wüstite band structure and the reason for irregular shape.

Unmixing or decomposition in materials in which the majority defects lie rather on the oxygen sublattice is very difficult to observe. A simple calculation was done by Martin[47] for a model system of $(A_{1-x}B_x)O_{2-x/2}$, wherein A is a tetravalent cation and B a trivalent one, as in yttria-doped zirconia (YSZ). In the electrolytic regime the oxygen ion transference number is practically unity and under a given P_{O_2} gradient no oxygen flux can occur because in order for oxygen ion to flow a transfer of electronic species must occur at the same time. Therefore an external circuit connecting both sides of the surface is required for electronic transport (this

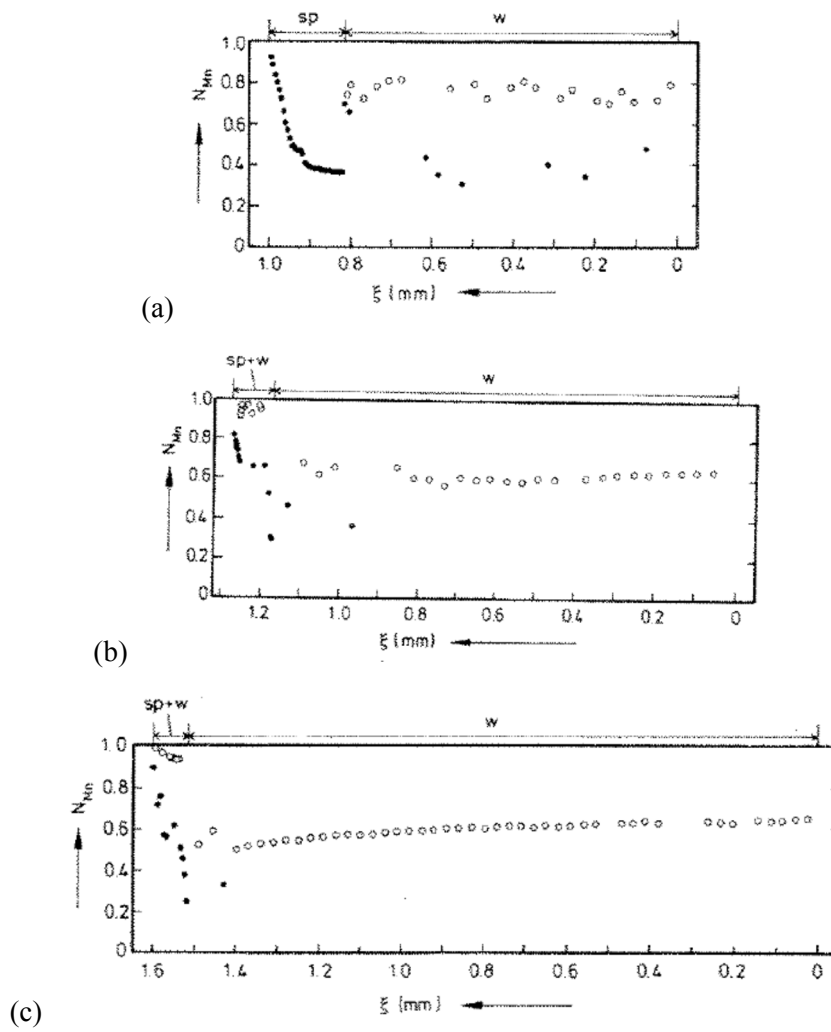


Fig. 2-9. The concentration profile of Mn after exposure of $(Mn_{0.6}Fe_{0.4})_{1-\delta}O$ to P_{O_2} gradients. The high P_{O_2} side (left side) is exposed to air while the low P_{O_2} side differed as follows: (a) $P_{O_2} = 3.1 \times 10^{-5}$ atm, 8 hours; (b) $P_{O_2} = 1.0 \times 10^{-5}$ atm, 3 hours; (c) $P_{O_2} = 1.6 \times 10^{-6}$ atm, 1 hour. (●): spinel; (○): wüstite. From Ueshima et al. [46]

is the same as a solid oxide fuel cell under working condition). Through similar treatment, it is shown that the cation profiles are governed by the ratio of their diffusion coefficients. Since cation diffusion is very slow, steady state can be reached in a reasonable duration only if the sample is very thin.

(ii) The treatment of cross effect

In 1989 Martin and Schmackpfeffer[48] reported the cross effect in trivalent B₂O₃-doped AO. Such case is different from homovalent solid solutions such as (Co,Mg)O in largely two ways; (i) The amount of dopant is low, generally about 5 m/o, i.e. complete solid solution is impossible, and (ii) strong interaction between the dopant ions and cation vacancies is possible, as speculated by Schmalzried and Laqua for (Ni_{1-x}Ti_{x/2})O. The theory on cross effect is better explained in the subsequent work by Martin[49] and is stated below. First the effect of cross effect in homovalent solution (A,B)O is discussed, followed by its effect in heterovalent solution.

The cross effect can be taken into account by the cross term L_{AB} in Onsager's matrix for the system. The fluxes of the chemical components can be written using the transport coefficients L_{ij} (i,j=A,B) as

$$j_A = -L_{AA} \nabla \mu_A - L_{AB} \nabla \mu_B, \quad (2-13a)$$

$$j_B = -L_{BA} \nabla \mu_A - L_{BB} \nabla \mu_B. \quad (2-13b)$$

By Onsager's reciprocity theorem, the two cross coefficients are equal, i.e. L_{AB}=L_{BA}. At steady state, by eq. (2-2) the two driving forces $-\nabla \mu_A$ and $-\nabla \mu_B$ are coupled as

$$\nabla \mu_B = \frac{(L_{AA} / L_{BB})c_B - (L_{BA} / L_{BB})c_A}{c_A - (L_{AB} / L_{BB})c_B} \nabla \mu_A = \Psi \nabla \mu_A. \quad (2-14)$$

Eq. (2-14) can further be modified to include the P_{O_2} gradient as driving force, for an ideal solution (A,B)O by local equilibria $A + 1/2O_2 = AO$ and $B + 1/2O_2 = BO$ as

$$\nabla_{X_B} = \frac{x_B(1-x_B)}{2} \frac{1-\Psi}{1-x_B(1-\Psi)} \nabla \ln a_{O_2} = \kappa \nabla \ln a_{O_2}. \quad (2-15)$$

Let us first consider the case where there is no cross effect, i.e. $L_{AB}=0$. According to the atomic theory self diffusion coefficients are given by

$$D_i = gs^2\omega_i x_v \quad (2-16)$$

where g is a geometrical factor dependent on the crystal structure, s the distance of individual atomic jump, ω_i the jump rate of species i and x_v the vacancy fraction. In this case Ψ becomes $D_A/D_B = \omega_A/\omega_B$ so eq. (2-15) is modified to

$$\left. \frac{\nabla_{X_B}}{\nabla \ln a_{O_2}} \right|_{L_{AB}=0} = \kappa_0 = \frac{x_B(1-x_B)}{2} \frac{1-\omega_A/\omega_B}{1-x_B(1-\omega_A/\omega_B)}. \quad (2-17)$$

Eq. (2-17) plainly states the conclusion obtained from the results by Schmalzried et al. - when $\omega_A > \omega_B$ (and therefore $D_A > D_B$) the faster component A is enriched at the high P_{O_2} side and vice versa. For the case where the cross effect prevails, Martin employed Manning's random alloy model[50] in which all transport coefficients are written in terms of the tracer diffusion coefficients (tracer diffusion coefficients are related to self diffusion coefficients as $D_i^* = D_i f_i$, with f_i the partial correlation factor). The cross coefficient L_{AB} is described in this model as

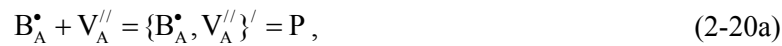
$$L_{AB} = \frac{1-f_0}{f_0 RT} \frac{c_A D_A^* \times c_B D_B^*}{c_A D_A^* + c_B D_B^*} \quad (2-18)$$

with f_0 the geometrical correlation factor which has the value 0.781 for a FCC lattice. The unmixing ratio κ as defined in eq. (2-15) can be calculated and is shown in Fig. 2-10 compared to κ_0 corresponding to the case $L_{AB}=0$. One can see that the sign of κ does not change, so the direction of unmixing remains the same. However, the magnitude of unmixing is decreased. Zhang and Murch[51] performed Monte Carlo simulation in (Co,Mg)O taking into account the cross effect. While their simulation results fit the experimental results obtained by Schmalzried et al., some disagreement rose in the frequency ratio ω_1 / ω_2 (and therefore the diffusion coefficient ratio). A possible reason would be the cross effect.

For a heterovalent doped oxide such as B_2O_3 -doped AO forming $(A_{1-x}B_x)_{1-\delta}O$ the story is more complicated. Assuming that the effect of intrinsic disorder (including electron-hole formation) is negligible compared to the doping effect and that the vacancies are fully ionized, the charge neutrality condition is written as

$$[B_A^\bullet] = 2[V_A^{//}] + [P] \quad (2-19)$$

where P is the dopant-vacancy associate formed by the reaction



$$K_p = \frac{[\{B_A^\bullet, V_A^{//}\}']}{[B_A^\bullet][V_A^{//}]} = \frac{[P]}{[B_A^\bullet][V_A^{//}]} \quad (2-20b)$$

The mass conservation for dopant B is given as

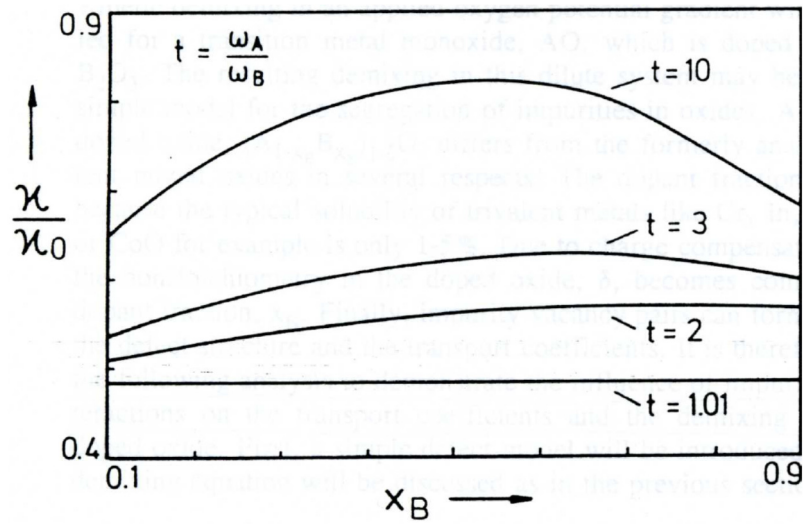


Fig. 2-10. Ratio of the demixing parameters κ ($L_{AB} \neq 0$) and κ_0 ($L_{AB} = 0$) as function of x_B for different ratios ω_A / ω_B . From Martin and Schmackpfeffer [48].

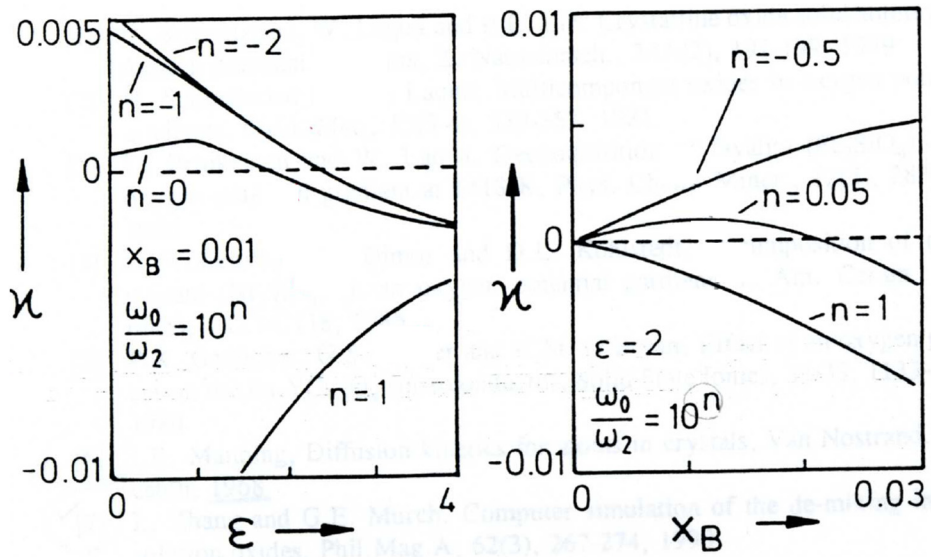


Fig. 2-11. The local unmixing ratio, κ , in a heterovalent doped oxide (a) as function of the binding energy ϵ for $x_B=0.01$ and different ratios ω_0/ω_2 and (b) as function of the dopant fraction x_B for $\epsilon=2$ and different ratios ω_0/ω_2 . From Martin and Schmackpfeffer [48].

$$x_B = [B_A^\bullet] + [P] \quad (2-21)$$

and oxygen exchange is done by



$$K_{ox} = \frac{[V_A^{//}]p^2}{a_{O_2}^{1/2}}. \quad (2-22b)$$

The defect fractions can be calculated as

$$[P] = \frac{1}{2K_p} + \frac{3}{4}x_B - \frac{1}{2}W \quad (2-23a)$$

$$W = \sqrt{\left(\frac{1}{K_p} + \frac{3}{2}x_B\right)^2 - 2x_B^2} \quad (2-23b)$$

$$[V_A^{//}] = \frac{1}{2}x_B - [P] \quad (2-23c)$$

$$[B_A^\bullet] = x_B - [P]. \quad (2-21')$$

As the chemical components and structure elements are related by local equilibria $A = A_A^\times - V_A^{//} - 2h^\bullet$ and $B = B_A^\bullet - V_A^{//} - 3h^\bullet$ and assuming ideal behavior for all structure elements,

$$\frac{\nabla\mu_A}{RT} = \alpha\nabla x_B - \frac{1}{2}\nabla \ln a_{O_2} \quad (2-24a)$$

$$\frac{\nabla\mu_B}{RT} = \beta\nabla x_B - \frac{3}{4}\nabla \ln a_{O_2} \quad (2-24b)$$

$$\alpha = -\frac{3}{2-3x_B} \quad (2-24c)$$

$$\beta = \frac{1+2W'}{4[B_A^*]} - \frac{1-2W'}{8[V_A^{//}]} \quad (2-24d)$$

$$W' = \frac{dW}{dx_B} \quad (2-24e)$$

By using the same methodology as in translating eq. (2-14) into eq. (2-15), eq. (2-24a) and (2-24b) can be combined with eq. (2-14) to result in an equation in the form of eq. (2-15), as

$$\kappa = \frac{3/4 - \Psi/2}{\beta - \alpha \Psi x_B} \quad (2-25)$$

To find the value of κ the jump rate of vacancies and therefore the transport coefficients must be known for this case. Because a dopant species is included in the matrix, there are various frequencies involved. Martin applied five-frequency model[52] wherein the impurity-vacancy interactions are considered but the influence of the impurity is limited to only the nearest neighbor. This model was simplified to include only three frequencies ω_0 (frequency of exchange of vacancy with A), ω_2 (frequency of exchange of vacancy with B) and ω_3 (frequency of exchange of vacancy with A and forming an impurity-vacancy pair). The derivation will not be done here and only the result are shown. The transport coefficients are given as

$$L_{AA} = \frac{2s^2\omega_0}{RT} [V_A^*] + \frac{s^2\omega_0}{6RT} \left(4 + 14t_1 - 2 \frac{(3t_1 - 2)^2}{2 + t_2 + t_1 F} \right) [P] \quad (2-26a)$$

$$L_{BB} = \frac{s^2\omega_2}{6RT} \frac{2 + 7t_1 F}{2 + 2t_2 + 7t_1 F} [P] \quad (2-26b)$$

$$L_{AB} = L_{BA} = \frac{s^2\omega_2}{6RT} \frac{6t_1 - 4}{2 + 2t_2 + 7t_1 F} [P] \quad (2-26c)$$

with $t_1 = \omega_3 / \omega_0$ and $t_2 = \omega_2 / \omega_0$, s the jump distance and F a constant. By observing eq. (2-26) one can see that the magnitude of L_{AB} can be comparable to L_{BB} , i.e. the cross effect cannot be neglected. The values of κ for this case are shown in Fig 2-11. For moderate binding energy of impurity-vacancy pair (ε), $\kappa > 0$ so the B cation is enriched at the high P_{O_2} side. When the binding energy becomes larger, the impurity moves with the vacancy to the low P_{O_2} side, enriching it with B cations, no matter which cation has higher exchange frequency with vacancies.

This theoretical treatment was experimentally confirmed by a later work involving Ga_2O_3 -doped CoO[53]. Compared with the tracer diffusion study on the same material system[54], the ratio of cross to direct coefficient, L_{AB}/L_{BB} , was found to be -1.6. This means that not only is cross effect not negligible, it may actually be larger in effect than the direct transport. To summarize the work by Martin et al. on cross effect, in homovalent oxides cross effect does not affect the directionality of unmixing; it only reduces the extent of unmixing. However, for heterovalent oxides, the dopants may interact strongly with the cation vacancies and even the directionality may be overturned by cross effect.

(iii) The treatment transient state and numerical calculation

Various works have been done on the numerical treatment of kinetic unmixing under P_{O_2} gradient. All in all the models incorporate the theories described up to now and combine it with the continuity equation $\partial c_k / \partial t = -\nabla \cdot j_k$. The method for numerical calculation itself will not be explained in detail here and the reader is referred to the literature[55-61].

(iv) Kinetic decomposition

The first report on kinetic decomposition under P_{O_2} gradient was by Schmalzried et al.[43] on $NiTiO_3$ and Co_2TiO_4 , as mentioned before. Since then, few more works

on kinetic decomposition were performed. As this part is the main theme of this thesis, the phenomenological results will be introduced in this section. Theoretical considerations will be given in the following Chapters. It will be stated at this point that the critical driving force is related to the Gibbs free energy of formation of the compound.

The first system was the olivine Ni_2SiO_4 , reported by Wolfenstine et al.[62] and Jacob and Shukla[63]. From self-diffusion measurements it has been known that in silicates the divalent cations are much more mobile than both oxygen and silicon[64,65]. After exposure under Po_2 gradient, both literatures reported that NiO layer was formed at the high Po_2 side and SiO_2 was formed at the low Po_2 side. A typical composition profile is given in Fig. 2-12. The work by Jacob and Shukla was more in depth, as Wolfenstine et al. only reported the results for a single Po_2 ratio ($\text{Po}_2''=0.21$ atm, $\text{Po}_2'=3.1 \times 10^{-4}$ atm), while Jacob and Shukla showed the results for various Po_2 ratios. Since Ni_2SiO_4 is a stoichiometric compound with narrow stability range, the experiments with Po_2 ratio smaller than the critical ratio showed virtually uniform chemical composition throughout the specimen, i.e. the unmixing effect was practically undetectable. This does not mean that kinetic unmixing did not occur. Rather, it means that the extent of unmixing is so small that it is overshadowed by errors occurring from compositional analysis.

A unique feature in Jacob and Shukla's work is that the critical Po_2 ratio seemed to be a function of the average Po_2 in which the specimen is situated in. For example, for samples with $\text{Po}_2''=1$ atm and $\text{Po}_2'=0.04\sim 0.90$ atm, the critical Po_2 ratio $\text{Po}_2'' / \text{Po}_2' |_{\text{crit}}$ was found to be 1.63 while for samples with $\text{Po}_2''=1.87 \times 10^{-8}$ atm and $\text{Po}_2'=1.17 \times 10^{-8} \sim 2.67 \times 10^{-9}$ atm the critical ratio is 2.16. This difference is probably due to the Po_2 dependence of the diffusion coefficients. This will again be treated further later in Chapter 4.

Similar results were found independently in the fayalite Fe_2SiO_4 by Weghöft and Schmalzried[66] and Brinkmann and Laqua[67]. As the divalent cations are much more mobile than tetravalent cations, FeO wüstite is expected to be found at the high Po_2 side and SiO_2 at the low Po_2 side, which was exactly the result, as shown in Fig. 2-13 (a). Brinkmann and Laqua, like Jacob and Shukla, performed unmixing experiment in two different atmospheres and confirmed the difference of critical Po_2 ratio according to the average Po_2 value (experiment 1: $\text{Po}_2'' = 5.01 \times 10^{-12} \sim 3.24 \times 10^{-13}$ atm, $\text{Po}_2' = 1.26 \times 10^{-13}$ atm, $\text{Po}_2'' / \text{Po}_2' |_{\text{crit}} = 7.1$; experiment 2: $\text{Po}_2'' = 1.62 \times 10^{-11} \sim 5.89 \times 10^{-12}$ atm, $\text{Po}_2' = 2.88 \times 10^{-12}$ atm, $\text{Po}_2'' / \text{Po}_2' |_{\text{crit}} = 2.28$). They found decomposed phases of "FeO" and SiO_2 , while Weghöft and Schmalzried found instead Fe_3O_4 and SiO_2 . This is because the experiment by Brinkmann and Laqua was performed at reducing atmospheres where $\text{Fe}_{1-\delta}\text{O}$ is stable ($\log(\text{Po}_2/\text{atm}) < -10$ at 1418 K), while Weghöft and Schmalzried performed their experiment at higher Po_2 where $\text{Fe}_{3-\delta}\text{O}_4$ is stable. However this result may be flawed because their experiment was performed at 1130°C with higher Po_2 at $\text{Po}_2'' = 3.55 \times 10^{-11}$ atm, which falls into the phase stability field of $\text{Fe}_{1-\delta}\text{O}$ [68]. Weghöft and Schmalzried also reported the unmixing phenomenon in olivine $(\text{Fe}_x\text{Mg}_{1-x})_2\text{SiO}_4$ with fayalite enriching at the high Po_2 side and Mg_2SiO_4 at the low Po_2 side, which is acceptable as $D_{\text{Fe}}/D_{\text{Mg}} \sim 3.6$. (Fig. 2-13 (b))

Azubike et al.[69] showed kinetic decomposition of nickel titanate NiTiO_3 (same as Schmalzried and Laqua[43]) and nickel tungstate NiWO_4 under Po_2 gradient. The result in NiTiO_3 was analogous to that by Schmalzried and Laqua, i.e. NiO was formed at the high Po_2 side and TiO_2 at the low Po_2 side, as shown in Fig. 2-14. The analysis for NiWO_4 is not quite complete, as only NiO and NiWO_4 were detected after experiment. NiO was found at the low Po_2 side, indicating that W is faster than Ni. However, using their Po_2 ratio, it is expected that Ni is about twice faster than W. There was no clear explanation of the reason for this opposite tendency. Also, WO_3 was detected only to a trace level. They explain this by the

possibility of sublimation of WO_3 , as WO_3 is known to be volatile at temperatures above 1000°C [70] although its melting point is above 1400°C [71]. This however is not conclusively confirmed.

For the system of $\text{La}_2\text{NiO}_{4+\delta}$, Cebasek et al.[72] showed that NiO was found in trace at the high Po_2 side, while the low Po_2 side showed no phase decomposition (Fig. 2-15). Through their previous work on solid state reaction between NiO and La_2O_3 [73], Ni was much faster than La in La_2NiO_4 . A possible reason for the non-detection of La_2O_3 is that it may have been segregated at the grain boundaries under the detection limit. However, because the exact ratio is not determined, further analysis was not possible. The electron probe microanalysis profiles showed no detectable unmixing or decomposition.

From here on the research on kinetic decomposition shifts from systematic study to phenomenological studies in devices, such as oxygen permeation membranes and solid oxide fuel cell (SOFC) cathodes, which employ complex perovskite-based oxides. Van Doorn et al.[74] showed possible kinetic unmixing and decomposition in SrO-doped lanthanum cobalt oxide ($\text{La}_{0.3}\text{Sr}_{0.7}\text{CoO}_{3-\delta}$), shown in Fig. 2-16. The result was that Sr-rich phases appeared at the low Po_2 side (O_2 content of 1.4%), in the form of SrCO_3 , which probably is an offspring of SrO, as the authors speculate that it was formed after cooling to room temperature and exposing to air. If the Po_2 was controlled by CO/CO_2 mixtures, then SrCO_3 definitely would have formed even during experiment, but it was controlled by O_2/Ar mixture, so the origin of SrCO_3 would be the exposure after cooling. This is contradictory from another experiment done on $\text{La}_{1-x}\text{Ca}_x\text{CrO}_{3-\delta}$, where CaO was found to segregate at the high Po_2 side[75]. The authors failed to provide any reason for the sluggish behavior of Sr cations.

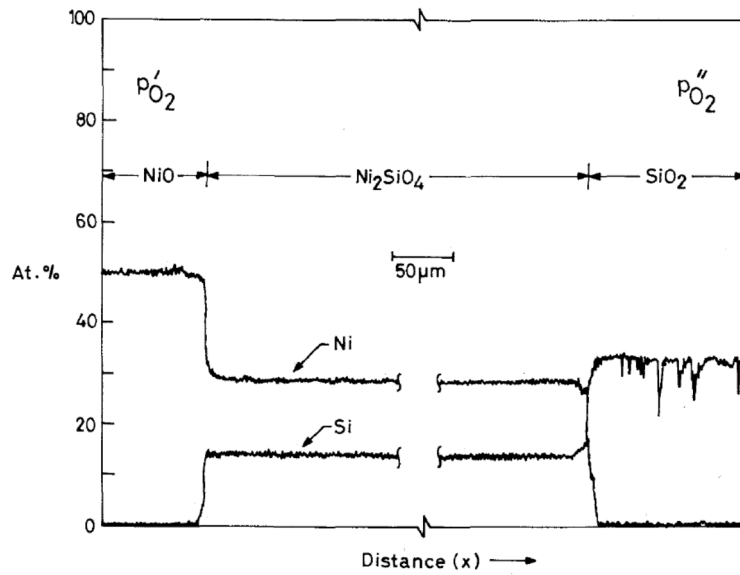


Fig. 2-12. Composition profile across the Ni_2SiO_4 disk after kinetic decomposition obtained by EPMA. From Jacob and Shukla [63]. Actual experimental conditions not indicated.

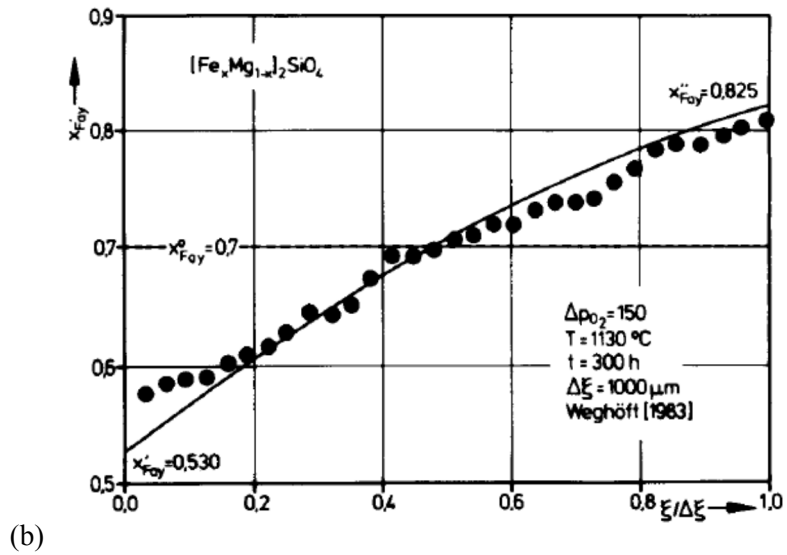
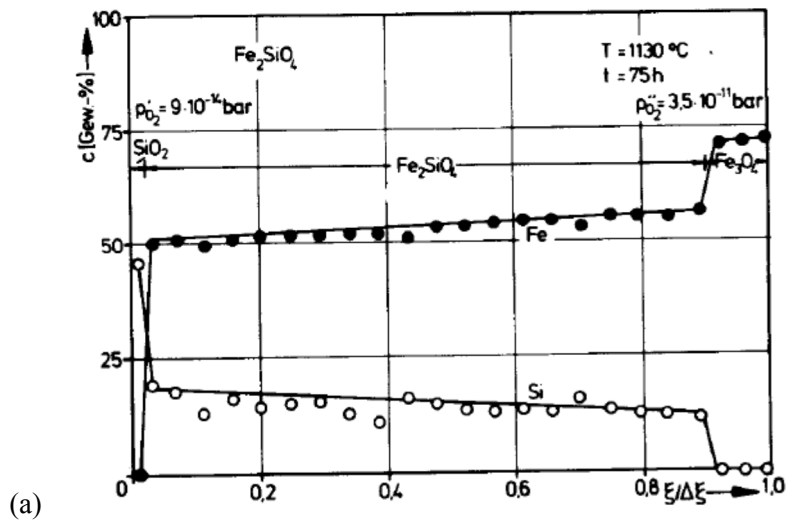


Fig. 2-13. The experimental steady state demixing profiles of (a) fayalite at 1130°C and $a''_{O_2} / a'_{O_2} = 390$ and (b) olivine $(Fe_xMg_{1-x})_2SiO_4$ at 1130°C and $a''_{O_2} / a'_{O_2} = 150$. From Weghöft and Schmalzried [66].

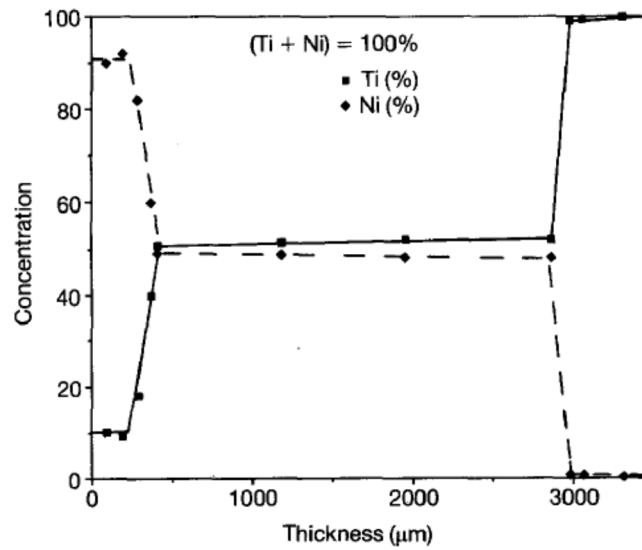


Fig. 2-14. Multiphase layer formed by exposing a single-phase NiTiO_3 to an oxygen potential gradient between 2.13×10^4 Pa (left) and 7.234 Pa (right) at 1450°C . From Azubike et al. [69]

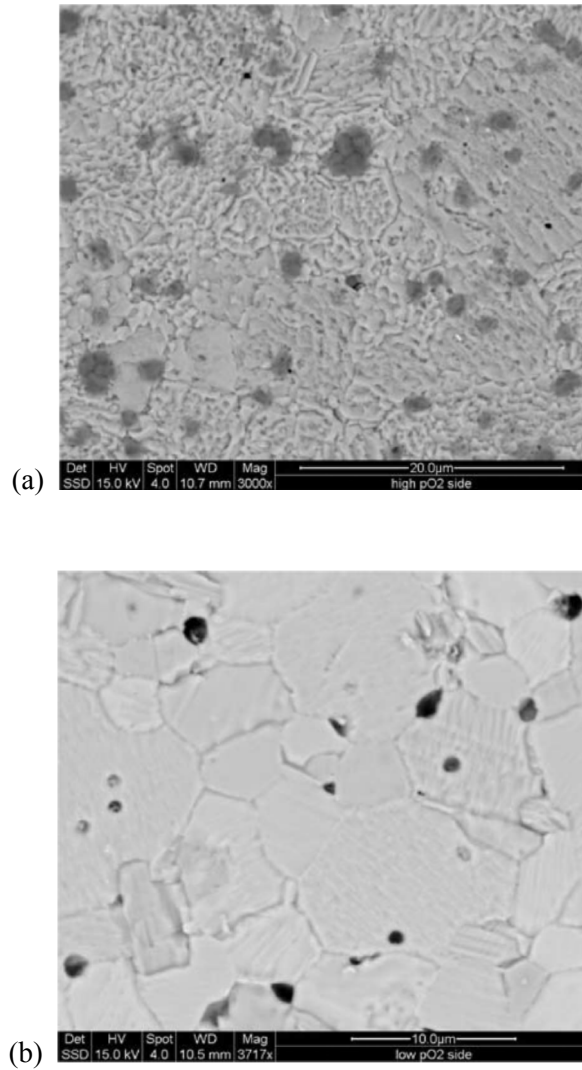


Fig. 2-15. SEM backscattered image of the (a) high Po_2 side and (b) low Po_2 side of the La_2NiO_4 membrane after annealing at 1000°C for 800 hours. The dark spots in (a) represent the decomposition product NiO . The dark spots in (b) are pores and no phase change was detected. From Cebasek et al. [72]

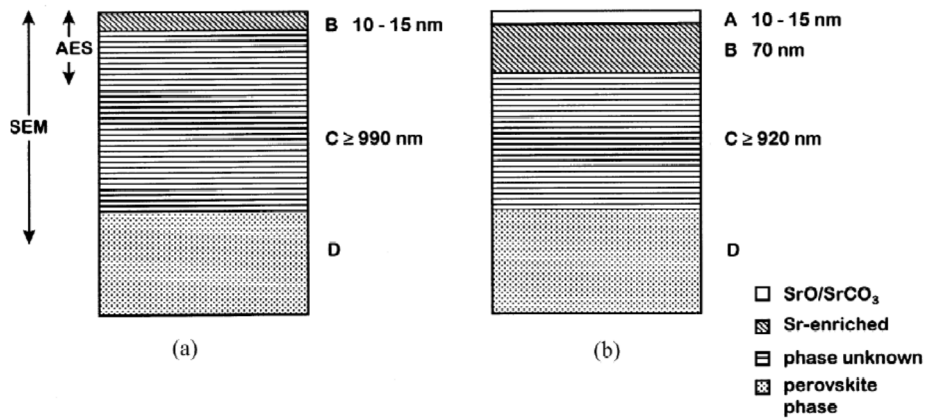


Fig. 2-16. Schematic illustration of the formation of different zones at the oxygen lean-side of permeated $\text{La}_{0.3}\text{Sr}_{0.7}\text{CoO}_{3-\delta}$ disks. (a) Disk permeated during 120 hours at 900°C in a gradient of air vs. 1.4% O_2 and (b) permeated for more than 500 hours at temperatures $900\sim 1100^\circ\text{C}$. From Van Doorn et al. [74]

For these high order perovskites, no theoretical considerations have been given. Only experimental results based on composition profiles are given. It is much more difficult to systematically examine kinetic unmixing and decomposition in these more complex oxides because (i) the dopants affect the diffusion coefficients and (ii) the products of decomposition are unclear. For example, for a system $(A,A')(B,B')O$, the decomposition products can be of any combination of $(AO$ or $A'O)-(BO$ or $B'O)$ or, if various intermediate compounds exist, a combination of intermediate compounds. Especially, if these intermediate compounds have similar crystal structure, it is more difficult to separate them by methods such as XRD. Therefore there has not been a systematic research for these systems although these are the real systems where such research is needed. Therefore, they should be tackled in the future work. For the literature reporting the phenomena the readers are referred to the following references for the respective systems: $La_{0.5}Sr_{0.5}Fe_{1-x}Co_xO_{3-\delta}$ [76], $La_{0.6}Sr_{0.4}Co_{0.2}Fe_{0.8}O_{3-\delta}$ [77-79], and $Ba_{0.5}Sr_{0.5}Co_xFe_{1-x}O_{3-\delta}$ [80].

(b) Electric field

The research on the effect of electric field on kinetic unmixing and decomposition are less in number compared to the Po_2 case. According to the literature, Bray and Merten[81] were the first to raise the possibility of kinetic unmixing in doped zirconia (although in doped zirconia it is very hard to observe kinetic unmixing since the majority defects lie on the oxygen sublattice, as mentioned before). The first quantitative work was done by Monceau et al.[82] in 1994, followed by Teller and Martin[83] in 1997. The theoretical treatment is analogous to the Po_2 case but there are some differences, especially in the final steady state solution.

Like the Po_2 case, let us first begin with a homovalent $(A,B)_{1-\delta}O$, in which the majority defects are cation vacancies and electron holes. We assume that cross effect can be neglected. The greatest difference we must consider compared to the Po_2 case is the existence of electrodes. The electrodes must be reversible to both oxygen ions and electron holes (or electrons). If the electrodes are blocking with

respect to oxygen ions, then oxygen concentration gradient will build up inside the specimen which will act as an additional indirect driving force, i.e. the driving force will not be electric field any more. The electrodes are blocking for cations (or else there would not be concentration gradient build up and therefore no kinetic unmixing or decomposition). When we apply an external electrostatic potential gradient $\nabla\phi$ to the specimen, the electrochemical potential gradient of electron holes will be given as $\nabla\eta_h = F\nabla\phi$. Assuming the local equilibria prevail and that (A,B)O acts as an ideal solution of components AO and BO, eq. (2-3) which describes the flux of cations, can be written for the cations as

$$j_A = -\frac{D_A x_A}{V_m} \left(\frac{\partial \ln x_A}{\partial \xi} + \frac{z_A F}{RT} \frac{\partial \phi}{\partial \xi} \right) \quad (2-27a)$$

$$j_B = -\frac{D_B x_B}{V_m} \left(\frac{\partial \ln x_B}{\partial \xi} + \frac{z_B F}{RT} \frac{\partial \phi}{\partial \xi} \right). \quad (2-27b)$$

By comparing with eqs. (2-6a) and (2-6b), one can see that the difference lies in the second term in the parentheses. Inserting eqs. (2-27a) and (2-27b) into the steady state condition eq. (2-2), the following steady state equation is derived:

$$dx_A = \frac{x_A(1-x_A)(z_B D_B - z_A D_A)}{(1-x_A)D_A + x_A D_B} \frac{Fd\phi}{RT} \quad (2-28)$$

assuming $x_A + x_A = 1$, i.e. the fraction of vacancies is very small.

Let us compare eq. (2-28) with eq. (2-7), the steady state equation under P_{O_2} gradient. If we take, as in the homovalent oxide (A,B)O, $z_A = z_B = z$, the resulting equation is

$$dx_A = \frac{\gamma - x_A}{x_A(1 - x_A)} \times \frac{1}{z} \frac{Fd\phi}{RT} \quad (2-29)$$

which is the exact form as eq. (2-7). The result becomes different when the cations are heterovalent as the formal charges are no longer taken to be the same. Whereas the local ratio of *self* diffusion coefficients of cations was the key factor in determining the steady state profiles in the Po₂ case, the local ratio of *electrochemical* mobilities, defined as $z_k D_k$ for component k, rules the kinetic phenomena in the electric field case. Also, looking at eq. (2-28), we can see that the cation with higher electrochemical mobility is concentrated at the (-) side, or where the electrostatic potential is lower. This migration of the faster cation towards the (-) side is obvious, as cations with their positive charge would migrate from (+) to (-) side. The unmixing occurs because of the difference in the mobility of each cation sublattice, or their jump frequencies. This is analogous to the Po₂ case.

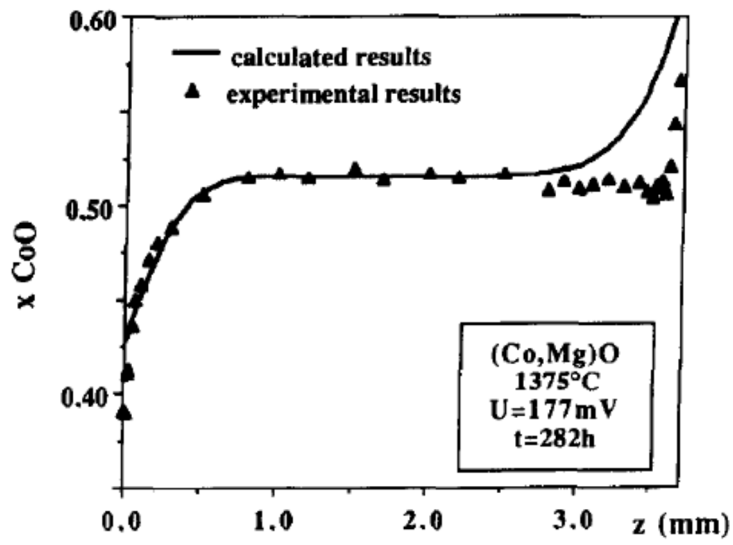
Monceau et al., based on the theoretical basis described above, conducted unmixing experiment on (Co,Mg)O under electric field (Fig. 2-17 (a)). While the calculated results complied with experimental results well enough, a discrepancy occurred near the cathode ((+) electrode). The authors explained this by internal short circuits between the cathode and the surface which lead to rehomogenization of the material.

Similar experiment was conducted on 9 m/o yttria-doped zirconia (YSZ) (Fig. 2-17 (b)). There are at least two great differences between (Co,Mg)O and YSZ. Number one is that (Co,Mg)O is a homovalent system, while YSZ is heterovalent since Y³⁺ is trivalent. However, a more important difference is that doped zirconia is an oxygen conductor, i.e. the majority defects lie on the oxygen sublattice and cations are virtually immobile. In the experimental condition of Monceau et al., the majority defects in YSZ are Y'_{Zr} and $V_{O}^{\bullet\bullet}$, with oxygen vacancy being the mobile defect as fluorite structure allows high oxygen mobility (whereas in rock salt

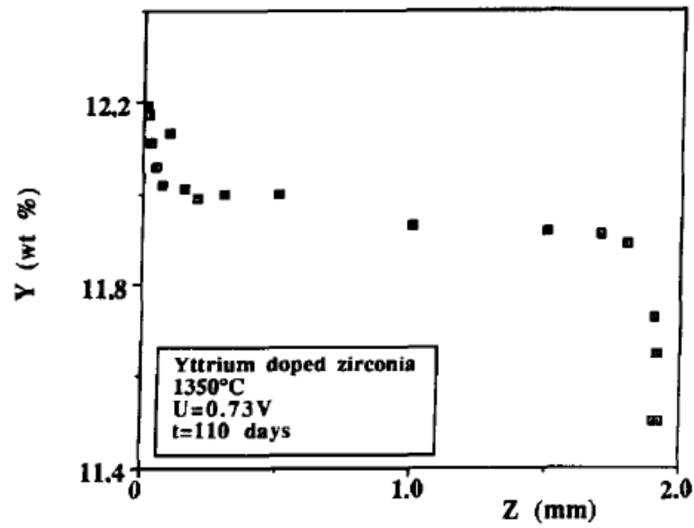
structure oxygen is virtually immobile, as is the case for (Co,Mg)O). Therefore, even when kinetic unmixing or decomposition occurs, a much longer time will be required for the phenomena to occur and reach steady state. To reflect this, (Co,Mg)O was put under electric field for 282 hours, while YSZ was put under for 110 days. However, the results for YSZ were not what the authors expected. According to literature, yttrium ion was found to have higher diffusion coefficient than zirconium ion in YSZ. Even considering their formal charges, the electrochemical mobility of yttrium is about twice that of zirconium. Therefore Y was expected to be enriched at the (-) electrode. However, it was found to be enriched at the (+) electrode, indicating that Zr is faster than Y. The authors speculated that the cation diffusion coefficients were inaccurate, but could not give conclusive proof and no further analysis was performed.

Teller and Martin showed unmixing under electric field for the homovalent system of (Co,Ni)O, where Co is faster than Ni[84]. This was confirmed by the cation profiles after unmixing experiment (Fig. 2-18). Using the calculation approach previously shown by Schmalzried et al. under P_{O_2} gradient[40], they calculated the steady state profiles and compared with the experimental results. Although no graphical proof was shown, it seems that they differed considerably because their experiment had not yet reached steady state - in fact, both Teller and Martin's work and the work by Monceau et al. were both not yet in steady state. The time required to reach steady state (the "relaxation time") was proposed by Schmalzried[85] and can roughly be represented as $\tau = (\Delta\xi)^2 / 2\overline{D}_{Me}$, where $\Delta\xi$ is the specimen thickness and \overline{D}_{Me} is the average diffusion coefficient of the metal cations. According to this equation, for example, the result of Monceau et al. on YSZ would require 10^5 years to reach steady state.

From the result of Monceau et al. on YSZ, where the faster species (or what was expected to be the faster species) was found at the (+) side, one can naturally recall



(a)



(b)

Fig. 2-17. The composition profiles of (a) (Co,Mg)O and (b) YSZ under electric field. From Monceau et al. [82]

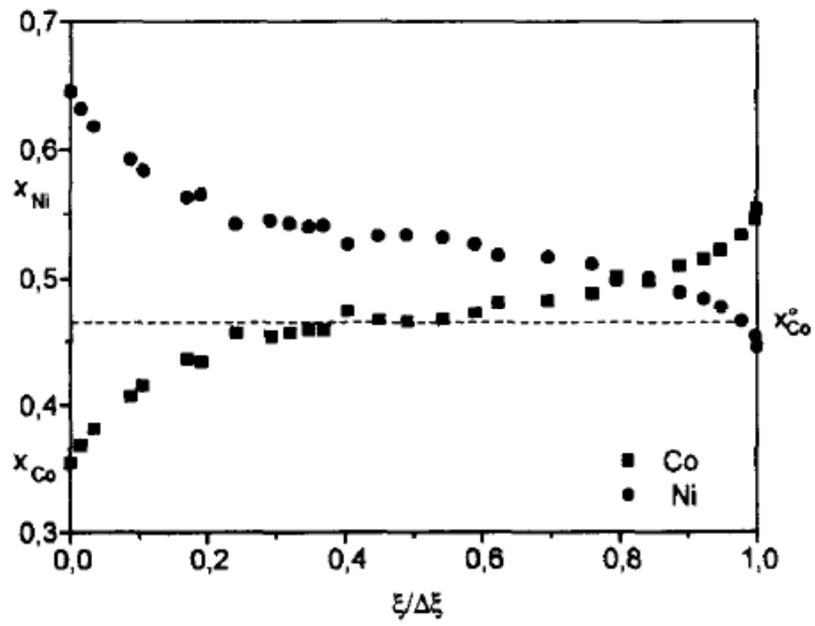
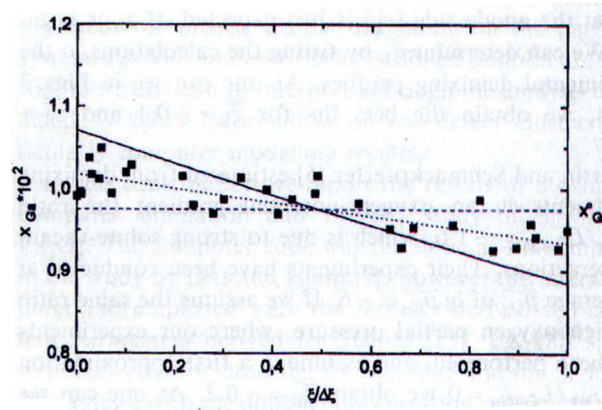
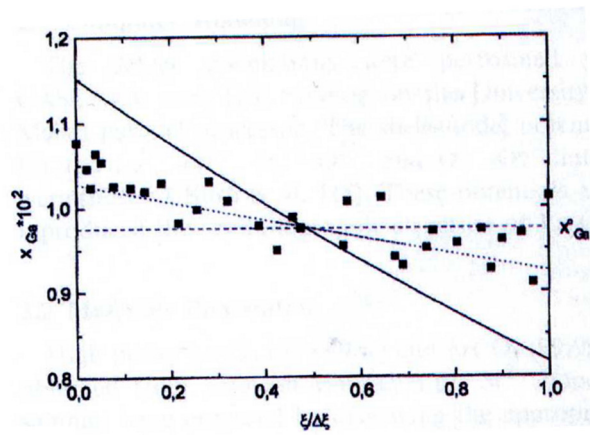


Fig. 2-18. Unmixing profile of Co and Ni in (Co,Ni)O under electric field of 275 mV for 480 hours. Left side is anode and right side is cathode. From Teller and Martin [83].



(a)



(b)

Fig. 2-19. Unmixing profile of Ga in (Co,Ga)O at (a) 225 mV and $\bar{z}_B = -0.1$, and (b) 450 mV and $\bar{z}_B = -0.07$. From Teller and Martin [86].

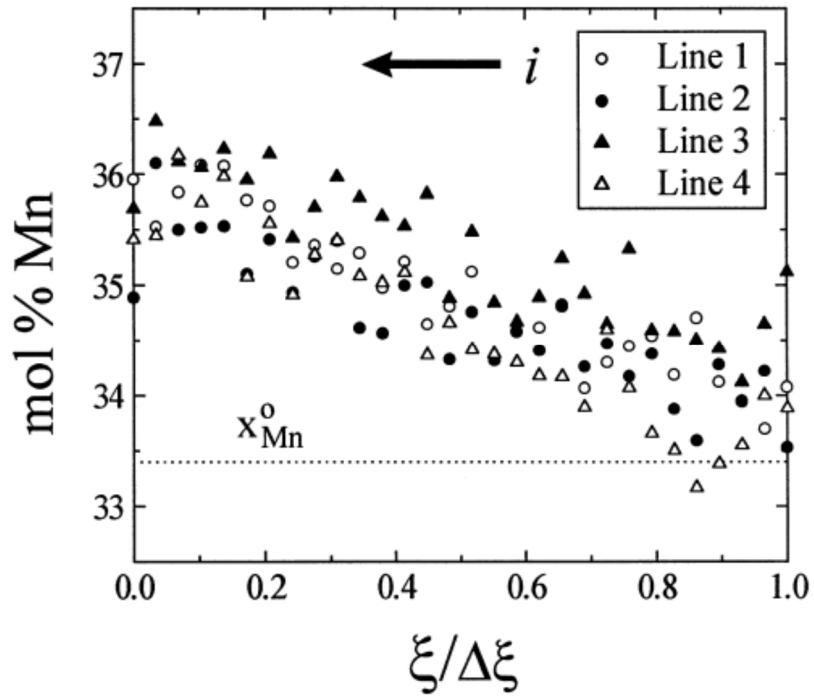


Fig. 2-20. Composition distribution (Mn) vs. relative distance from the cathode to the anode. From Hong and Yoo [87].

the cross effect which was shown for the Po_2 case for the system of $(\text{Co,Ga})\text{O}$. Teller and Martin in their subsequent article[86] reported the unmixing results of $(\text{Co,Ga})\text{O}$ under electric field and analyzed the results again with five-frequency model (Fig. 2-19). According to their analysis, the unmixing profile is decided by the apparent effective charge of the solute species B. This effective charge is defined as

$$\bar{z}_B = 3 + 2 \frac{L_{AB}}{L_{BB}} + \frac{L_{Bh}}{L_{BB}} \quad (2-30)$$

where L_{AB} is the cross effect between A and B and L_{Bh} the cross effect between B and electron holes. If there is no cross effect between B and A or electron holes, then B will be trivalent. However, as we had seen for the Po_2 gradient case, $L_{AB}/L_{BB}=-1.6$, so the effective charge of Ga in $(\text{Co,Ga})\text{O}$ would be less than 3, and even be negative depending on the cross effect between B and electron holes. In the experiment \bar{z}_B was found to be about -0.1 (although the concentration profiles are quite scattered due to the small concentrations of Ga, $x_{\text{Ga}}^0 = 0.975$ m/o), indicating that $L_{Bh}/L_{BB} \sim 0.1$, indicating that the cross effect between B and electron holes cannot be neglected. The positive value of L_{Bh}/L_{BB} means that the defect associate $\{\text{Ga}^{\bullet}, \text{V}^{//}\}'$ attracts electron holes and creates neutral defect associate. As the effective charge of Ga is negative, it is concentrated at the (+) electrode.

The authors in the literatures up to this point had performed their experiments in potentiostatic manner, i.e. constant voltage was applied through the outer probes. However, galvanostatic experiments (i.e. constant current is applied) may also be used. In the spinel system $(\text{Mn}_x\text{Fe}_{1-x})_3\text{O}_4$ Hong and Yoo[87] performed galvanostatic electrotransport and observed kinetic unmixing (Fig. 2-20). They derived the steady state equation including the cross coefficients as

$$\frac{F \times i / \sigma}{RTVx_A} = \frac{\frac{L_{11}}{x_A} + \frac{x_A}{x_B} \frac{L_{22}}{x_B} - \frac{2L_{12}}{x_B}}{x_A \left(\frac{z_1 L_{11} + z_2 L_{12} - L_{13}}{x_A} - \frac{z_1 L_{21} + z_2 L_{22} - L_{23}}{x_B} \right)} \quad (2-31)$$

where i is the applied constant current density and σ the total conductivity of the semiconducting specimen. The suffix 1 indicates A (Fe), 2 B (Mn) and 3 electrons. If the cross coefficients are neglected, eq. (2-31) is reduced to eq. (2-28). In the experiment they found that Mn was saturated at the (-) side, in accordance with the fact that $D_{Mn}/D_{Fe}=2$ in the thermodynamic conditions of the experiment. In analyzing, they neglected the cross coefficient L_{12} since both cations supposedly have equal formal charge. In this case the charge of transport $\alpha_k^* = L_{k3} / L_{kk}$ ($k=1,2$) which indicates the number of electrons dragged by a type k cation upon its transfer in the absence of its own driving force, becomes critical, as was shown for the system of $Co_{1-\delta}O$ [88]. The charge of transport for this case was in the range of 1.2~1.5. Such cross effect would decrease the steady state concentration gradient as the effective charge of the cations would decrease from 8/3 to about 1.17~1.47, which is in accordance with the experimental results. However, the effect of cross coefficient L_{12} should be further analyzed for better analysis.

An interesting literature is provided by Yoo et al.[26] on La-doped $BaTiO_3$. In this work electric field was applied to La-doped $BaTiO_3$, to the extent in which kinetic unmixing and even decomposition is expected. The basis of this speculation will be provided later in Chapter 4. In Fig. 2-21, one can see that electrotransport occurred, from the microstructure change at the cathode (Fig. 2-21 (a)) and anode (Fig. 2-21 (b)). However, despite applying such large driving force, neither kinetic unmixing nor decomposition occurred (Fig. 2-22). The only possible reason the authors could give was that the A-site barium and B-site titanium ions migrated with equal electrochemical mobility, i.e. $z_A D_A = z_B D_B$. This conclusion is yet to be confirmed, but it is a good possibility. However, would this be the only possibility? Further

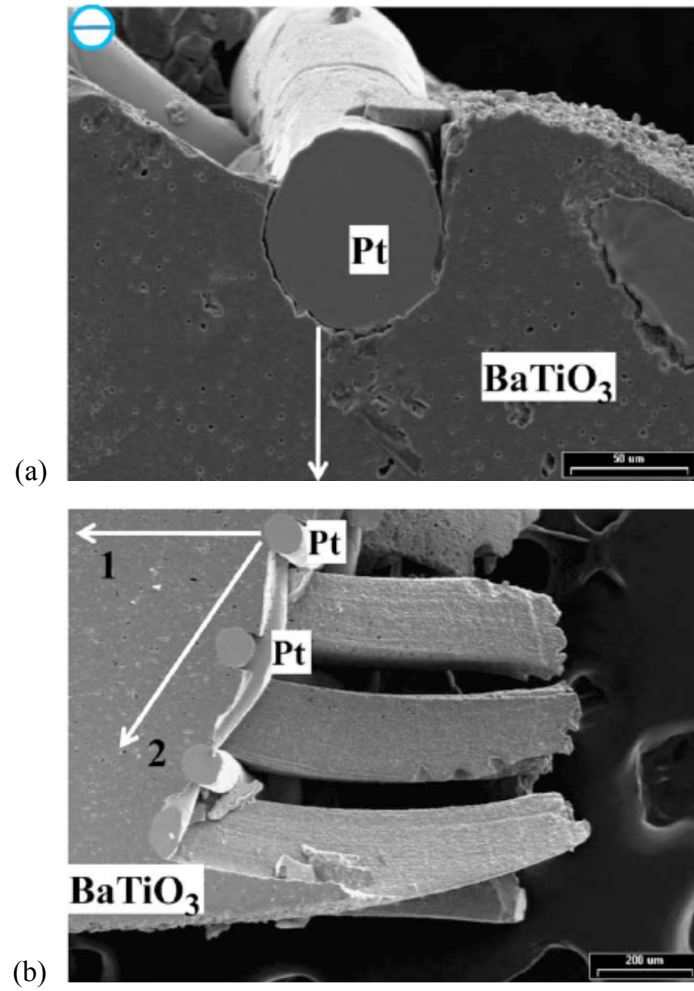
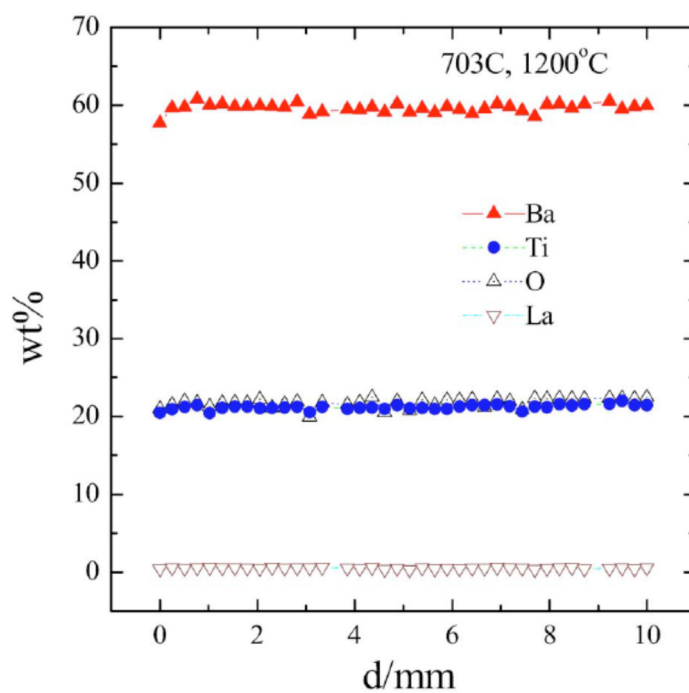
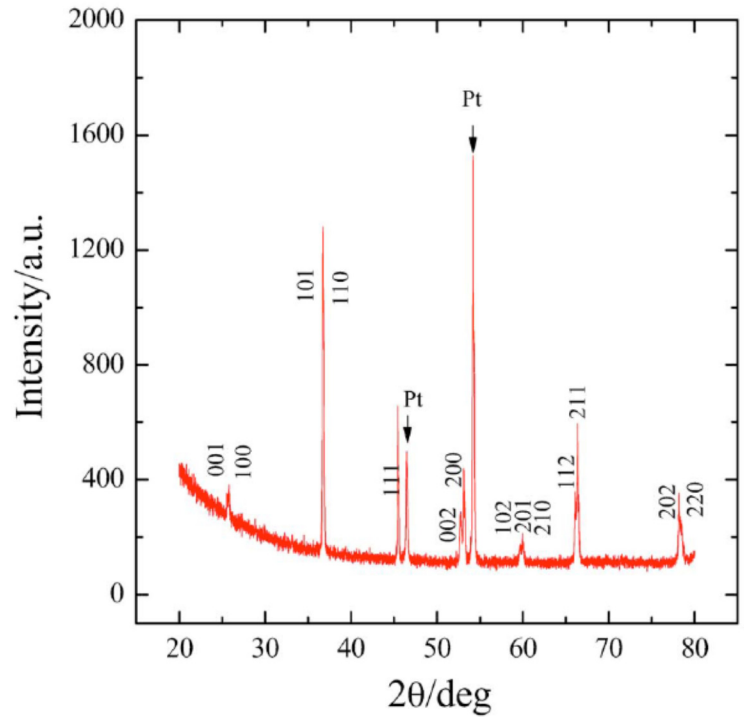


Fig. 2-21. (a) The cathode vicinity of La-doped BaTiO₃, after passing 703 C at 1200°C in air. (b) The anode vicinity of La-doped BaTiO₃, after passing 1161 C at 1200°C in air. One can see that in (a) the novel lattice grows around the Pt cathode, while in (b) the Pt anode penetrates into the lattice. From Yoo et al. [26]



(a)

Fig. 2-22. (a) The electron probe microanalysis (EPMA) profile showing the distribution of Ba, Ti, O and La as measured from anode to cathode, along the white arrow in Fig. 2-21 (a). (b) The x-ray diffraction pattern obtained from the cathode surface of the oxide in Fig. 2-21. All the peaks are assigned to the perovskite BaTiO_3 . There is virtually no gradient in the EPMA profile and no decomposed phase in the XRD pattern. From Yoo et al. [26] (Continued in the next page)



(b)

(continued) Fig. 2-22. (a) The electron probe microanalysis (EPMA) profile showing the distribution of Ba, Ti, O and La as measured from anode to cathode, along the white arrow in Fig. 2-21 (a). (b) The x-ray diffraction pattern obtained from the cathode surface of the oxide in Fig. 2-21. All the peaks are assigned to the perovskite BaTiO_3 . There is virtually no gradient in the EPMA profile and no decomposed phase in the XRD pattern. From Yoo et al. [26]

issues concerning this work and perovskites will be given later in Chapter 4.

As in the case of P_{O_2} gradient, various attempts have been made to conduct numerical calculation of the transient concentration profiles under electric field. The readers are again referred to the respective literature[61,89-91]. An interesting point is that no result on kinetic decomposition under electric field has ever been reported.

As stated before, there has been no effort at deriving the critical voltage required for decomposition to occur. Probably the only work in literature that could be found concerning the decomposition voltage is that done by Gibbs, resulting in the Gibbs theorem for electric work. When two half cell reactions are combined to form a galvanic cell, the cell performs electrical work, or produces electromotive force. The electromotive force is related to the Gibbs free energy change of the reaction (which is the sum of the two half cell reactions) by the famous Gibbs theorem which is given as

$$\Delta G = -nFE . \quad (2-32)$$

Here, the electrical work done by the system is designated as positive, resulting in a negative Gibbs free energy. n refers to the number of electrons that are required to perform the cell reaction. This equation was derived by Gibbs in 1876[92] with emphasis on electrical work. It will be shown in Chapter 4, however, that this theorem is insufficient in treating the current problem. A brief account is given below.

If Gibbs theorem could be applied to a ternary oxide electrolytic cell, then the decomposition voltage will be given by eq. (2-32). Looking at Gibbs' definition, Gibbs stated that the electromotive force was the difference of the potential of an ion. However, in ternary oxides there are multiple ions with the same polarity,

which means that the definition of electromotive force given by Gibbs may not be fit to describe in ternary oxides. Therefore the Gibbs theorem, which is the only equation that could be found dealing with decomposition voltage, may not be applicable for ternary oxides or higher. This is aptly shown for the system BaTiO₃ mentioned before. According to thermodynamic data, the decomposition voltage would be about 750 mV for BaTiO₃ at 1200°C with n=2 (the decomposition voltage would be higher with smaller n. n in this case would be either 2 or 4, depending on which ion is the carrier). However, even at applied voltage of c.a. 2.5 V, no decomposition occurred, signifying that Gibbs theorem is not applicable.

(c) Temperature gradient and stress field

Another thermodynamic driving force that can be applied to induce kinetic unmixing or decomposition is temperature gradient. Petuskey and Bowen[93] seem to be the first to report such phenomenon in oxides. There are basically two mechanisms perceived in inducing kinetic unmixing. The first is, simply put, the difference in cation mobilities, and the second is the interaction between the flow of thermal energy and the flow of ions, which is termed the "heat of transport." In a spinel system Fe(Fe_{1.51}Al_{0.49})O₄ (written to indicate the A and B sites) they performed two different experiments - (i) open surface and (ii) closed surface with respect to oxygen transport (done by wrapping the specimen surface with Pt foil). Through the result it was found that unmixing occurs almost solely by the cation mobility difference. Heat of transport was found to have negligible effect.

Other than this, reports on experimental results are scarce. Timm and Janek[94] found demixing under Soret conditions (closed system) in Cu_{2-δ}O system, but as one can see this is not a ternary system - rather, it should be described as the nonhomogenization of nonstoichiometry by thermal gradient. Theoretical considerations and numerical calculations can be found in the works of Akbar et al.[95] and Monceau et al.[96]

Under stress gradient Dimos et al.[97] derived theoretically the unmixing profile and the critical stress for kinetic decomposition to occur under nonhydrostatic stress. The treatment is analogous to that done by Schmalzried et al. for P_{O_2} gradient and will not be discussed here. However, no experimental results had been found. High pressure decomposition is important in the field of geophysics[98,99], but this type of decomposition is of thermodynamic nature, not a kinetic one.

Up to now, we have walked through the history of kinetic unmixing and decomposition under various thermodynamic driving forces, namely P_{O_2} gradient, electric field, thermal gradient and stress gradient, with emphasis on the P_{O_2} gradient and electric field. From the literature, one can see that no literature has ever reported kinetic decomposition under electric field. Numerous literature report kinetic unmixing under P_{O_2} gradient and electric field, and there are few reports concerning kinetic decomposition under P_{O_2} gradient. Electric field is the most common driving force one can find nowadays, and kinetic decomposition affects the performance of devices in a more severe manner compared to kinetic unmixing. It is therefore quite amazing to see that no research reports kinetic decomposition (which is consequentially more severe) under electric field (which is the most common driving force). This leads to the main theme of this thesis. In the next Chapter, experiments are performed to (i) confirm whether kinetic unmixing *and* decomposition occur in ternary oxides under electric field and (ii) give other possible reasons for the behavior of $BaTiO_3$, which as previously shown showed neither kinetic unmixing nor decomposition. The results will be confirmed with novel equations in Chapter 4.

3. Experimental results on kinetic unmixing, decomposition and solid state reaction (diffusion couples)

(1) The literature on the ternary system - NiTiO₃

In selecting a model ternary oxide system, a few conditions had to be concerned. The most important criterion was the simplicity in phase diagram. To exclude any possibility of formation of other intermediate compounds, systems with very simple phase diagram, i.e. quasibinary AO_x-BO_y systems with only one intermediate compound (which would be the model system) were chosen. Within those systems, materials with chemical instability, i.e. hygroscopicity, were excluded. Also, if possible, systems with smaller magnitude of Gibbs free energy of formation $|\Delta G_f^\circ|$ were preferred, because it would mean that relatively smaller driving force would be required for kinetic unmixing or decomposition. Combining all these criteria, nickel titanate (NiTiO₃) was selected as the model system.

Nickel titanate has ilmenite structure, which is an ordered derivative of corundum (Al₂O₃) structure. The name ilmenite refers to the mineral FeTiO₃. There are two main structures for ABO₃ ternary oxides - perovskites and ilmenites. A material takes one of the two depending on the Goldschmidt tolerance factor[100] of the system which is given as

$$t = \frac{r_A + r_O}{\sqrt{2}(r_B + r_O)} \quad (3-1)$$

where r_k is the radius of k ion (k=A,B,O). In essence, this ratio shows how "cubic" the structure is. Depending on this ratio the ternary oxide takes its respective crystal structure as shown in Table 3-1.

In case of NiTiO₃, $r_{\text{CN}=6}^{\text{Ni}^{2+}}=0.69 \text{ \AA}$, $r_{\text{CN}=6}^{\text{Ti}^{4+}}=0.605 \text{ \AA}$ and $r_{\text{CN}=6}^{\text{O}^{2-}}=1.4 \text{ \AA}$ (CN: coordination number of each ion)[101], leading to Goldschmidt ratio of 0.74. Ilmenite structure is based on hexagonally close-packed oxygen layers with cations occupying two thirds of the available octahedral interstitial sites and has space group $R\bar{3}$. The cation layers alternate from A-filled layer to B-filled layer, i.e. the layer sequence is A-O-B-O-A... (whereas in LiNbO₃ structure the layer sequence is (A+B)-O-(A+B)-O-(A+B)... The two structures are the representative derivative structures of corundum) as shown in Fig. 3-1 and the cations form a hexagonal ring, as shown in Fig. 3-2. Each cation type has six oxygen ions around it to form AO₆ and BO₆ octahedra, sharing their faces on the (001) plane. Due to the electric repulsion between the cations, the actual structure is distorted with the extent of distortion increased by external pressure, even changing the stacking sequence into that of LiNbO₃ type structure (space group $R\bar{3}c$)[102] or even into GdFeO₃ structure (Pbmn)[103] which is orthorhombic perovskite.

The electrical properties of NiTiO₃ had been researched by Stüber et al.[104] at high temperatures. There is an order-disorder transition near temperature of 1290°C wherein the ordered ilmenite structure turns into a disordered corundum structure (Fig. 3-3). As in ilmenite structure the oxygen ions are close packed in hexagonal configuration and are much larger in size compared to the cations, oxygen defects are negligible, just as in the case of rock salt structure. The majority defects lie on the cation sublattice, along with electronic defects.

Simplicity of phase diagram is essential in treating kinetic unmixing and especially kinetic decomposition. NiTiO₃ is ideal when taking into account kinetic unmixing and decomposition because according to the phase diagram[44,45] the ilmenite NiTiO₃ seems to have a certain range of stability large enough to be not represented as just a line in the phase diagram (48~52 m/o NiO, Fig. 3-4). This will enable observation of kinetic unmixing to relatively large extent for a near-stoichiometric

Goldschmidt tolerance factor (t) [§]	Structure	Example
>1	Hexagonal perovskite	BaNiO ₃
0.9~1	Cubic perovskite	SrTiO ₃ , BaTiO ₃
0.71~0.9	Orthorhombic/rhombohedral perovskite	GdFeO ₃ , CaTiO ₃
<0.71	Corundum, ilmenite, LiNbO ₃ type	FeTiO ₃ , NiTiO ₃ , MgTiO ₃ , LiNbO ₃

§ The given tolerance factor ranges are not absolute values

Table 3-1. Crystal structure of ABO₃ type compound according to Goldschmidt tolerance factor.

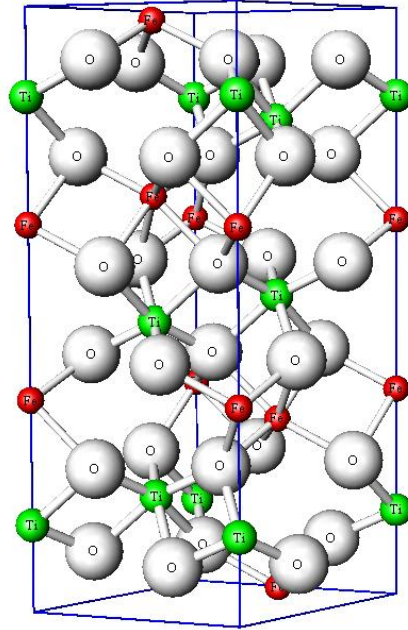


Fig 3-1. The crystal structure of ilmenite FeTiO_3 , showing hexagonally close-packed oxygen anions and alternating cation layers filling $2/3$ of octahedral sites.

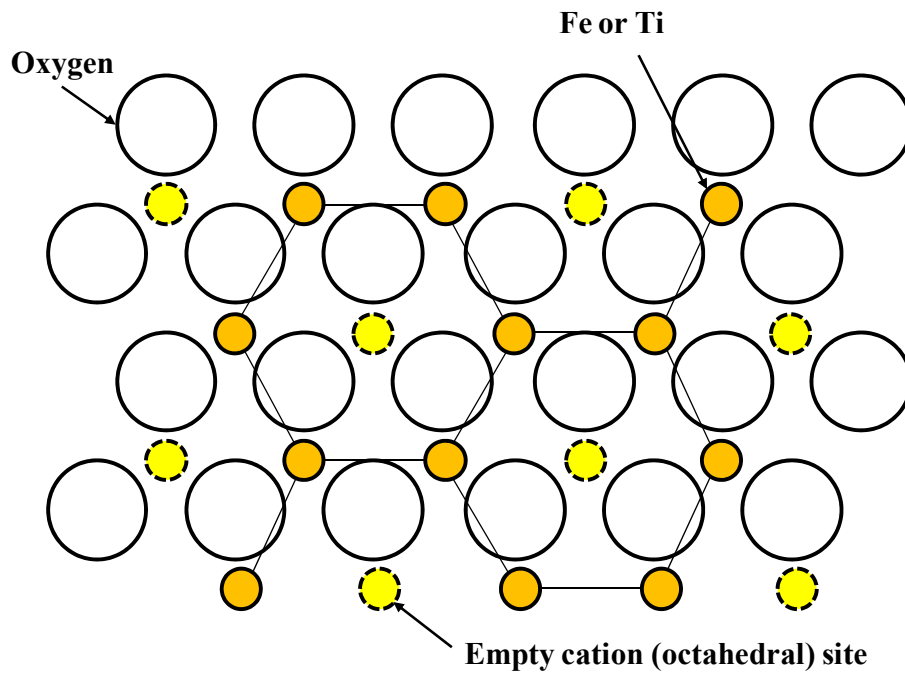


Fig. 3-2. The ilmenite structure as viewed from [0001] direction. The oxygen ions form hexagonally close-packed layer, with cations filling 2/3 of octahedral sites, forming hexagonal rings.

compound (in most cases, intermediate compounds are very stoichiometric, i.e. they exist in a very narrow range of composition). Also, below c.a. 1380°C the only intermediate compound in the NiO-TiO₂ system is NiTiO₃, so when and if kinetic decomposition occurs there will not be any other intermediate compound to further complicate the analysis. A good comparison would be the system of CoO-TiO₂[28], wherein multiple intermediate compounds exist.

The order-disorder transition was first anticipated by Lerch et al.[105] from the anomalous increase in electrical conductivity and temperature dependence of the Seebeck coefficient in the region between 1250°C and 1290°C. The transition enthalpy and entropy was measured and calculated from emf-measurement cell in the configuration Ni,TiO₂,NiTiO₃|ZrO₂(+CaO)|Ni,NiO in the transition region. The values were (18±2) kJ/mol and (12±1) J/mol·K, respectively in air. When this transition occurs with increasing temperature, the crystal structure changes from ilmenite ($R\bar{3}$) to corundum ($R\bar{3}c$), wherein the cations are not ordered anymore, i.e. the cation sites are now mixed.

The main defects as mentioned before lie on the cation sublattice. Below the transition temperature (ilmenite) the defects are Ni vacancies $V_{Ni}^{//}$ and trivalent Ti interstitials Ti_i^{***} , electrons and electron holes, while above the transition temperature (corundum) instead of Ni vacancies, as sites are disordered, cation vacancies are formed, with expected charge of 3+. At air atmosphere the compound is a p-type semiconductor, therefore electron holes are dominant electronic defects.

Another reason NiTiO₃ was selected as a model system is the relatively small values of formation free energy compared to other ABO₃ compounds, especially cubic perovskites. Numerous studies have been done on the free energies concerning the Ni-Ti-O system. Taylor and Schmalzried[106] used galvanic cells with zirconia (doped with either CaO or MgO) as electrolyte to determine the free

energies of formation of various compounds including NiTiO₃ in the temperature range of 800~1200°C. Pejryd[107] used CaO-doped zirconia for the range of 747~1247°C. Lerch and Laqua[108] also used CaO-doped YSZ in the temperature range 777~1377°C. Kale[109] used YSZ in the temperature range 721~1098°C. Jacob et al.[110] used similar galvanic cell to measure the free energies in the temperature range 627~1427°C. Also, it is calculated from the enthalpy and entropy values tabulated in thermodynamic handbook[111]. The compiled results are shown in Fig. 3-5. It can be seen that at the temperature of 1300°C, the free energy of formation is c.a. -7~-9 kJ/mol. It should be emphasized that this free energy of formation is that from its constituent oxides, in the reaction NiO(s, rock salt)+TiO₂(s, rutile)=NiTiO₃(s, ilmenite) and not the free energy of formation from the atoms, i.e. Ni+Ti+3O=NiTiO₃. We are concerned with the former one because according to the phase diagram NiTiO₃ would, if it does, kinetically decompose into NiO and TiO₂.

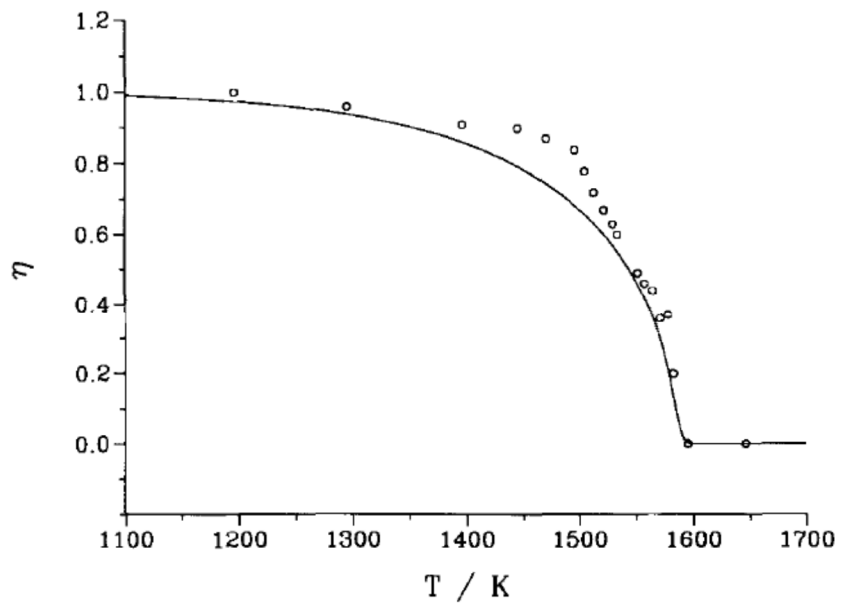


Fig. 3-3. The order parameter η of NiTiO_3 calculated from conductivity data (solid line) and neutron scattering (circles). From Stüber et al. [104]

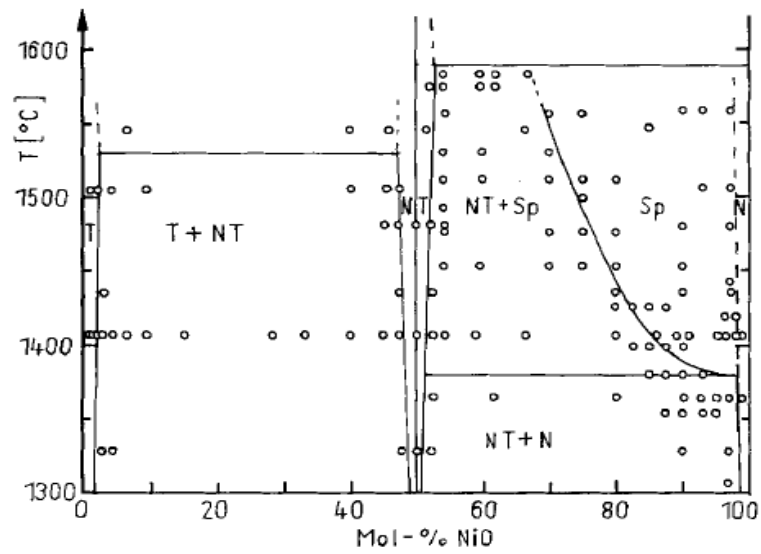


Fig. 3-4. The high temperature phase diagram of NiO-TiO₂ system. NT resembles the ilmenite NiTiO₃. From Laqua et al. [44]

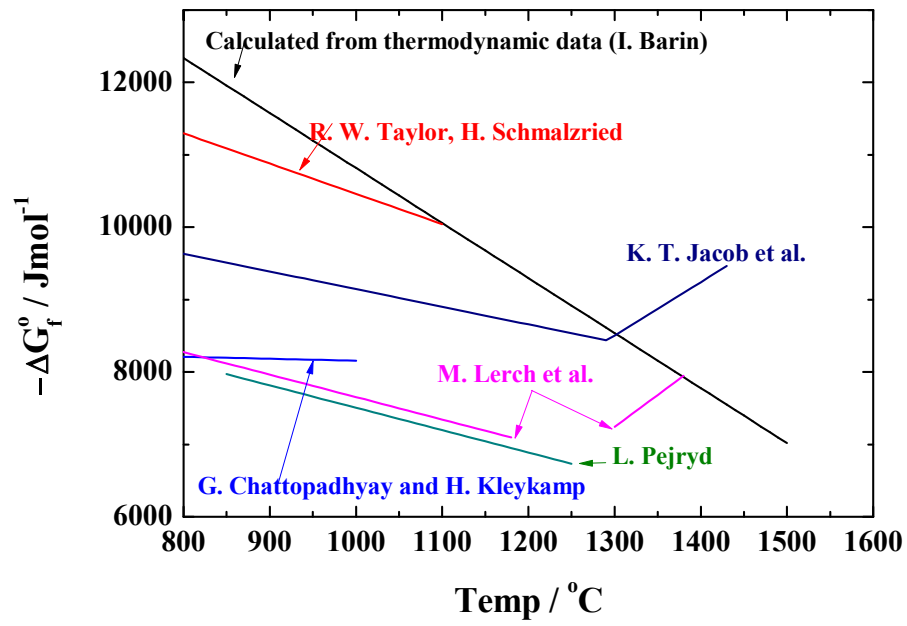


Fig. 3-5. The compiled values of $-\Delta G_f^0$ from literature as function of temperature in NiTiO_3 for the reaction $\text{NiO(s)} + \text{TiO}_2\text{(s)} = \text{NiTiO}_3\text{(s)}$.

(2) The literature on solid state reaction (diffusion couples) and inert markers

In Chapter 2 it was stated that the origin of kinetic unmixing and decomposition is the difference in mobility of the constituent cations. Therefore, one must somehow measure the cation mobilities to quantitatively analyze these phenomena. In this section a method for such purpose is given, in the form of solid state reaction (diffusion couples) while applying inert markers.

When two or more materials are put together at high enough temperatures, the materials react with each other to form novel compounds. For simplicity, let us limit the discussion to two oxides that are put together. This kind of reaction is called solid state reaction, because the materials react in their solid states. This material "couple" is called diffusion couple, as the ions interdiffuse while forming an intermediate compound.

Interdiffusion refers to the cation species diffusing in opposite directions, i.e. the A cations in AO_x migrate toward BO_y and the B cations in BO_y migrate toward AO_x . The driving force for such migration is the concentration gradients, or chemical potential gradients. As it is a pure diffusion process, it is governed solely by Fick's law. There are many different reaction mechanisms that could govern this process, such as those suggested by Schmalzried[112] for oxides: (a) only cations are mobile (oxygen is excluded from phase boundaries); (b) oxygen is provided at both boundaries; (c) only oxygen is available at the boundaries; (d) oxygen and one of the reactants are possible available at the boundaries; (e) one of the reactants is available at one boundary and both oxygen and the other reactant is available at the other boundary. They are shown in Fig. 3-6.

When oxygen is abundant in the ambient atmosphere the A cation meets BO_y and forms an intermediate compound, for example, ABO_{x+y} by the reaction

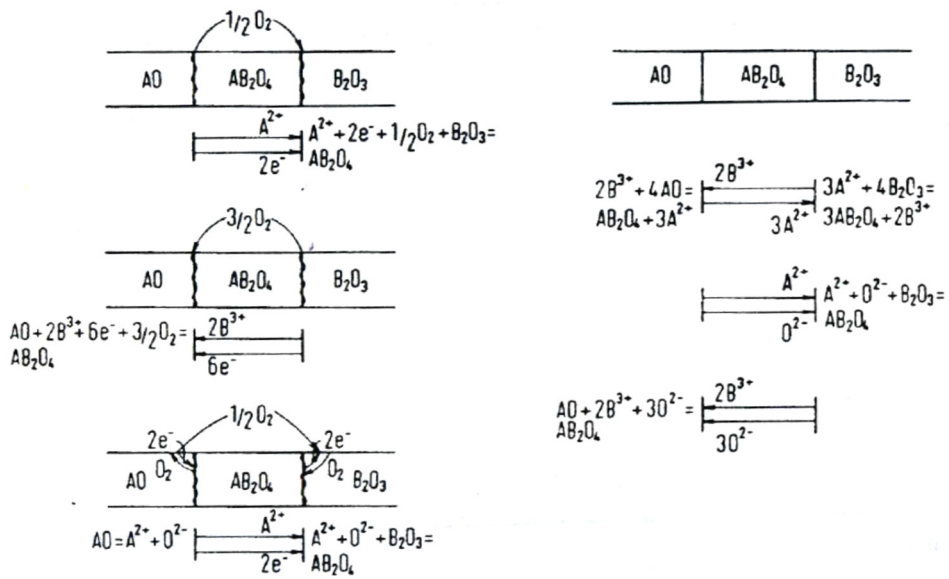


Fig. 3-6. The proposed possible mechanisms of spinel oxide formation. Taken from Schmalzried. [112]



and for the B cation meeting AO_x the reaction would be in the form



If both cations migrate at equal rate in the newly created compound ABO_{x+y} , and assuming that the energy barrier required in forming ABO_{x+y} is very small, then the cations would have equal contribution in the newly-formed layer thickness, i.e. the layer grown by transport of cation A would be equal to that by the transport of cation B. However, this generally is not the case. Because the cations generally migrate through different sublattices as stated in Chapter 2 (unless the starting materials AO_x and BO_y have identical crystal structure and form complete solid solution, i.e. $(Co,Mg)O$), they have different migration activation energy and therefore different mobility. For example, if the A cation is much faster than the B cation, the contribution of B cation would be negligible compared to A cation and ABO_{x+y} would be formed solely by the transport of cation A through the ABO_{x+y} layer and meeting with BO_y to form new ABO_{x+y} , i.e. by eq. (3-1).

As stated in Chapter 2, the origin of kinetic unmixing and decomposition lies in the mobility ratio of the constituent cations. In the previous paragraph, it was stated that the respective thicknesses arising from the transport of A or B cation corresponds to the mobility of the respective cations. However, how can one distinguish which layer corresponds to which? In other words, how can one set the boundary between the layer grown by the transport of A and one grown by the transport of B, respectively? To answer this question, inert markers are introduced.

Before introducing inert markers, there is another method that could directly measure the diffusion coefficient (and therefore the mobility) of the ions. This method is termed secondary ion mass spectrometry (SIMS). SIMS itself is a technique used to analyze the composition of solid surfaces or thin films by sputtering the surface of the specimen with a focused primary ion beam and collecting and analyzing the ejected secondary ions (thus the term secondary). The ejected secondary ions are put through an energy filter (electrostatic analyzer), then are collected in a mass spectrometer. The sputtered depth may range from a few nanometers to micrometer range.

SIMS can be used to measure the diffusion coefficients of ions in the following manner. On the surface to be analyzed, impurity elements or radioactive tracers with long enough lifetime are applied as thin films, usually by chemical vapor deposition (CVD) or pulsed laser deposition (PLD). This specimen-thin film setup is then put under heat treatment at desired temperatures for a duration. During thermal annealing, the thin film source of impurities or tracers diffuse into the specimen, creating a concentration profile, like the one shown in Fig. 3-7 [113]. As this profile is created solely by diffusion, the profile is then fit to a concentration profile equation, usually in the form of error function such as

$$c(x, t) = c_0(t) \exp\left(-\frac{x^2}{4Dt}\right). \quad (3-3)$$

From fitting the diffusion coefficient can be obtained for each annealing condition. Through more complex analysis, the grain bulk and grain boundary diffusion coefficients can also be obtained. Because grain boundaries generally possess characteristics that are different from the grain bulk, these two diffusion coefficients usually differ by orders of magnitude.

Although SIMS is indeed a powerful tool in obtaining the information on diffusion

coefficients, the apparatus required for analysis is very expensive. Also, for some elements there may not be adequate radioactive tracers, as radioactive tracers are generally unstable. Therefore another method is introduced, wherein at least the mobility ratio can be obtained, which is the previously mentioned solid state reaction with inert markers.

Let us first introduce the history of inert markers. Inert markers were first used by A. Smigelskas and E. Kirkendall[114]. They wrapped insoluble thin wires of molybdenum around a Cu-Zn α -brass (Cu:Zn=70:30) and electrodeposited copper around it (Fig. 3-8). After thermal treatment, the molybdenum wires carved into the alloy in a parabolic manner (i.e. the carved-in distance was proportional to the square root of time, as shown in Fig. 3-9). When diffusion took place in α -brass, the zinc diffused much more rapidly than copper, leading to a shrinkage of the α -brass which is highly concentrated with zinc compared to the electroplated copper surrounding it. This was an important result in that, before their work the interchange of solute and solvent atoms during diffusion was assumed to be equal, in which case the molybdenum wires would not have moved. This result suggested unequal interchange of solute and solvent atoms during diffusion. Because the result was at the time inexplicable, it faced severe criticism from the scientific society, such as that from R. F. Mehl. However, Mehl obtained exact same results afterward, thereby confirming Kirkendall's work. Thereafter, this phenomenon was accepted and coined Kirkendall effect.

The explanation for such behavior was first provided by L. S. Darken [115]. The following assumptions should first be made: (i) the molar volume V_m of the assembly should be constant, or V_m is independent of concentration (therefore the lattice site density remains constant during the interdiffusion) and (ii) local equilibrium prevails. Essentially, the sum of fluxes of cations A and B has to vanish for the number of lattice sites to be kept constant. However, one flux is usually larger than the other, since the cations have different mobilities, meaning that the

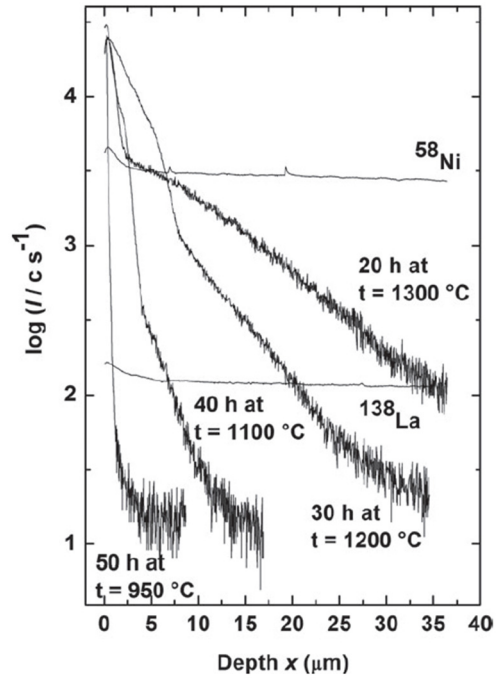


Fig. 3-7. A typical concentration profile according to secondary ion mass spectroscopy. The fluctuating lines represent radioactive Co tracers after various annealing conditions in $\text{La}_2\text{NiO}_{4+\delta}$. From Cebasek et al. [113]

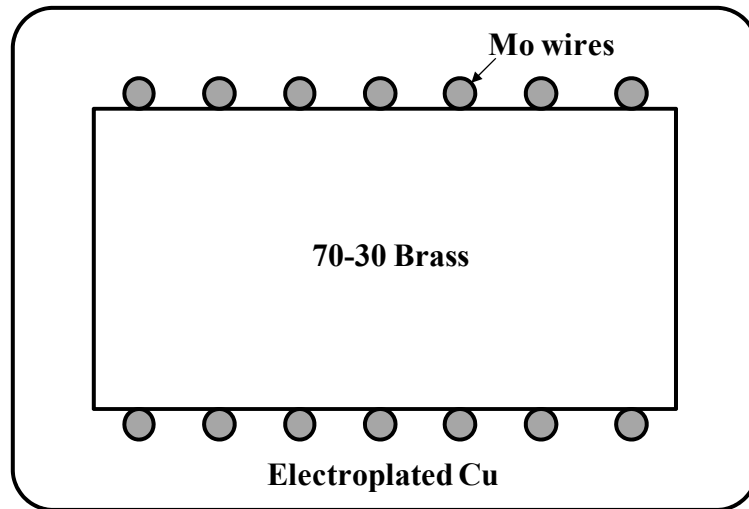


Fig. 3-8. A sketch of a cross section of a bar-shaped specimen from the paper by Smigelskas and Kirkendall. Taken from Nakajima [116].

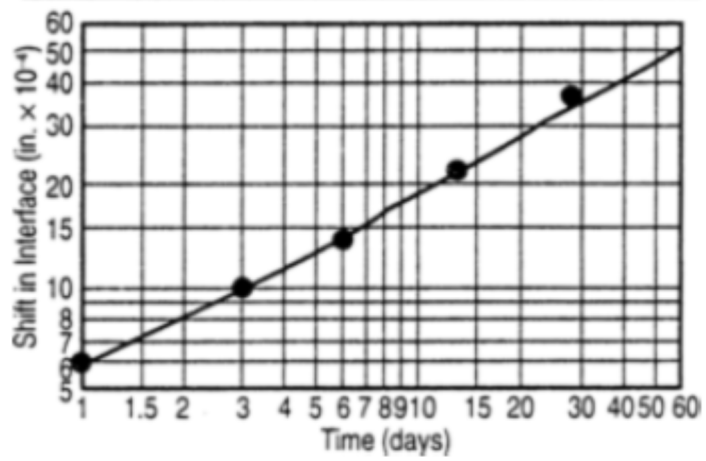


Fig. 3-9. The annealing time dependence of the interface shift (the distance between the molybdenum wires on the opposite surfaces). From Nakajima [116].

total cation flux is non-zero. To compensate for this difference in mobilities but still keep the number of lattice sites constant, local production or annihilation of lattice sites must occur. This can be done by the flux of vacancies in the direction opposite to the faster migrating species, which counterbalance the total cation flux, i.e. $J_V = -(J_A + J_B)$. From an external observer's view, the markers move in the direction of vacancy flux. If cation A is faster than B, the markers would be situated near A and vice versa. It should be noted that Kirkendall effect occurs not only for vacancy mechanism but also for interstitialcy mechanism, but not for interstitial mechanism, as diffusion by vacancy and interstitialcy mechanisms require the presence of point defects for the atom to move while interstitials move by distorting the host crystal[117].

In the work by Smigelskas and Kirkendall they used as *insoluble* markers molybdenum. From the term *insoluble* or *inert* one can see that these markers do not chemically react with the surrounding matrix. As they must be chemically inert even at high temperatures they are generally made of rare metals such as molybdenum[114,118], platinum[73,119-128], gold[129,130] or tungsten[131-134].

Originally the markers were applied as wires around a specimen or embedded in a matrix for the lack of better methods. However, due to the comparatively large sizes of wires, reaction layers much thicker than the wires were required for analysis. Instead, films were deposited so as to uniformly cover the entire surface. This method however denied ionic transport when the films were coated too thick, acting as blocking layer for diffusion. A better method was found by thermally annealing the coated films so that they break up into small islands, therefore only partially covering the surface but being small enough in size not to hinder transport. This can also be done by painting the surface with inert paints or pastes, such as platinum pastes, then annealing. The various elements and forms applied as inert markers are summarized in Table 3-2.

From Darken's analysis of Kirkendall effect, one can see that the inert markers, after thermal annealing, represent the original interface in which the diffusion couple was set up in. This was the information that was required for obtaining the mobility ratios of the constituent cations in ABO_{x+y} . In other words, the boundary between the layer grown by the transport of A and B is set by the position of the inert markers. Therefore one can obtain the cation mobility ratio by measuring the distance from AO_x/ABO_{x+y} boundary to the inert markers and from the inert markers to the ABO_{x+y}/BO_y boundary. The justification of this will be treated in Chapter 4.

Inert marker element	Form	Reference
Mo	wire	[114], [118]
Pt	wire	[119], [123]
	film	[120], [122] [124], [125]
	particle	[73], [121], [126] [127], [128]
Au	particle	[129]
	wire	[130]
W	film	[131], [133], [134]

Table 3-2. Various inert marker elements and forms.

(3) Specimen preparation and experimental results

(a) Specimen preparation

NiTiO₃ specimens for the unmixing and decomposition experiment were prepared by solid state reaction method, mixing stoichiometric ratio of starting powders NiO (Seimi Chemical, Japan) and TiO₂ (Sigma Aldrich, USA). The powders were weighed, then were put under planetary milling in a zirconia jar with zirconia balls overnight with absolute ethanol as solvent. After milling, the solvent was dried and the powder was calcined at 1100°C, followed by sintering at 1400°C for 5 hours in air. The sintered pellets had relative density of c.a. 98% and had mean grain size of (18±4) μm. They were found to be of single phase NiTiO₃ with no detectable secondary phases by x-ray diffractometry.

The sintered pellets were then cut into near-square plates with dimensions of (4.2~4.6) × (4.2~4.6) × (1.0~1.2) mm³. The opposite near-square faces were polished using diamond pastes to the range of 1 μm fineness. For electrodes, platinum gauze (100 mesh, Sigma Aldrich, USA) was used. This is because the specimen surface at the electrodes should be open to oxygen exchange but blocking with respect to cation exchange. If the surface is completely shut, oxygen would not be able to penetrate to the surface to meet the oncoming cation (at the (-) electrode side) or the oxygen evolved from the electrode may be trapped at the electrode/specimen interface (at the (+) electrode side), both acting negatively in analyzing the results. The size of platinum mesh was 5 × 5 mm², slightly bigger than the specimen surface. The platinum mesh was attached to the specimen with the aid of lightly-painted platinum paste (HLG6926, Engelhard, USA) and subsequently heat-treated at 1000°C overnight under light spring pressure to secure firm electrical contact between the electrode and the specimen. The cells assembled as described above were held at a constant temperature of 1300°C in air. The driving force was applied galvanostatically in the range of 10<I/mA<550 using current source (Keithley 228A, Keithley, USA; Agilent 6010A, Agilent, USA; Keithley 2400, Keithley, USA) and the voltage values were measured by digital

multimeters (Keithley 2000, Keithley 2000, USA). The time duration of each run was selected so that the total charge flown was approximately constant for all runs at about 5200 C.

For the experiment of NiTiO₃ formation, its component oxides NiO and TiO₂ were prepared by sintering the same starting powders NiO and TiO₂ as above at 1400°C for 3 hours and 1450°C for 6 hours, respectively, both in air. The sintered pellets of both oxides were ca. 98% dense with mean grain sizes of (8±2) and (14±2) μm, respectively. Both component oxide pellets were subsequently cut into thin square plates, measuring ca. 4.5×4.5×0.6 mm³ and polished on the square faces down to a 1 μm fineness. The reaction couples NiO/TiO₂ were formed by keeping the two component plates in intimate contact between the two alumina rods with a light spring pressure applied. As the inert markers are used to locate the original interface afterwards, the platinum paste was put on lightly onto either of the polished faces in contact. The presence of such inert markers may affect the reaction kinetics because Pt particles are cation-blocking in any case. We have, thus, prepared some blank couples without the inert markers to check this possibility afterwards. The results will be shown later. Formation reaction experiments were carried out by keeping the reaction couples, sometimes together with the blank couples, at a fixed temperature of 1300°C in air for different time durations. Schematic cell diagrams are shown in Fig. 3-10. The specimen images are shown in Fig. 3-11.

The spring loading is done by putting the specimen-electrode setup between two alumina rods which are loaded by spring on one side. Although the specimen and the alumina rods are separated by platinum mesh, slight reaction between the Ni and alumina occurred, resulting in a bluish hue on the alumina rods, which is the spinel NiAl₂O₄. To prevent this reaction, platinum foils (0.05 mm thickness, Sigma Aldrich, USA) with the same size as platinum mesh were inserted between the

electrode and alumina rods on both sides. The lead wires were connected to these foils by welding.

After each electrotransport run or formation experiment, the unmixing /decomposition cell or diffusion couple was immediately taken out of the furnace into room temperature. Although thermal shock is a worrisome phenomenon, no visible thermal cracks occurred in the specimens. The reason for such a quenching instead of slowly lowering the cell temperature is that additional matter flow can occur at such slow ramp. The cation concentration profile that has been fixed at 1300°C by electric field and subsequent diffusion flux will be disrupted when the electric field is turned off, resulting in pure diffusion flux which will decrease the formed concentration gradient. The specimen was cut into two halves in the direction of the current. The dissected surfaces were then subsequently polished to 1 μm fineness. After polishing the surfaces were examined by x-ray diffractometry (M18XHF-SRA, MAC Science Co. Japan; New D8 Advance, Bruker AXS, Germany) and scanning electron microscopy (JSM-5600 and JSM-6360, JEOL, Japan). The compositional scans were done using an electron probe microanalyzer (JXA-8900R, JEOL, Japan).

As the unmixing experiment is to be carried out galvanostatically in a two-probe d.c. setup, it is necessary later on to convert the constant current I passed into the voltage U applied across the specimen itself, free from the electrode overpotentials. The total conductivity of NiTiO_3 was measured by the four-probe d.c. method on a parallelepiped specimen cut out of the as-sintered NiTiO_3 pellet, measuring $(3.42 \pm 0.02) \times (3.163 \pm 0.008) \times (6.289 \pm 0.007)$ mm^3 with the inner potential-probes (3.56 ± 0.16) mm apart, at the identical thermodynamic condition of the unmixing experiments, 1300°C and air atmosphere. In order to see the effect of unmixing and decomposition on the total conductivity, measurements were made on the same specimen from being fully equilibrated through being only unmixed till being decomposed at both ends by less than 5 % by volume.

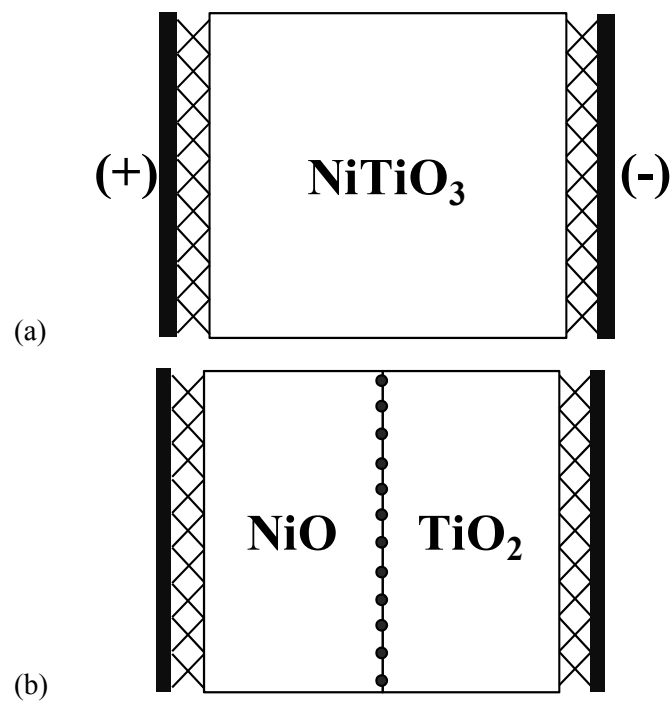
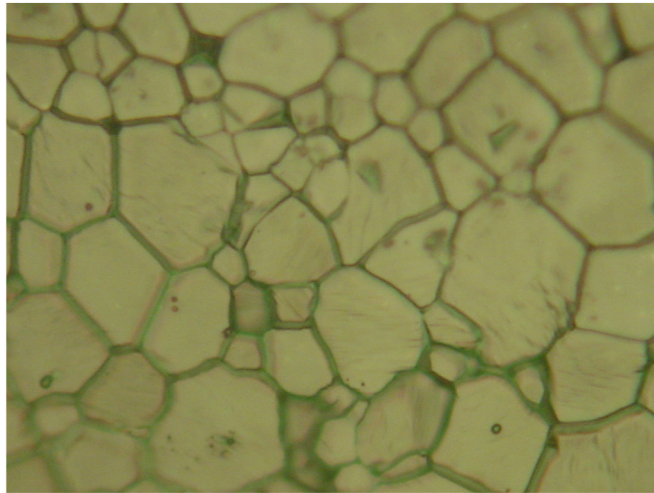
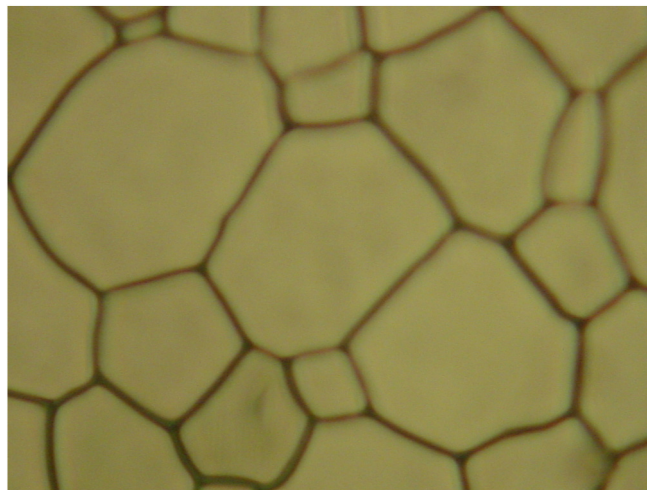


Fig 3-10. Schematics of the as-constructed (a) unmixing cell involving NiTiO_3 and the (b) as-constructed reaction couple $\text{NiO}|\text{TiO}_2$ for NiTiO_3 formation. $\times\times\times\times$: platinum gauze; $\bullet\bullet\bullet\bullet$: inert platinum markers; \blacksquare : platinum foil.

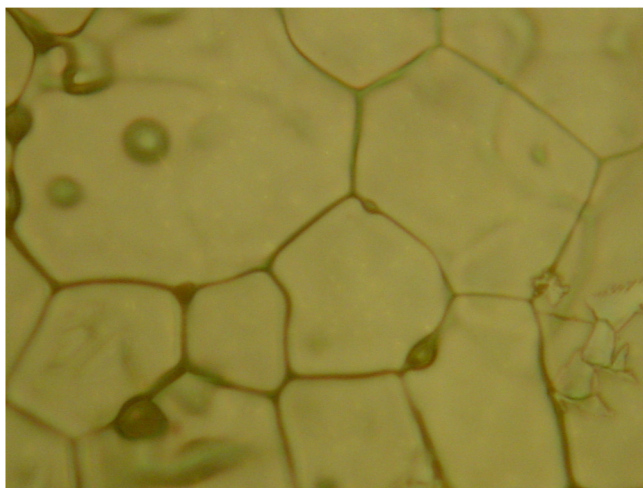


(a) **0.05mm**



(b) **0.05mm**

Fig. 3-11. Optical images of (a) NiO, (b) TiO₂ and (c) NiTiO₃ after thermal etching (continued in the next page).



(c) **0.05mm**

(continued) Fig. 3-11. Optical images of (a) NiO, (b) TiO₂ and (c) NiTiO₃ after thermal etching.

(b) The total conductivity of NiTiO₃

NiTiO₃ is a semiconductor and p-type conduction is dominant at 1300°C in air. The total conductivity was measured as $\sigma=0.130\pm0.006$ S/cm (Fig. 3-12) at 1300°C. Compared to the literature value[104], it is about half. This is probably due to the difference in grain size, although the grain sizes were not mentioned in the literature for comparison. After measuring the equilibrium conductivity, a constant current of 20 mA was applied to the specimen. This magnitude of current is high enough to cause even decomposition (as will be shown later). The inner potential drop was monitored during this unmixing and decomposition process for 5 hours. The potential varies only within 0.05 %, as shown in Fig 3-13. Only the effect of kinetic unmixing, if there is any, would be detectable by the inner probes as decomposition would occur only at the outer electrodes where the lattice is actually annihilated or formed. Also, after quenching the specimen the volume percentage of the decomposed regions was measured. It was found to be very small (less than 5% for specimen 1 in Table 3-3 (shown later) which was exposed to very large driving force. The volume percentage of other specimens was less than 2%). Since the volume percentage of the decomposed phases is very small, the overall conductivity can be assumed to the conductivity of NiTiO₃, which even with unmixing is practically constant. Therefore the total conductivity can be assumed to be practically constant as $\sigma=0.130\pm0.006$ S/cm at 1300°C. This constant total conductivity is used to convert the applied current into applied voltage which, as will be shown in Chapter 4, sets the criterion for decomposition rather than the applied current.

(c) Kinetic unmixing and decomposition in NiTiO₃

A total of seven electrotransport runs were made for the system NiTiO₃. To first state the conclusion, five of them (specimen 1~5) showed both kinetic unmixing and decomposition while specimens 6 and 7 showed only kinetic unmixing. Let us first begin with the latter case.

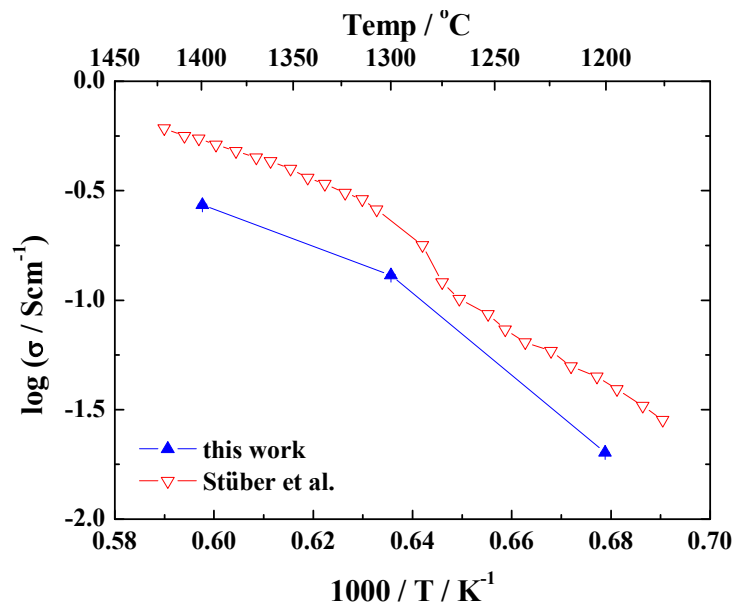


Fig. 3-12. The Arrhenius plot of the total conductivity of NiTiO₃ in air, compared with the literature values reported by Stüber et al. [104]

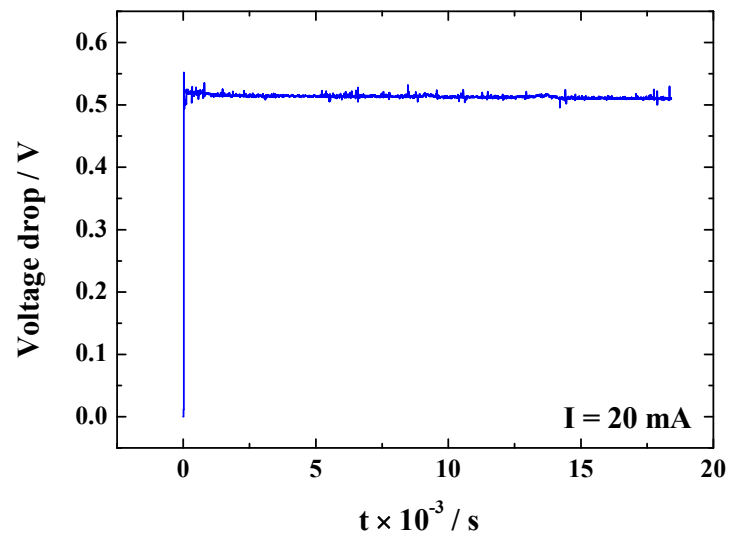


Fig. 3-13. Temporal variation of the voltage drop between the potential probes, 3.56 mm apart, of the ca. 6.289 mm long, 4-probe specimen $\text{NiTi}_{1+\xi}\text{O}_{3+\delta}$ while passing a constant current 20 mA at 1300°C in air atmosphere which has eventually caused a compositional unmixing $\Delta\xi\approx 0.171$ (shown later). Note that the voltage drop remains unchanged within 0.05 % for ca. 5 hrs.

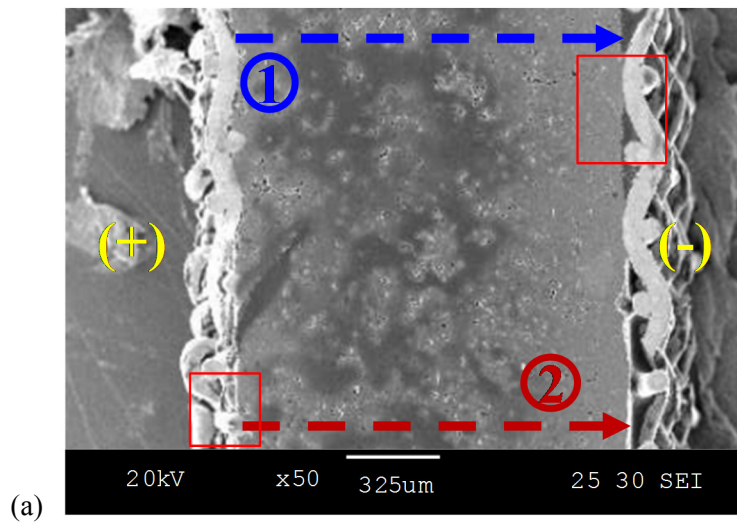
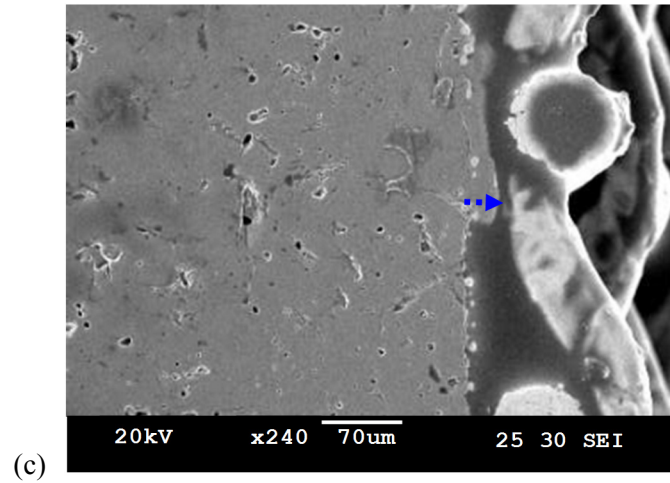
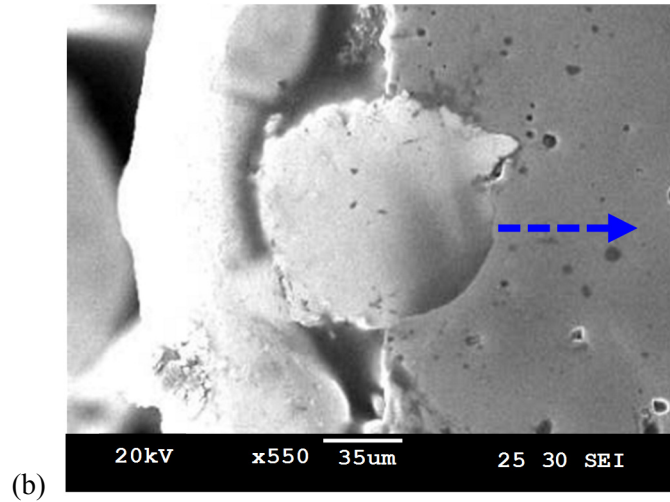
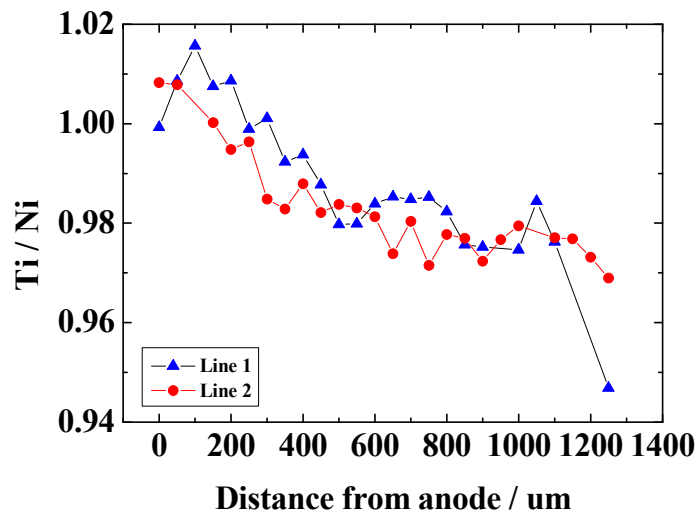


Fig. 3-14. The scanning electron microscopy images of the (a) overall specimen, (b) the anode and (c) the cathode, for specimen 6 which was put under $I=24.1$ mA for 60 hours at 1300°C . The exploded views of the boxed regions are shown in (b) and (c). The dotted arrows indicate the path in which the electron probe microanalysis was done. (continued in the next page)

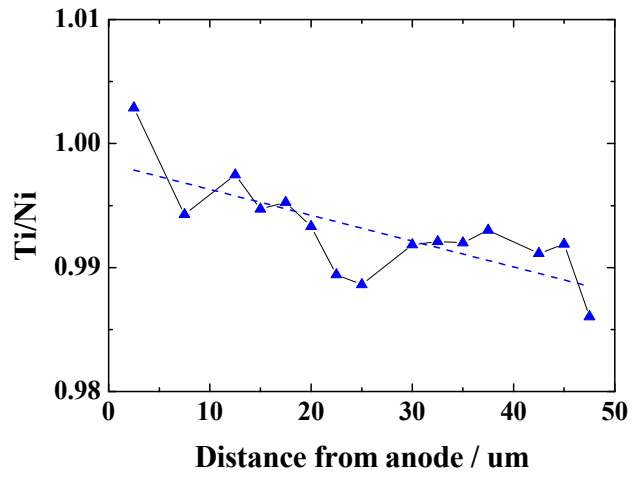


(continued) Fig. 3-14. The scanning electron microscopy images of the (a) overall specimen, (b) the anode and (c) the cathode, for specimen 6 which was put under $I=24.1$ mA for 60 hours at 1300°C . The exploded views of the boxed regions are shown in (b) and (c). The dotted arrows indicate the path in which the electron probe microanalysis was done.

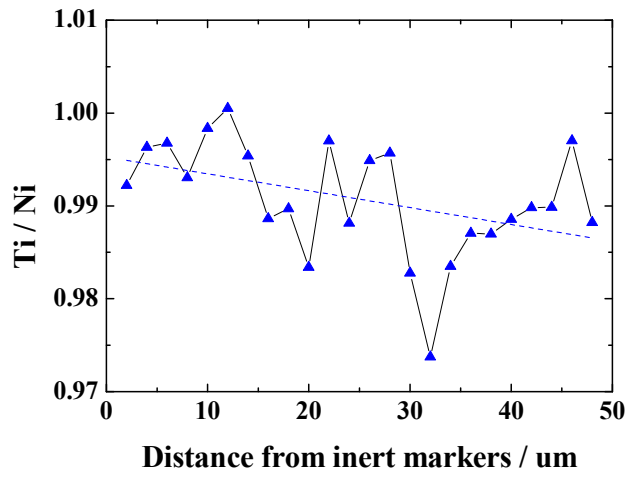


(a)

Fig. 3-15. The electron probe microanalysis (EPMA) scan results of the (a) overall specimen, (b) the anode and (c) the cathode, for specimen 6 which was put under $I=24.1$ mA for 60 hours at 1300°C . The scan paths correspond to the dotted arrows in Fig 3-14. (continued in the next page)



(b)



(c)

(continued) Fig. 3-15. The electron probe microanalysis (EPMA) scan results of the (a) overall specimen, (b) the anode and (c) the cathode, for specimen 6 which was put under $I=24.1$ mA for 60 hours at 1300°C . The scan paths correspond to the dotted arrows in Fig 3-14.

A typical microstructure that occurs with electrotransport is shown in Fig. 3-14. Fig. 3-14 shows the overall microstructure (a) of the specimen from anode to cathode, (b) anode vicinity and (c) cathode vicinity after passing $I=24.1\pm 0.04$ mA for 60 hrs. The detailed microstructure in the anode vicinity is first taken into account. It is first noted that platinum wire segments of the anode platinum mesh have penetrated into the specimen matrix, as can be clearly seen in Fig. 3-14 (b). This is due to the lattice annihilation that occurs at the electrode-specimen interface. This is a typical feature of the electrotransport-induced microstructure change in the anode vicinity, which is due to the concentrated field lines at the anode mesh surface in contact with the matrix and the continuity constraint. Although the extent of penetration of platinum mesh is similar for all platinum mesh in contact with the specimen, some electrodes penetrated in deeper than others, which is probably due to the local concentrations of grain boundaries and other structural defects. The specimens used in the experiment are polycrystalline, so local fluctuation in properties is possible.

In the cathode vicinity one can first see a line of platinum paste particles (Fig. 3-14 (c)), which were used to put the platinum mesh in good contact with the specimen surface. These particles also act as inert markers, or *Darken's chips*, and show the original surface of the specimen. Before the electrotransport run the platinum particles were lined up in the direction parallel to the platinum mesh and in contact with the platinum mesh. However, after electrotransport a new matrix is formed between them. As is the platinum mesh penetrating into the specimen at the anode side, this is another indication that mass transport occurred by the applied current and is another characteristic electrotransport-induced microstructure change. The same features were also observed in the work by Yoo et al. for BaTiO_3 [26], as stated in Chapter 2 (Fig. 2-21).

While the microstructure changes are similar in both NiTiO_3 and BaTiO_3 , the concentration profiles differ greatly. Looking at the EPMA profile across the whole

specimen, one can see in Fig. 3-15 (a) that unmixing occurred without a doubt. The extent of unmixing is about 0.95~1.02 in terms of the ratio Ti/Ni. The EPMA scan at the electrode vicinities were done for three different spots, all yielding similar results. Only one each as representatives are shown in Figs. 3-15 (b) and 3-15 (c). At the electrode vicinities, the scanned profiles show very slight concentration gradient. If decomposition occurred, then there would be concentration jumps which would be noticeable because according to the phase diagram the only compounds that can exist are NiO, TiO₂ and NiTiO₃. Even if NiO and TiO₂ have some mutual solubilities, they would not be very big as they have different crystal structure and from the phase diagram their solubility is less than 5%. No such concentration jump occurred, therefore it is safe to say that decomposition did not occur. This is quite different from BaTiO₃, as no unmixing was detected in that case regardless of the magnitude of the driving force.

Specimens 1~5 were applied to higher current. Fig. 3-16 shows the SEM images for specimen 1 which was exposed to the highest current at 546 mA for 160 minutes. From the SEM images of the electrodes one can see that the extent of microstructure change is much greater than that for specimen 6. The anode penetrated into the specimen deeper so that the platinum mesh is completely inside the matrix, leaving behind a linear void as its trail. Also, near the Pt mesh one can observe regions that are darker in color. In SEM image, darker region generally corresponds to lighter elements or regions with lower density. At the cathode side, novel lattice again grew not only in between the platinum mesh and the inert markers but around the platinum mesh as well. This means that a larger extent of matter transport due to electrotransport occurred.

One may wonder why the anode platinum mesh penetrates completely into the matrix. The cell is spring-loaded, meaning that when the mesh would not have any driving force to penetrate into the lattice once it is completely submerged in the lattice. Due to the electrode reactions, the lattice around it would be annihilated,

but this itself does not provide any driving force so that it could penetrate in deeper. A possible reason for such penetration is the larger surface energy. As the platinum mesh leaves behind a void trail, new surfaces open up, meaning that surface energy increases. To decrease the surface energy the matrix tries to clam up behind the mesh and this seems to be the driving force for the penetration. This can be justified by Fig. 3-16 (b), where one can see that the trail left behind by the platinum mesh is narrower than the diameter of the mesh.

The EPMA scan profiles for the overall specimen also shows a larger extent of kinetic unmixing, as shown in Fig. 3-17. The concentration profiles at the electrode vicinities are critical, as they show concentration jumps which signify decomposition. At the anode the ratio Ti/Ni jumps to c.a. 500, which would refer to TiO₂ with very small Ni solubility (~0.8 mol% NiO in TiO₂). At the cathode, the ratio drops to c.a. 0.1. This indicates that Ti can be incorporated into NiO up to 12.8 mol%, which is much larger than that expected from the phase diagram. However, this high solubility seems to be true, as this high solubility was also shown by Schmalzried and Laqua[43] for the Po₂ case and their experimental results coincide with the ones in this thesis.

Although kinetic unmixing was confirmed by EPMA profiles and the EPMA profiles jumped at the electrode vicinities, implying kinetic decomposition, it would be imperative to show by x-ray diffractometry the existence of NiO and TiO₂ to confirm kinetic decomposition. The XRD results confirm (Fig. 3-18) that a small amount of TiO₂ and NiO exist at the anode and cathode vicinities, respectively. Therefore for specimen 1 one can conclusively state that kinetic unmixing and decomposition occurred. Similar results were found for specimen 2~5.

The compiled results for specimens 1~7 are shown in Table 3-3. The applied voltage U_{appl} is calculated from the applied current I_{appl} by multiplying I_{appl} with the

specimen resistance R. Specimens 1 to 5 showed both kinetic unmixing and decomposition, while specimens 6 and 7 showed only kinetic unmixing. This result indicates that the critical decomposition voltage U_d lies somewhere in between 97 and 120 mV. If we take the Gibbs theorem and calculate the decomposition voltage according to $\Delta G_f^o = -nFU_d$, with $\Delta G_f^o = -8,502$ J/mol [110] and $n=2$ (Ni-dominant case), the decomposition voltage is 44 mV. If n is taken to be four (Ti-dominant case), which for the current case does not make sense since it was shown that Ni is faster than Ti (so that the material cannot be a Ti transport-dominant one), it becomes 22 mV. From Table 3-3, it can be easily seen that the results from Gibbs theorem does not fit and that another standard should be employed. This will be confirmed in the upcoming sections.

Specimens 1~5 all showed decomposition. Since kinetic unmixing is required for decomposition to occur, for the decomposed specimens the extent of unmixing would be at maximum at the phase boundaries NiO/NiTiO₃ and NiTiO₃/TiO₂ as the specimen cannot unmix beyond the phase boundaries. Specimens 1~5 all showed similar unmixing profiles like the one shown in Fig. 3-17 (a) for specimen 1. Another example is in Fig. 3-19 for specimen 2. The average compositions in terms of the mole fraction of TiO₂ (x_B) for specimens 1~5 at the NiO/NiTiO₃ boundary (cathode side, x_B^R) and the NiTiO₃/TiO₂ boundary (anode side, x_B^L) are given as

$$x_B^R = 0.482 \pm 0.006, \quad (3-4)$$

$$x_B^L = 0.524 \pm 0.006. \quad (3-5)$$

It should be noted that both x_B^R and x_B^L may be underestimated. This is because the EPMA was done at the point closest to the boundary as possible, but it is not exactly at the boundary. Therefore x_B^R may be smaller than 0.482 and x_B^L larger than 0.524. The phase stability range $\Delta x_B^{\max} = x_B^L - x_B^R$ therefore would be larger

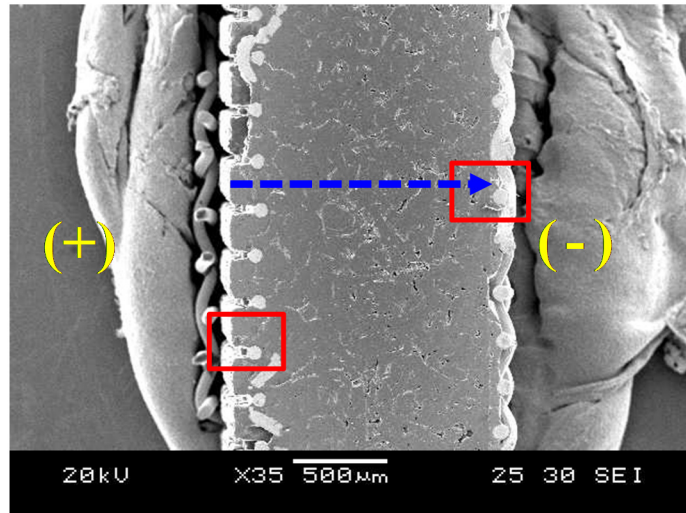
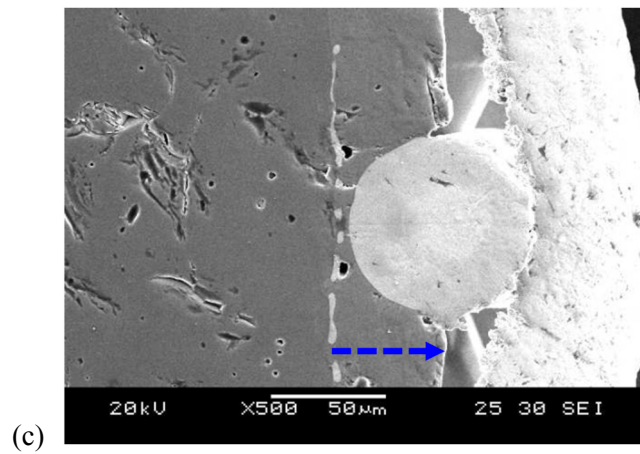
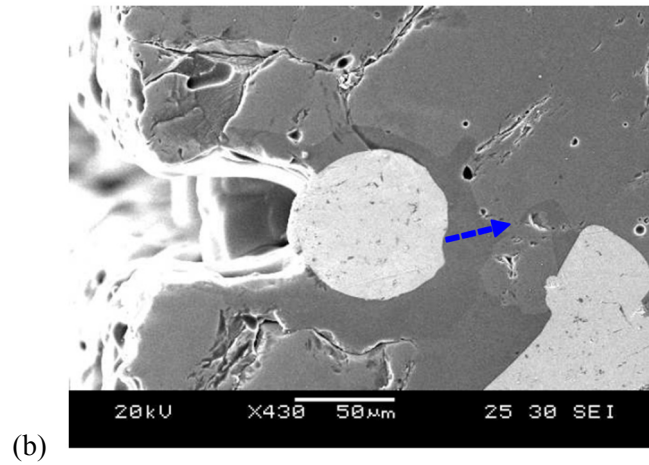
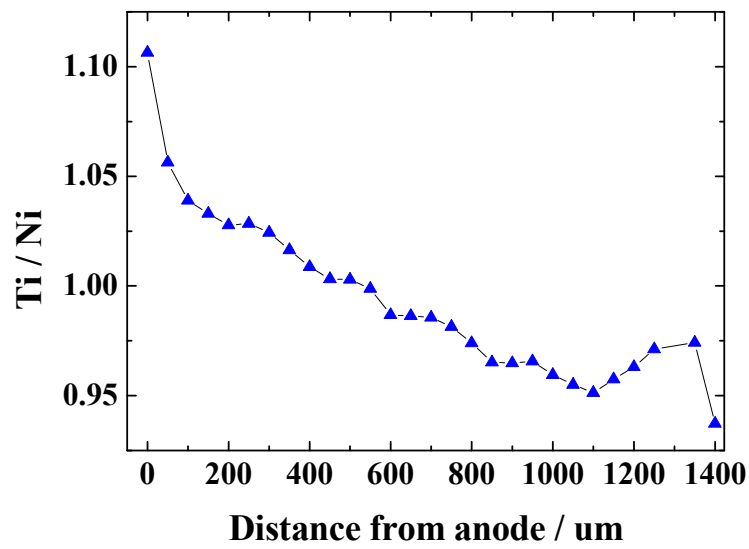


Fig 3-16. The scanning electron microscopy images of the (a) overall specimen, (b) the anode and (c) the cathode, for specimen 1 which was put under $I=546$ mA for 160 minutes at 1300°C . The exploded views of the boxed regions are shown in (b) and (c). The dotted arrows indicate the path in which the electron probe microanalysis was done. (continued in the next page)

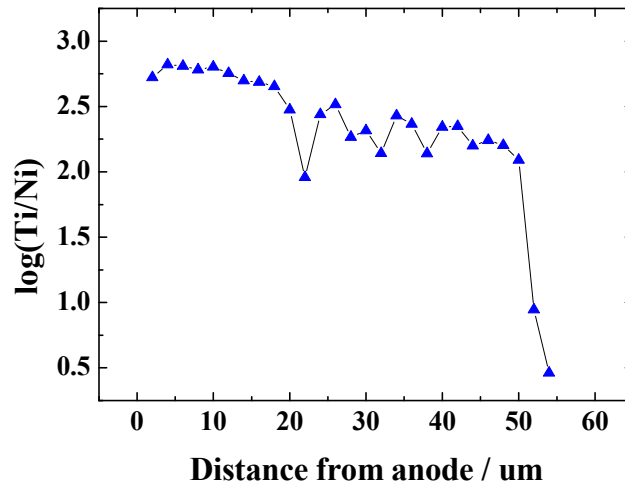


(continued) Fig 3-16. The scanning electron microscopy images of the (a) overall specimen, (b) the anode and (c) the cathode, for specimen 1 which was put under $I=546$ mA for 160 minutes at 1300°C . The exploded views of the boxed regions are shown in (b) and (c). The dotted arrows indicate the path in which the electron probe microanalysis was done.

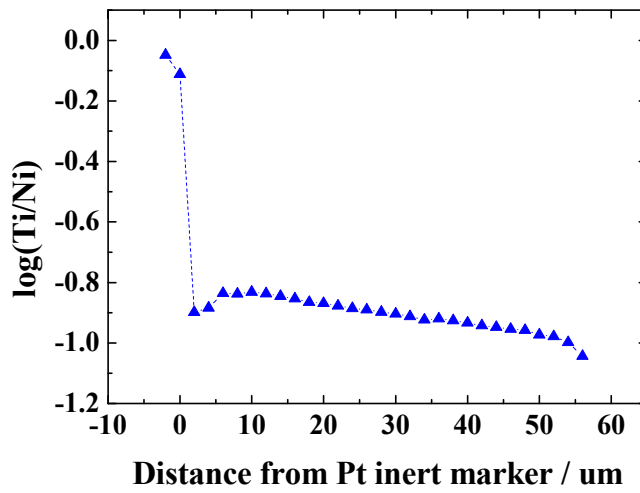


(a)

Fig. 3-17. The electron probe microanalysis (EPMA) scan results of the (a) overall specimen, (b) the anode and (c) the cathode, for specimen 1 which was put under $I=546$ mA for 160 minutes at 1300°C . The scan paths correspond to the dotted arrows in Fig. 3-16. (continued in the next page)



(b)



(c)

(continued) Fig. 3-17. The electron probe microanalysis (EPMA) scan results of the (a) overall specimen, (b) the anode and (c) the cathode, for specimen 1 which was put under $I=546$ mA for 160 minutes at 1300°C . The scan paths correspond to the dotted arrows in Fig. 3-16.

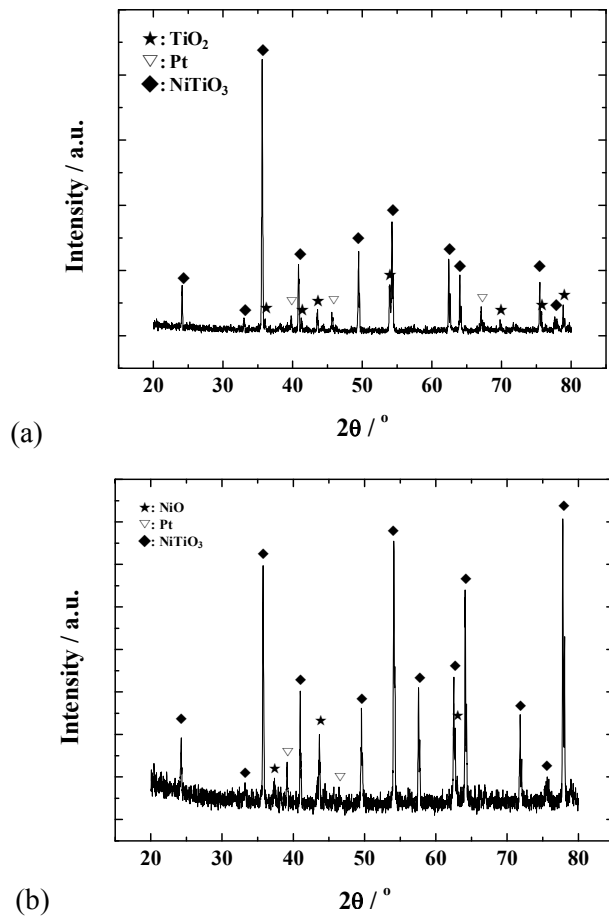


Fig. 3-18. X-ray diffraction patterns taken from (a) the anode vicinity and (b) the cathode vicinity of the electrotransported NiTiO₃ in Fig 3-16. Note that in addition to the peaks for the mother matrix NiTiO₃, only TiO₂ peaks are seen in the anode vicinity and only NiO peaks in the cathode vicinity.

Cell	$I_{\text{appl}} / \text{mA}$	$U_{\text{appl}} / \text{mV}$	Phenomenon observed	
			Unmixing	Decomposition
1	546 ± 6	2200 ± 200	O	O
2	76.4 ± 0.7	300 ± 18	O	O
3	51.0 ± 0.6	200 ± 12	O	O
4	35.5 ± 0.5	143 ± 9	O	O
5	25.9 ± 0.4	120 ± 7	O	O
6	24.1 ± 0.4	97 ± 6	O	X
7	11.9 ± 0.2	48 ± 3	O	X

Table 3-3. Summary of the unmixing/decomposition experiments on NiTiO₃ at 1300°C. Specimens 1~5 exhibited both kinetic unmixing and decomposition while specimens 6 and 7 showed only kinetic unmixing.

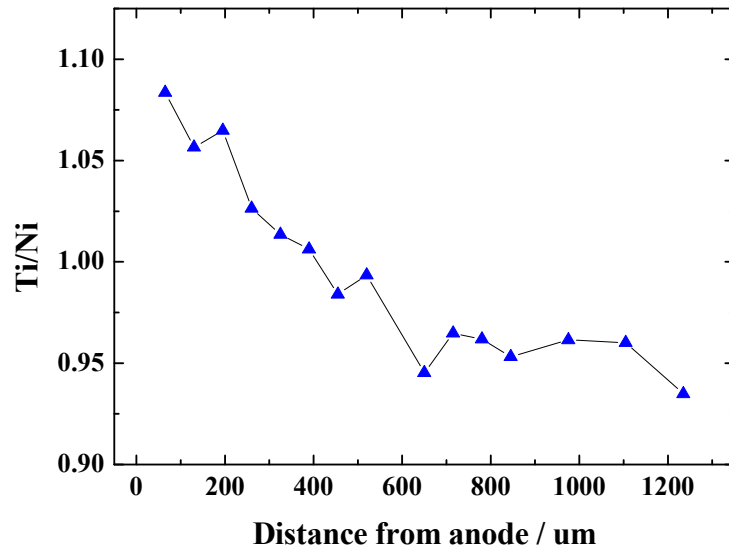


Fig. 3-19. The EPMA profile for the whole specimen in specimen 2. Like Fig. 3-17 (a), kinetic unmixing is visible and the extent of unmixing is also similar.

than 0.042. Compared to the phase diagram (Fig. 3-4) which shows the phase stability regime to be approximately $0.491 \leq x_B \leq 0.510$ at 1300°C, the phase stability regime is about twice larger than depicted in the phase diagram. The reason for such difference is not yet known, but it should be noted that the phase diagram in the literature is not as accurate, since it fails to predict the high solubility of Ti in NiO as well.

(d) Solid state reaction of NiO-TiO₂ and inert markers

A typical microstructure of the NiO-TiO₂ after each solid state reaction run is shown in Fig 3-20. In Fig. 3-20 two cells, one with platinum inert markers and the other without markers, are compared to check the influence of inert markers on the growth kinetics, to ensure that the markers do not affect the growth by i.e. blocking. Both cells were put at 1300°C for 120 hours. The NiTiO₃ layer thickness can be measured from the SEM images and are found to be (155±7) μm and (149±6) μm. Since the two thicknesses are equal within experimental errors, one can conclude that the platinum inert markers applied in the form of platinum pastes do not disturb the formation reaction kinetics and therefore can be safely applied. After formation experiments, NiO tended to fall off the diffusion couple spontaneously. Examination of the interface on the NiO pellet that would have been in contact with NiTiO₃ showed no remnants of NiTiO₃. In other words, all the formed NiTiO₃ existed attached to the TiO₂ pellet. This may be due to the fact that excessive amount of Ni was transported from NiO to NiTiO₃, thus making the bonding at the interface irregular and unstable.

The total layer thickness ($\Delta x = \Delta x_A + \Delta x_B$) and the partial layer thickness ratio $\Delta x_B / \Delta x_A$ are shown in Fig 3-21 according to reaction time. Here, Δx_A refers to the distance from the inert markers to the TiO₂/NiTiO₃ interface, which corresponds to the NiTiO₃ that was formed by the transport of Ni. Analogously Δx_B corresponds to the distance between the inert markers to the NiO/NiTiO₃

interface. From Fig. 3-21 (a), one can see that the layer grew in parabolic manner and can be fit to

$$(\Delta x)^2 = 2k_p t, \quad (3-6)$$

where k_p is the parabolic rate constant or Tamman constant. By fitting the data to eq. (3-6) the Tamman constant is found to be

$$k_p = (2.81 \pm 0.11) \times 10^{-10} \text{ cm}^2/\text{s}. \quad (3-7)$$

The physical significance of the Tamman constant will be given in Chapter 4. The inert markers were found to be aligned in the NiTiO_3 layer, closer to the $\text{NiO}/\text{NiTiO}_3$ interface. This indicates that Ni is faster than Ti, as explained in Chapter 3 in the explanation of Kirkendall effect. Ideally, the markers would be perfectly lined and the maximum error of their placement would be about 1 μm , which is the roughness of the surface of the pellets after polishing with 1 μm diamond pastes. However, due to the dispersion of local density of grain boundaries and other crystal defects, the markers are spread out with marginal errors. Due to this the partial layer thickness ratio $\Delta x_B / \Delta x_A$ is measured with large errors as

$$\frac{\Delta x_B}{\Delta x_A} = 0.21 \pm 0.07. \quad (3-8)$$

According to theoretical analysis this ratio has no temporal dependence, as steady state is assumed. The fact that the layer growth follows the parabolic rate law indicates steady state. This ratio actually corresponds to the diffusivity ratio D_B/D_A which is essential in calculating the critical decomposition voltage U_d . The theoretical analysis will be given in Chapter 4.

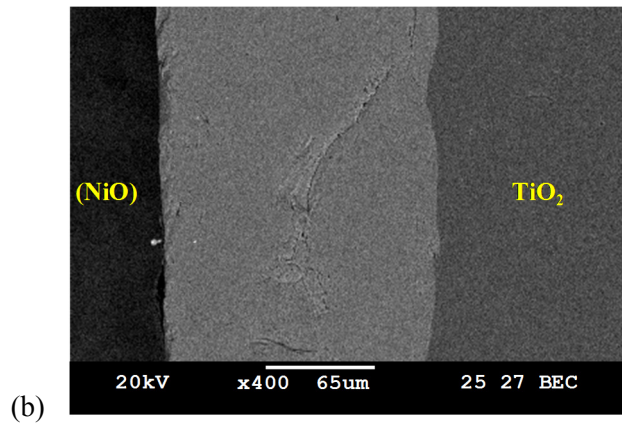
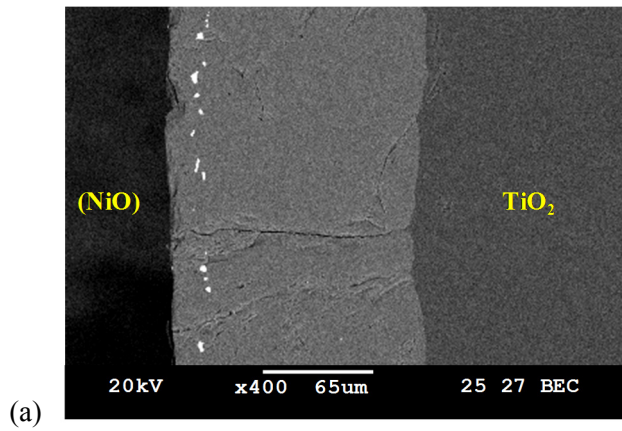
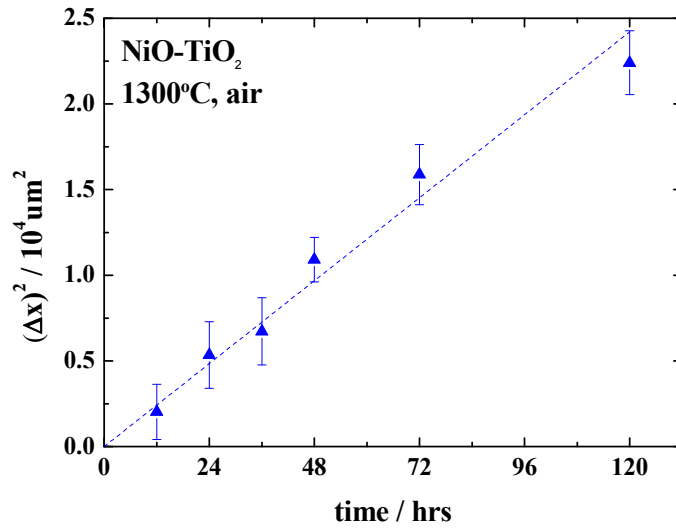
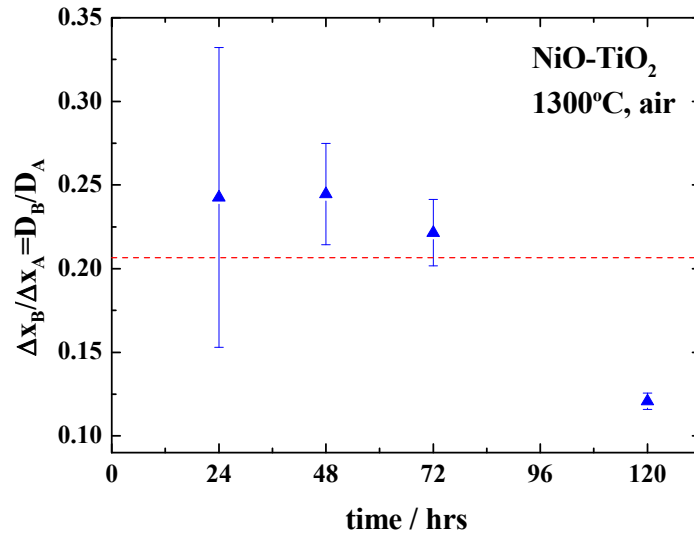


Fig. 3-20. Backscattered images of the reaction couple (a) with Pt-markers (bright spots) embedded and (b) the other blank, simultaneously reacted in the identical surrounding for 120 hrs at 1300°C. Note that the reaction layer thicknesses are the same within experimental error. NiO is written in parentheses to note that it had been there but had spontaneously fallen off.



(a)



(b)

Fig. 3-21. (a) The overall reaction layer thickness and (b) the partial reaction layer thickness ratio vs. reaction duration time of the reaction couple NiO|TiO₂ at 1300°C in air. Dotted lines are the best fits to the theory which will be discussed in upcoming sections.

4. Analysis of the experimental results

To explain the experimental results shown in the previous Chapter, theoretical treatments should be provided. The theoretical treatment of kinetic unmixing and decomposition under electric field, or any other driving force for that matter, stems from that on kinetic unmixing and decomposition under P_{O_2} gradient which was the first studied case. Therefore we will first begin with treatment under P_{O_2} gradient, which was provided by Schmalzried et al., then derive the equation for kinetic decomposition under electric field, which has never been done yet in literature.

After the derivation of critical decomposition voltage, the theory on solid state reaction (diffusion couple) is presented. Finally, the experimental results will be explained with the theoretical analysis. From the comparison it will be seen that the theoretical analysis is sound. Also, as stated in Chapter 2, $BaTiO_3$ showed anomalous behavior under electric field, i.e. neither kinetic unmixing nor decomposition under electric field. A possible reason for this is given with the emphasis on the thermodynamic factor of the system. In short, the following will be given in this Chapter which is the main body of this thesis: (i) theoretical derivation of critical P_{O_2} ratio, according to Schmalzried, (ii) novel theoretical derivation of critical decomposition voltage U_d , (iii) comparison of experimental results with theoretical expectations, therefore confirming the theory, (iv) possible reasons for the behavior of $BaTiO_3$, with emphasis on the thermodynamic factor of the system.

(1) Kinetic decomposition under μ_{O_2} gradient

The phenomenon of kinetic decomposition under P_{O_2} gradient (or μ_{O_2} gradient) was first reported by Schmalzried et al. in the near-stoichiometric systems of $NiTiO_3$ and Co_2TiO_4 [43]. Here, the derivation of the steady state profile will be introduced. Although the overall derivation is similar to that of steady state profile

for kinetic unmixing, there are some crucial points that must be covered. Let us follow through the explanation given by Schmalzried[135] for a spinel AB_2O_4 compound. We assume that the spinel is a semiconducting and that the majority defects are cationic and electronic, i.e. oxygen ions are immobile. Also, AB_2O_4 decomposes into AO and B_2O_3 . By local equilibria



the relationships between the chemical and electrochemical potentials are given as

$$\nabla\eta_{A^{2+}} = \nabla\mu_{AO} - \nabla\mu_O - 2\nabla\eta_{e^-} \quad (4-2)$$

$$\nabla\eta_{B^{3+}} = \frac{1}{2}\nabla\mu_{B_2O_3} - \frac{3}{2}\nabla\mu_O - 3\nabla\eta_{e^-} \quad (4-3)$$

Since the material is a semiconductor and no current flows through the spinel, the electrochemical potential gradient of electrons can be taken as zero. Inserting eqs. (4-2) and (4-3) into eq. (2-3) one gets

$$j_{A^{2+}} = j_A = -c_A b_A (\nabla\mu_{AO} - \nabla\mu_O) \quad (4-4a)$$

$$j_{B^{3+}} = j_B = -c_B b_B \left(\frac{1}{2}\nabla\mu_{B_2O_3} - \frac{3}{2}\nabla\mu_O \right) \quad (4-4b)$$

As the spinel material is a near stoichiometric compound, by Gibbs-Duhem equation $\nabla\mu_{AO} + \nabla\mu_{B_2O_3} = \nabla\mu_{AB_2O_4} \approx 0$. Using this Gibbs-Duhem equation with eqs. (4-4a), (4-4b) and the steady state condition eq. (2-2), we get

$$v_{st} = -b_A(\nabla\mu_{AO} - \nabla\mu_O) = -b_B\left(\frac{1}{2}\nabla\mu_{B_2O_3} - \frac{3}{2}\nabla\mu_O\right) \quad (4-5)$$

and rearranging this by introducing the mobility ratio $\psi = b_B / b_A$ which we assume to be insensitive to concentration we get the relationship between the chemical potential gradient of one component (AO or B₂O₃) and the oxygen chemical potential gradient (since the driving force we are applying is Po₂ gradient) as

$$\nabla\mu_{AO} = \frac{1 - \frac{2}{3}\psi}{1 + \frac{1}{2}\psi} \nabla\mu_O. \quad (4-6)$$

Eq. (4-6) is, after a few rearrangements, is eq. (2-7) rewritten. However, here comes a change. Since spinels have very limited range of composition unlike complete solid solutions, they decompose after a rather small unmixing. When a Po₂ gradient is applied to the surfaces, internal $\nabla\mu_O$ is built and accordingly $\nabla\mu_{AO}$ is built. The maximum chemical potential gradient of AO $\nabla\mu_{AO}^{\max}$ which the spinel can sustain is found by quasi-binary approach, wherein the original spinel and their respective decomposed oxides are assumed to be in equilibrium at the respective surfaces. The configuration is given as Fig. 4-1.

At the surface where AO is formed (and therefore AO and AB₂O₄ are deemed to be in equilibrium), the chemical potential of AO is given simply by its standard state chemical potential $\mu'_{AO} = \mu^{\circ}_{AO}$, as AO is at standard state. At the opposite surface B₂O₃ and AB₂O₄ are in equilibrium so they are at their standard states, i.e. $\mu''_{B_2O_3} = \mu^{\circ}_{B_2O_3}$ and $\mu''_{AB_2O_4} = \mu^{\circ}_{AB_2O_4}$. By local equilibrium, $\mu_{AO} + \mu_{B_2O_3} = \mu_{AB_2O_4}$ so the chemical potential of AO at this surface is given as

$$\mu_{AO}'' = \mu_{AB_2O_4}'' - \mu_{B_2O_3}'' = \mu_{AB_2O_4}^{\circ} - \mu_{B_2O_3}^{\circ} \quad (4-7)$$

Therefore, when kinetic unmixing in the spinel phase is at its full extent and decomposition begins to occur the chemical potential difference at the surfaces is

$$\Delta\mu_{AO}^{\max} = \mu_{AO}'' - \mu_{AO}' = (\mu_{AB_2O_4}^{\circ} - \mu_{B_2O_3}^{\circ}) - \mu_{AO}^{\circ} = \Delta G_{AB_2O_4}^{\circ} \quad (4-8)$$

Eq. (4-8) states that, the maximum chemical potential difference a system can endure is the Gibbs free energy of formation of the material. Equation (4-6) can be integrated as

$$\Delta\mu_{AO} = \frac{1 - \frac{2}{3}\psi}{1 + \frac{1}{2}\psi} \Delta\mu_O \quad (4-9)$$

Therefore, inserting eq. (4-8) into eq. (4-9) along with replacing $\Delta\mu_O$ by

$$\Delta\mu_{O_2} = \frac{1}{2} RT \Delta \ln P_{O_2},$$

$$\ln \frac{P_{O_2}''}{P_{O_2}'} \geq 2 \frac{1 + \frac{1}{2}\psi}{1 - \frac{3}{2}\psi} \frac{\Delta G_{AB_2O_4}^{\circ}}{RT} \quad (4-10)$$

In other words, when we apply a P_{O_2} ratio greater than the right-side of eq. (4-10), kinetic decomposition would occur. The inequality arises from replacing $\Delta\mu_{AO}$ with $\Delta\mu_{AO}^{\max}$. The mobility ratio ψ will affect which compound will appear on which side. If $b_B > \frac{3}{2}b_A$, AO will appear on the high P_{O_2} side and if $b_B < \frac{3}{2}b_A$ it

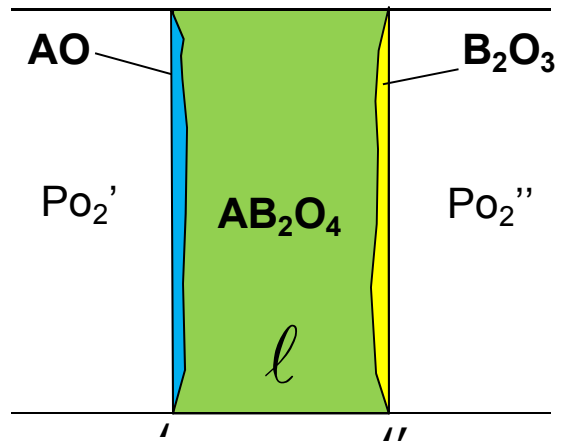


Fig. 4-1. Schematic configuration of the decomposition cell. According to quasi-binary approach, AO is in equilibrium with AB_2O_4 at interface ' and B_2O_3 in equilibrium with AB_2O_4 at interface ". l is the thickness of the specimen.

will appear on the low P_{O_2} side. If $b_B = \frac{3}{2}b_A$, the critical P_{O_2} ratio will diverge to infinity, meaning that no decomposition would occur.

In the above discussion, there were some more assumptions than the ones stated, for example, the cross coefficients were assumed to be negligible and the cation mobility ratio ψ is constant with respect to the local chemical potential of oxygen. Since the first assumption concerning cross effect had already been discussed by Martin and Schmackpfeffer[53], let us look into the second assumption. The cation mobility ratio ψ is defined as b_B/b_A , the ratio of mechanical mobility. According to Einstein relation $D_k = b_k k_B T$ (k_B : Boltzmann constant), so ψ is also the ratio D_B/D_A . Self diffusion coefficient of a component is related to that of its defect such as vacancies as

$$D_k c_k = D_{V_k} c_{V_k} . \quad (4-11)$$

Let us take an atomistic picture. By defect chemistry the number of vacancies will differ with the surrounding thermodynamic variables such as temperature and P_{O_2} , although they will be very low in concentration compared to the lattice sites ($c_{V_k} \ll c_k$). Therefore vacancies would act as ideally diluted solutes and be non-interacting with each other. From the standpoint of a vacancy on lattice site k , it can jump to any nearest neighbor site which is filled with an atom (or ion) of type k . However, atom (or ion) k can only jump when a vacancy is situated at its nearest neighbor site and can only jump in that direction. Once it completes the jump, it has higher tendency to jump back to where the vacancy is, i.e. the jumps of an atom are correlated and its jumping frequencies are anisotropic. Therefore the self diffusivity of an atom which is a function of its jump frequency is not constant – the self diffusivity of its vacancies is – and as the concentration of vacancies changes with temperature and P_{O_2} , the self diffusivity of an atom is a function of

temperature and P_{O_2} .

Also, unlike homovalent complete solid solutions like (Co,Mg)O wherein the cations migrate through the same sublattice so that their diffusion coefficients have the same P_{O_2} dependence, in near stoichiometric compounds the cations are heterovalent and mostly migrate through different sublattices, resulting in different P_{O_2} dependences. Therefore, strictly speaking, ψ is a function of P_{O_2} and may not be taken as constant. Following this train of thought, eq. (4-6) should be integrated instead as

$$\int_1^n d\mu_{AO} = \int_1^n \frac{RT}{2} \frac{1 - \frac{2}{3}\psi(P_{O_2})}{1 + \frac{1}{2}\psi(P_{O_2})} d \ln P_{O_2}. \quad (4-12)$$

Since ψ is now a function of P_{O_2} , the critical P_{O_2} ratio determined by eq. (4-8) will be dependent on which range P_{O_2}' and P_{O_2}'' are located. In such case, even when a fixed P_{O_2} ratio is applied to a system (i.e. $P_{O_2}'' / P_{O_2}' = 10^3$) kinetic decomposition may or may not occur depending on where P_{O_2}'' lies (i.e. $P_{O_2}'' = 10^{-2}$ atm vs. $P_{O_2}'' = 10^{-8}$ atm). This dependency was shown experimentally by Brinkmann and Laqua[67] and Jacob and Shukla[63], as stated in Chapter 2.

However, as the phase stability range of near-stoichiometric compounds is narrow, it can be assumed that the range of existence of ψ is narrow and that ψ can be taken as the average of $\psi(P_{O_2}')$ and $\psi(P_{O_2}'')$, in which eq. (4-9) can be written as

$$\ln \frac{P_{O_2}^*}{P_{O_2}} \geq 2 \frac{1 + \frac{1-\bar{\psi}}{2}}{1 - \frac{3-\bar{\psi}}{2}} \frac{\Delta G_{AB_2O_4}^{\circ}}{RT} \quad (4-13)$$

where $\bar{\psi}$ is the average of ψ over the stability field of the spinel compound. Of the literature reporting kinetic decomposition the only experimental proof that eq. (4-10) is correct or not had been given by the fore-mentioned works of Brinkmann and Laqua, and Jacob and Shukla. However, instead of finding the value ψ and calculating the critical P_{O_2} ratio, they applied various P_{O_2} ratios to obtain the ψ values at each P_{O_2} range. They obtained different values for each P_{O_2} range, but the results were not cross-checked by i.e. inert marker experiments.

(2) Kinetic decomposition under electric field

The critical driving force was found as a function of the cation mobility ratio and the Gibbs free energy of formation of the compound. When the driving force is changed eq. (4-6) stays the same except that the left side changes into a form representing the new driving force. This has been shown for a spinel material under nonhydrostatic stress by Dimos et al.[97], although no experimental proof had been reported.

The case of electric field as driving force is different. Electric field is the only case in which electric current is flown by external force, connected by an external circuit. In most literature concerning kinetic unmixing under electric field, the driving force was applied potentiostatically in a two-probe setup. However, this means that some part of the driving force would be consumed at the interface between the specimen and the electrode, so that we cannot correctly know the driving force that is applied *to the specimen*, unless the specimen is large enough so that inner probes can be attached to achieve a four-probe configuration so we can extrapolate the voltage drop at the inner probes to the whole specimen length. Therefore in a two-probe setup it would make more sense to apply the driving force in a galvanostatic manner and during deriving the equation for the critical electric field, galvanostatic method is implied.

(a) The Gibbs Theorem – its derivation and limitations

Before we derive the novel equation for the electric field case, however, we must first look back in the history, to see whether any attempts to find the threshold voltage for decomposition under electric field had been done in literature. One such account was found, namely the Gibbs theorem.

The Gibbs theorem, which is expressed as $\Delta G = -nFE$, gives the amount of electrical work or electromotive force that can be produced from a given chemical reaction, i.e. it converts chemical energy into electrical energy. In his work

Equilibrium of Heterogeneous Substances[136] Gibbs defined the "fundamental equations," equations from which all the thermal, chemical and mechanical properties can be deduced. They were defined in his notation as

$$\psi = \varepsilon - t\eta, \quad (4-14a)$$

$$\chi = \varepsilon + pv, \quad (4-14b)$$

$$\zeta = \varepsilon - t\eta + pv, \quad (4-14c)$$

where ε is the internal energy, t the absolute temperature, η the entropy, p the pressure and v the volume of the system in consideration. Gibbs termed ψ as the *force function for constant temperature* and χ as the *heat function for constant pressure*. ζ was not specifically named. We can see that they are in our modern day terms the Helmholtz free energy ($A=U-TS$, often F is used as the symbol for Helmholtz free energy but to avoid confusion with the Faraday constant, A is here used), the enthalpy ($H=U+pv$) and the Gibbs free energy ($G=H-TS=U-TS+pv$), respectively.

In Gibbs' work one of the points of interest was how much work can be performed by a system under given thermodynamic conditions (i.e. isothermal, isobaric, etc.), especially in certain *fluids* classified as "*electrolytic conductors*." One reason why only electrolytes – not electronic-conducting semiconductors – were considered was that the existence of electrons was not found until 1897 by Thompson. As Gibbs wrote,

“...we may suppose that electricity (positive or negative) is inseparably attached to the different kind of molecules...”

all electricity was thought to be carried by charged molecules or *ions*. Liquid or aqueous electrolytes were found before solid electrolytes – i.e. the Voltaic pile – and although the concept of solid electrolytes was already demonstrated by

Cavendish (1774)[137], Gaugain (1853)[138] and Buff (1854)^a [139], their characteristics were not yet well understood at Gibbs' time, thus the focus on *fluids*^b. It was not until the appearance of Nernst glowers (1899) that solid electrolytes appeared in the mainstream of electrochemistry.

To begin with, Gibbs defined the system as a *perfect electrochemical apparatus*, i.e. no changes take place in the cell except during the passage of the current and all the changes which accompany the current can be reversed by reversing the current (reversible cells). The 1st law of thermodynamics state that

$$d\varepsilon = dQ - dW , \quad (4-15)$$

with dQ defined as the heat absorbed by the system and dW the work done by the system. Here, Gibbs considered as a general case four different kinds of external actions that a cell is subjected to, namely i) the supply of electricity at one electrode and the withdrawal of the same quantity at the other electrode ($=dW_e$, the electrical work), ii) the supply or withdrawal of a certain amount of heat dQ , iii) the action of gravity dW_g and iv) the motion of the surfaces enclosing the apparatus dW_p , therefore the total work dW equaling $dW_e+dW_g+dW_p$. It should be noted that there is no mention of the pv -work that occurs during the passage of an electrical current and seems to be neglected in Gibbs' consideration^c. This omission of pv -work, as will be shown later, is the difference between Gibbs free energy and

^a Cavendish observed an increase in the conductivity of glass upon heating. Gaugain discovered the solid electrolyte galvanic gas cells while Buff demonstrated galvanic cells and batteries free of water wherein the glass takes over the role of the moist conductor.

^b The term "solid electrolyte" was in use by the end of the 19th century

^c The notion of pv -work was first introduced by Clapeyron in 1834, much before Gibbs. Therefore it is perplexing to see that no mention of pv -work was given by Gibbs.

Helmholtz free energy.

The 2nd law of thermodynamics declared by Clausius is given as

$$d\eta = \frac{dQ}{t} \quad (4-16)$$

for reversible isothermal processes. The two thermodynamic laws eqs. (4-15) and (4-16) combine to give

$$dW = dW_e + dW_g + dW_p = -d\varepsilon + td\eta . \quad (4-17)$$

The right-hand side of eq. (4-17), according to eq. (4-14a), is equal to $-d\psi$ for isothermal conditions, meaning that the magnitude of ψ represents the total work of a system. When we neglect the gravitational work and the work arising from the motion of surfaces, only electrical work remains, i.e.

$$dW_e = -d\varepsilon + td\eta = -d\psi . \quad (4-18)$$

From physics, we know that electrical work defined as the product of electromotive force^d ($V''-V'$, where V' and V'' are the electric potentials at anode and cathode, respectively) and the amount of charge δe that had been flown through the system. Therefore electrical work can be represented as

$$dW_e = (V'' - V')\delta e . \quad (4-19)$$

^d The "force" in electromotive force is not a mechanical force, but is named to indicate potential.

Combining eqs. (4-18) and (4-19) leads to

$$dW_e = (V'' - V')\delta e = -d\psi \quad (4-20)$$

and when integrated for the whole process can be written in our modern day notation with $V'' - V' = E$ and $\delta e = nF$ as

$$-A = nFE. \quad (4-21)$$

One may realize that eq. (4-21) is different from the Gibbs theorem, in that Helmholtz free energy is used instead of Gibbs free energy. As we know, the Helmholtz free energy and Gibbs free energy both set the criterion for equilibrium albeit under different conditions, i.e. Helmholtz free energy under isothermal condition and Gibbs free energy under isothermal *and* isobaric conditions. Gibbs, after arriving at eq. (4-21) and restating eq. (4-14c), expanded it to

$$(V'' - V')\delta e = -d\zeta \quad (4-22)$$

under constant temperature and pressure. However, as stated before, Gibbs did not comment on the pv term which is the difference between eqs. (4-20) and (4-22). If there is no volume change with the passage of current, eqs. (4-20) and (4-22) would be equal. As Gibbs did not consider the pv -work during his derivation, it seems that this is the reason for such expansion from eq. (4-20) to (4-22).

As mentioned before, Gibbs, in his work, did not name the thermodynamic potentials he defined in eqs. (4-14a) to (4-14c). It was in an independent work by Helmholtz[140] where the term *free energy* was first introduced. Helmholtz defined the free energy in his notation as $F = U - \mathcal{J}\theta S$ (with θ the absolute temperature and \mathcal{J} the conversion factor from mechanical to thermal quantity), and in similar manner

as Gibbs showed that for isothermal changes the function F coincides with the value of *work convertible without limit*, i.e. all external reversible work corresponds to change of the function F as $dW=-dF$. This *convertible work* was used in contradiction to *bound work*, which is the heat that is accompanied during the process. One should note that again (in modern day notation) Helmholtz free energy (A or ψ) was used instead of Gibbs free energy (G or ζ), with no comment on the p - v -work that is required to create such a system.

The work of Gibbs and Helmholtz both showed one conclusion - that the maximum available work is given by the free energy A . However, although risking being repetitive it should be again noted that the maximum available work is the sum of p - v -work which is done against the constant pressure of the atmosphere and other works (such as electrical, gravitational, etc.). The p - v -work must always be done when a process occurs at constant pressure - unless there is no volume change - which means it should not be counted as *usable* work. Lewis and Randall in their textbook *Thermodynamics*[141] defined this remainder the *net work* as

$$w' = w - p\Delta v . \quad (4-23)$$

With this definition, one can see the difference between the Helmholtz free energy A and Gibbs free energy G (Lewis and Randall denoted G as F , but for clarity's sake we write here in modern day notation G). For isothermal and reversible process, the maximum work was given as the negative value of change of Helmholtz free energy, i.e. $dw=-dA$. Therefore the net work which is available is

$$w' = \Delta A - p\Delta v = \Delta G . \quad (4-24)$$

As the electrical work that is performed is independent from p - v -work, and since in most chemical reactions the conditions are isothermal and isobaric, it is fitting to use $-\Delta G$ instead of $-\Delta A$ for maximum work and is so defined by Lewis and Randall,

arriving at the modern day form of Gibbs free energy.

The experimental confirmation of Gibbs theorem in galvanic cells can be done by comparing the thermochemical data with those obtained from Gibbs theorem and seems to be first done by Haber and Moser in 1905[142]. Another earlier example can be found in the textbook by Guggenheim[143] for the system of AgI. Also, some examples involving oxygen-conducting electrolytes can be found in the work by Kiukkola and Wagner[144] and other researchers[145-147].

It seems that one of the first practical usage of Gibbs theorem was the extraction of metal aluminum from molten cryolite. Cryolite can easily be saturated with aluminum oxide but melts at 1012°C which is much lower than the melting point of pure alumina (α -Al₂O₃: 2054°C). Many researchers tried to figure out the minimum voltage that is required to obtain metal aluminum[148-152]. In calculating, the authors all used Gibbs theorem while naming the electromotive force E as *decomposition voltage* or *minimum electromotive force required for decomposition*. The experimental results showed that the calculation results were correct within experimental error limits, signifying that Gibbs theorem is applicable for both galvanic and electrolytic cells, provided that the system is an electrolyte.

However, when the material is not an electrolyte, leakage current due to the transport of electrons occurs within the system which reduces the obtainable electromotive force in galvanic cells. In semiconductor cells the applied electric potential gradient is spent by this leakage current, reducing the build-up of the chemical potential gradients that are required for decomposition to occur. Theoretically, a perfect binary semiconductor cannot be decomposed under electric field as infinite amount of driving force is needed.

Therefore, in semiconductors the Gibbs theorem is no longer applicable. However, many complex materials that we use in devices under various thermodynamic

driving forces are semiconductors, and the decomposition voltage of such materials is a prerequisite information for designing safer operating environment of the devices – how much electric potential gradient can this material endure? A difference between binary semiconductors and ternary (or higher) semiconductors is that in ternary semiconductors there are multiple cations, generally with different mobility, and although their transference numbers are small they do migrate to create concentration gradients. The following section therefore is devoted to deriving the decomposition voltage U_d in ternary semiconductors.

(b) Novel derivation of decomposition voltage U_d

Let us assume an $A^{2+}B^{4+}O_3$ near-stoichiometric compound which is a semiconductor and that the majority defects are on the cation sublattice rather than the oxygen sublattice. The system setup is as shown in Fig. 4-2. Local equilibria prevails and cross effect is neglected. Also, both surfaces are exposed to equal P_{O_2} , so $\nabla\mu_{O_2} = 0$. The fluxes of cations are given according to eq. (2-3) under local equilibria as

$$j_{A^{2+}} = j_A = -c_A b_A \nabla \eta_{A^{2+}} = -c_A b_A (\nabla \mu_{AO} - 2 \nabla \eta_e) \quad (4-25a)$$

$$j_{B^{4+}} = j_B = -c_B b_B \nabla \eta_{B^{4+}} = -c_B b_B (\nabla \mu_{BO_2} - 4 \nabla \eta_e). \quad (4-25b)$$

Here, since we will apply electric current externally, the electrochemical potential gradient of electrons cannot be neglected. This is the main difference compared to the P_{O_2} case and other cases and is a unique feature of the electric field case. Inserting eqs. (4-25a) and (4-25b) into eq. (2-2) we get

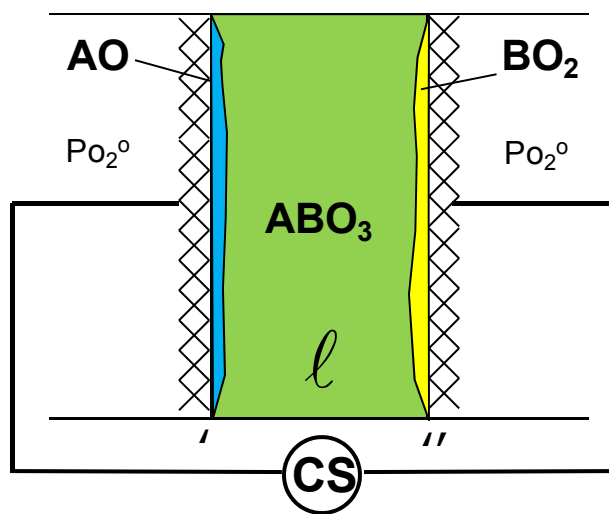


Fig. 4-2. Schematic diagram of ABO_3 under electric field undergoing kinetic decomposition.

$$v_{st} = -b_A (\nabla \mu_{AO} - 2\nabla \eta_e) = -b_B (\nabla \mu_{BO_2} - 4\nabla \eta_e) \quad (4-26)$$

which can be rewritten by again introducing $\psi = b_B / b_A$ and using Gibbs-Duhem equation as

$$4\nabla \eta_e = -\frac{2+2\psi}{1-2\psi} \nabla \mu_{BO_2} \quad (4-27)$$

where we have expressed the relationship between the electrochemical potential gradient of electrons and the chemical potential gradient of a component (AO or BO₂).

This so far is analogous to the Po₂ case except that the electrochemical potential gradient of electrons had not been neglected. However a second unique equation is required in the electric field case, the closed-circuit condition, because of the galvanostatic condition. The closed-circuit condition is given as

$$\sum_k i_k = -\frac{\sigma_A}{2F} \nabla \eta_{A^{2+}} - \frac{\sigma_B}{4F} \nabla \eta_{B^{4+}} + \frac{\sigma_e}{F} \nabla \eta_e = i_{\text{appl}} \quad (4-28)$$

where σ_k is the partial conductivity of species k, F the Faraday constant and i_{appl} the applied electric current density. Since the compound is a semiconductor, $\sigma_e \approx \sigma_{\text{tot}}$ and defining the transference number $t_k = \sigma_k / \sigma_{\text{tot}}$ eq. (4-28) can be modified as

$$4\nabla \eta_e = (t_B - 2t_A) \nabla \mu_{BO_2} + \frac{4i_{\text{appl}} F}{\sigma_{\text{tot}}} \quad (4-29)$$

To find the relationship between the applied current (density) and the chemical

potential gradient of a component AO (BO_2), we eliminate the electrochemical potential gradient of electrons. By combining eqs. (4-27) and (4-29) we can achieve this as

$$\left[-\frac{2+2\psi}{1-2\psi} + (2t_A - t_B) \right] \nabla \mu_{\text{BO}_2} = \frac{4i_{\text{appl}}F}{\sigma_{\text{tot}}} \quad (4-30)$$

which can be rewritten and integrated as

$$\int_0^\ell \left[-\frac{2+2\psi}{1-2\psi} + (2t_A - t_B) \right] d\mu_{\text{BO}_2} = \int_0^\ell \frac{4i_{\text{appl}}F}{\sigma_{\text{tot}}} d\xi. \quad (4-31)$$

Assuming that ψ , σ_{tot} and t_{cat} are constant within the narrow stability regime of ABO_3 eq. (4-31) can be written as

$$\left[-\frac{2+2\psi}{1-2\psi} + (2t_A - t_B) \right] \Delta \mu_{\text{BO}_2} = \frac{4i_{\text{appl}}F}{\sigma_{\text{tot}}} \ell \quad (4-32)$$

where ℓ is the length of the specimen. The quantity $i_{\text{appl}}\ell/\sigma_{\text{tot}}$ is the actual electric field that is applied to the specimen, U . As shown previously, $\Delta \mu_{\text{AO}}$ can be rewritten as $\Delta G_{\text{ABO}_3}^\circ$ and $\Delta \mu_{\text{BO}_2}$ can be written as $-\Delta G_{\text{ABO}_3}^\circ$, the Gibbs free energy of formation of ABO_3 from AO and BO_2 , according to quasi-binary approach. By replacing with these quantities eq. (4-32) becomes

$$U_d = -\frac{\Delta G_{\text{ABO}_3}^\circ}{4F} \left[-\frac{2+2\psi}{1-2\psi} + (2t_A - t_B) \right]. \quad (4-33)$$

Since the compound is a semiconductor the cation transference numbers can be

neglected. Also, since only the magnitude of U_d is important in determining whether kinetic decomposition occurs under electric field, the absolute value is taken, i.e.

$$U_d = \left| \frac{\Delta G_{ABO_3}^{\circ}}{4F} \frac{2 + 2\psi}{1 - 2\psi} \right| = \frac{|\Delta G_{ABO_3}^{\circ}|}{4F} f(\psi). \quad (4-34)$$

The steady state kinetic decomposition is determined by the cation mobility ratio ψ and $\Delta G_{ABO_3}^{\circ}$. As ψ approaches 1/2 (which in terms of electrochemical mobilities indicates $z_A D_A = z_B D_B$) the electric field required to cause decomposition diverges to infinity, i.e. kinetic decomposition (and unmixing) cannot occur. Although we have neglected the polarity of U , the polarity of U does indicate at which surface AO and BO₂ would appear. The function $f(\psi)$ in eq. (4-34) is represented as a function of ψ in Fig. 4-3.

There is an issue we must take into account considering ψ . As we saw in the Po₂ case, the critical driving force was dependent on $\psi(Po_2)$ and was a function of the Po₂ range in which experiments were held in. Since U is the difference of electric potential between the surfaces, $U = \phi'' - \phi'$, what if the same U is applied but at different potential values (i.e. 110 V-100 V vs. 210 V-200 V)? However, the issue is moot. A thermodynamic property is defined by at least two thermodynamic variables such as temperature or pressure. However, electric potential is not a thermodynamic variable and itself has no physical meaning. No phenomenon arises from the existence of just single potential, rather, two potentials are needed for a charged component to migrate and the difference of these potentials is the driving force in which charged particles are driven upon, the electric field.

Although both the chemical potentials and electric potentials share the term "potential," they are different in that chemical potential is a thermodynamic

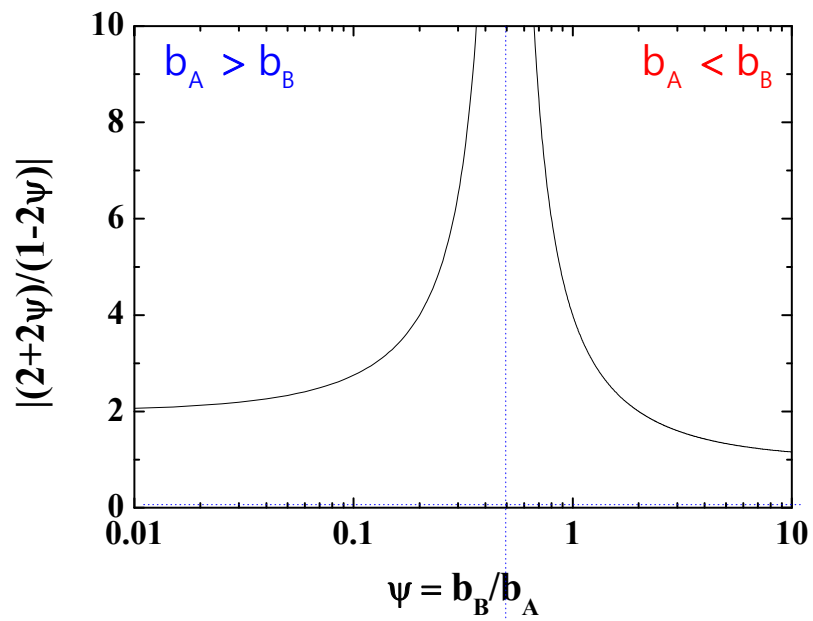


Fig. 4-3. The values of $f(\psi) = |(2+2\psi)/(1-2\psi)|$ as function of ψ . As ψ approaches $1/2$, one can see that the function explodes to infinity.

property while electric potential is not. Rather, electrochemical potential gradient is a thermodynamic property, and by looking at the definition $\eta_k = \mu_k + z_k F \phi$ one can see that the electric potential just acts as a displacement of electrochemical potential from chemical potential. To sum up electric potential is not a thermodynamic property and does not have any relationship with thermodynamic variables such as T or P (i.e. the electric potential would not change when temperature is increased) it would not have effect on defect chemistry and therefore on transport properties. Of course, electric field which is the gradient of electric potentials does affect the transport properties of a material.

There is another thing that we must see from eq. (4-34). When A-site cation is much faster than the B-site cation, $\psi \rightarrow 0$ and $f(\psi) \rightarrow 2$. Combined with the rest of the equation Eq. (4-34) becomes

$$U_d = \frac{|\Delta G_{ABO_3}^{\circ}|}{2F}. \quad (4-35)$$

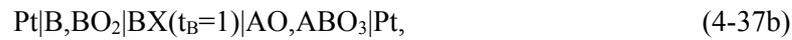
On the other hand, if B-site cation is much faster than the A-site cation, $\psi \rightarrow \infty$ and $f(\psi) \rightarrow 1$, resulting in

$$U_d = \frac{|\Delta G_{ABO_3}^{\circ}|}{4F}. \quad (4-36)$$

What eqs. (4-35) and (4-36) mean is that when a particular cation species is dominantly faster than the other, the decomposition voltage acts becomes the same magnitude as the electromotive force for the corresponding galvanic cell expected from the Gibbs theorem. If the total reaction in the galvanic cell occurred by the ionization of A as $A=A^{2+}+2e^-$, for example, $n=2$ and the electromotive force will be given by eq. (4-23). If it occurs by the ionization of B as $B=B^{4+}+4e^-$, $n=4$ and the

electromotive force becomes analogous to eq. (4-24). However, if the diffusion coefficients of both cations are comparable, discrepancy between the electromotive force of the galvanic cell and the decomposition voltage arises.

If we state the above statement a bit more specifically, it can be done as follows. Eqs. (4-35) and (4-36) can be thought from the perspective of galvanic cells wherein the formation reactions of ABO_3 occur. When we consider galvanic cells of ABO_3 with either A-conducting or B-conducting electrolytes (here written simply as AX or BX), i.e. in the form



in these galvanic cells, at the left-hand side the reaction



would occur, while at the right-hand side the reaction



occurs. The total reaction is the formation of ABO_3 from AO and BO_2 , with the electromotive force calculated according to eqs. (4-35) and (4-36). In other words, when one cation species is dominantly faster, the decomposition voltage U_d is simplified into a form analogous to Gibbs theorem.

The big question is, is eq. (4-34) really true and can it be confirmed? The comparison with experimental data and eq. (4-34) will be done later in the upcoming sections and the verity of eq. (4-34) will henceforth be confirmed. First, though, we must take into account the most important factor in eq. (4-34), the cation mobility ratio ψ . The cation mobility ratio is obtained from the diffusion couple experiment that was separately performed. This is given in the next section. This experiment also naturally leads us into Chapter 5 where the diffusion couple experiments (in other words, the formation reactions) are done under electric field.

(3) Solid state reaction (diffusion couple) and inert markers

Here we derive how the thickness ratio $\Delta x_B / \Delta x_A$ is related with the diffusion coefficient or mobility ratio ψ . Let us assume that steady state is reached for the reaction. In this case steady state would refer to the system growing in parabolic manner, as shown by Wagner[153]. Also, it would mean that the fluxes of constituent ions are constant. By the definition of flux the flux of A^{2+} and B^{4+} (in mol/cm²·s) are given as

$$j_{A^{2+}} = j_A = -\frac{D_A c_A}{RT} \nabla \eta_{A^{2+}} = -\frac{D_A c_A}{RT} (\nabla \mu_{AO} - 2\nabla \eta_e), \quad (4-40a)$$

$$j_{B^{4+}} = j_B = -\frac{D_B c_B}{RT} \nabla \eta_{B^{4+}} = -\frac{D_B c_B}{RT} (\nabla \mu_{BO_2} - 4\nabla \eta_e), \quad (4-40b)$$

respectively, with D_k and c_k being the self diffusion coefficient and concentration (in mol/cm³) of component k. Again, the chemical potential gradient of oxygen is neglected as there is no P_{O_2} gradient applied. Also, the open-circuit condition gives

$$\sum_k i_k = -\frac{\sigma_A}{2F} \nabla \eta_{A^{2+}} - \frac{\sigma_B}{4F} \nabla \eta_{B^{4+}} + \frac{\sigma_e}{F} \nabla \eta_e = 0 \quad (4-41)$$

which is reduced to, along with local equilibria,

$$(1 + t_A + t_B) \nabla \eta_e \approx \nabla \eta_e = \frac{t_A}{2} \nabla \mu_{AO} + \frac{t_B}{4} \nabla \mu_{BO_2}. \quad (4-42)$$

Inserting eq. (4-42) into eqs. (4-40a) and (4-40b), one obtains

$$j_{A^{2+}} = j_A = -\frac{D_A c_A}{RT} (1 - t_A + \frac{t_B}{2}) \nabla \mu_{AO} \approx -\frac{D_A c_A}{RT} \nabla \mu_{AO}, \quad (4-43a)$$

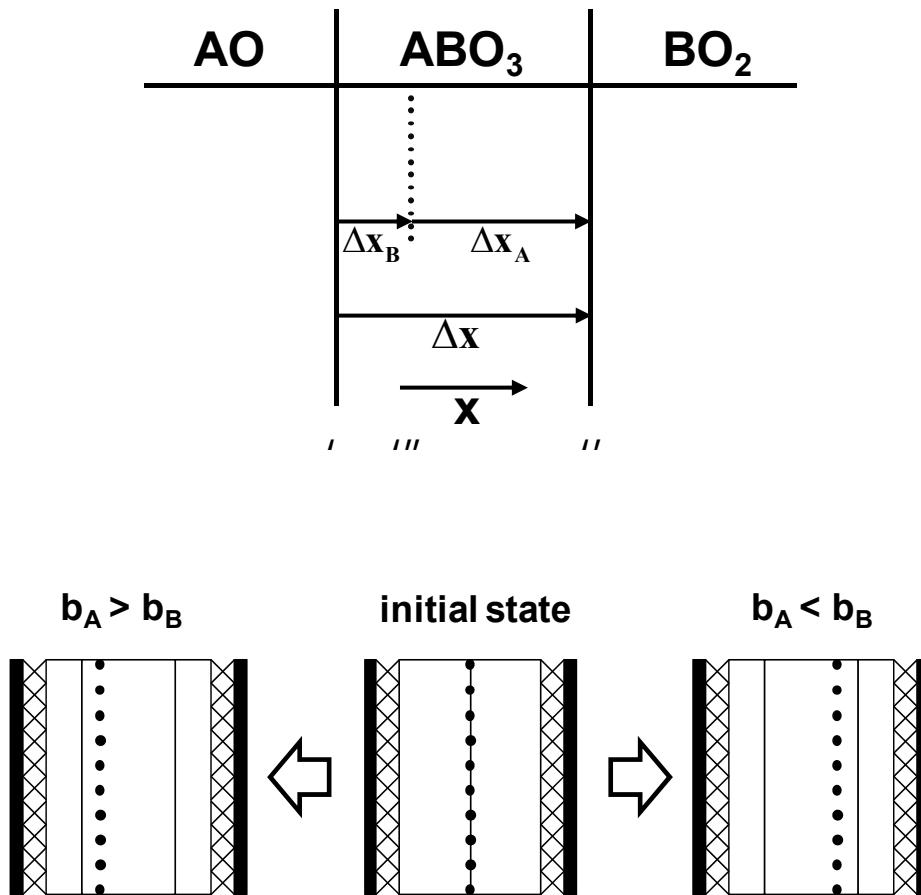


Fig. 4-4. Schematic diagram of AO-BO₂ diffusion couple employing inert markers. The positions are marked by ', " and "'. Figure not drawn to scale. The expected placement of inert markers (•) are shown for $D_A > D_B$ and $D_B > D_A$ in the bottom half.

$$j_{B^{2+}} = j_B = -\frac{D_B c_B}{RT} (1 - t_B + 2t_A) \nabla \mu_{BO_2} \approx -\frac{D_B c_B}{RT} \nabla \mu_{BO_2}. \quad (4-43b)$$

According to the setup as in Fig. 4-4, $j_{A^{2+}}$ will be in the positive x direction, while $j_{B^{2+}}$ will be in the negative x direction. Δx_A is the ABO_3 layer grown by the transport of cation A and Δx_B the layer grown by transport of cation B, both positive quantities. The total flux for ABO_3 , j_{ABO_3} , is then given as

$$j_{ABO_3} = j_A - j_B = \frac{D_A c_A + D_B c_B}{RT} \nabla \mu_{BO_2} = \frac{d\Delta x}{V_m dt}. \quad (4-44)$$

with the right-hand side arising from the steady state assumption. Since $V_m c_k \ll 1$ for systems with very narrow stability regime, and approximating $\nabla \mu_{BO_2}$ as $-\Delta G_f^\circ / \Delta x$, eq. (4-44) is then transformed into the parabolic rate law $(\Delta x)^2 = 2k_p t$, with k_p defined as

$$k_p = -(D_A + D_B) \frac{\Delta G_f^\circ}{RT}. \quad (4-45)$$

The partial layer growths Δx_A and Δx_B can also be obtained. The respective fluxes, again under steady state assumption, can be written as

$$j_{A^{2+}} = j_A = -\frac{D_A c_A}{RT} \nabla \mu_{AO} = \frac{D_A c_A}{RT} \nabla \mu_{BO_2} = \frac{d\Delta x_A}{V_m dt}, \quad (4-46a)$$

$$j_{B^{2+}} = j_B = -\frac{D_B c_B}{RT} \nabla \mu_{BO_2} = \frac{d\Delta x_B}{V_m dt}. \quad (4-46b)$$

The $\nabla \mu_{BO_2}$'s correspond to the gradient of the chemical potential of BO_2 within

the layer Δx_A or Δx_B , respectively. As steady state is assumed, this can again be assumed as $\Delta\mu_{\text{BO}_2} / \Delta x = -\Delta G_f^\circ / (\Delta x_A + \Delta x_B)$ by the rule of similarity. Therefore eqs. (4-46a) and (4-46b) are rewritten as

$$\frac{d\Delta x_A}{V_m dt} = \left| -\frac{D_A c_A}{RT} \frac{\Delta G_f^\circ}{\Delta x_A + \Delta x_B} \right| = \frac{A}{\Delta x_A + \Delta x_B} \quad (4-47a)$$

$$\frac{d\Delta x_B}{V_m dt} = \left| \frac{D_B c_B}{RT} \frac{\Delta G_f^\circ}{\Delta x_A + \Delta x_B} \right| = \frac{B}{\Delta x_A + \Delta x_B} \quad (4-47b)$$

where the absolute values are introduced as only the magnitude of layer thicknesses are of interest. One can see that, compared with eq. (4-45),

$$k_p = V_m (A + B)t \quad (4-48)$$

and that

$$\Delta x = \Delta x_A + \Delta x_B = \sqrt{2V_m (A + B)t} . \quad (4-49)$$

Inserting eq. (4-34) into eqs. (4-32a) and (4-32b), the partial layer thicknesses are written as

$$d\Delta x_A = \frac{A\sqrt{V_m}}{\sqrt{2(A+B)}} t^{-1/2} dt , \quad (4-50a)$$

$$d\Delta x_B = \frac{B\sqrt{V_m}}{\sqrt{2(A+B)}} t^{-1/2} dt . \quad (4-50b)$$

Integrating eqs. (4-50a) and (4-50b) results in

$$\Delta x_A = \frac{A\sqrt{2V_m}}{\sqrt{2(A+B)}} t^{1/2} \quad (4-51a)$$

$$\Delta x_B = \frac{B\sqrt{2V_m}}{\sqrt{2(A+B)}} t^{1/2} \quad (4-51b)$$

One can now divide eq. (4-51b) by eq. (4-51a) to obtain

$$\frac{\Delta x_B}{\Delta x_A} = \frac{B}{A} = \frac{|D_B c_B \Delta G_f^0| / RT}{|D_A c_A \Delta G_f^0| / RT} \approx \frac{D_B}{D_A} = \psi. \quad (4-52)$$

Eq. (4-52) states that one can measure estimate the ratio of cation self diffusivities or mobilities by measuring the respective lengths from the inert markers to the phase boundaries, i.e. the connection between the layer thickness ratio and the diffusion coefficient ratio is made, assuming that steady state is achieved in the system. This principle is applicable to all cation valence combination, i.e. AO-B₂O₃, AO₂-B₂O₃, etc.

The diffusion coefficients can now be independently calculated. Eq. (3-7) showed the fitted result for NiO-TiO₂ at 1300°C as

$$k_p = (2.81 \pm 0.11) \times 10^{-10} \text{ cm}^2/\text{s} \quad (3-7)$$

and from eq. (3-8)

$$\psi = \frac{\Delta x_B}{\Delta x_A} = \frac{b_B}{b_A} = \frac{D_B}{D_A} = 0.21 \pm 0.07, \quad (3-8)$$

where b_k is the mechanical mobility of component k , with the third equality possible by Einstein relation ($D=b_k k_B T$, k_B : Boltzmann constant). Inserting eqs. (3-

7) and (3-8) into eq. (4-45), with $\Delta G_f^\circ = -8,502$ J/mol for NiTiO_3 at 1300°C [110], the diffusion coefficients for Ni and Ti in NiTiO_3 are calculated as

$$D_{\text{Ni}} = (3.6 \pm 0.2) \times 10^{-10} \text{ cm}^2/\text{s}, \quad (4-53a)$$

$$D_{\text{Ti}} = (0.75 \pm 0.26) \times 10^{-10} \text{ cm}^2/\text{s}. \quad (4-53b)$$

(4) Justification of the theory

We have set the theoretical basis of kinetic decomposition in section 2 and that of inert markers in section 3. Let us now apply these theoretical basis to the experimental results obtained from NiTiO₃ shown in Chapter 3. From the inert marker experiment, the partial thickness ratio $\Delta x_B / \Delta x_A = \psi$ was obtained as $\psi = 0.21 \pm 0.07$. This leads to the value of $f(\psi)$ as

$$f(\psi) = \left| \frac{2 + 2\psi}{1 - 2\psi} \right| = \frac{2.42 \pm 0.14}{0.58 \pm 0.14} = 4.2 \pm 1.0. \quad (4-54)$$

Inserting this into Eq. (4-34), while again using the value $\Delta G_{\text{NiTiO}_3}^\circ = -8,502 \text{ J/mol}$ obtained from the work by Jacob et al.[110], the critical decomposition voltage U_d is calculated as

$$U_d = (92 \pm 23) \text{ mV} \quad (4-55)$$

which is about twice larger than the value predicted by Gibbs theorem ($\sim 44 \text{ mV}$), again showing that Gibbs theorem is inadequate in explaining the current phenomena. The experimental results shown in Table 3-3 showed that the critical decomposition voltage is expected in the range of $97 \leq U_d / \text{mV} \leq 120$. The two figures coincide within error range, indicating that the proposed theory is indeed sound. The comparison of theoretical expectations and experimental results is shown in Fig. 4-5. The x-axis of Fig. 4-5 represents the full range of possible ψ , from 0.14 to 0.28. The solid curve represents the theoretical U_d value corresponding to each ψ value, while the shaded area is the window of U_d expected from the experimental results in Table 3-3. While the values coincide within error limits, it can be seen that the experimentally obtained values are on the high ψ side. A possible reason for this may be due to the fact that the 120 hour point in Fig. 3-21 (b) has lower value ($\psi \sim 0.12$) compared to the other points ($\psi \sim 0.24$). The diffusion coefficient

ratio is not a function of time so it should be constant, therefore the ψ value at 120 hours seem to be underestimated for some reason that is unknown as of now.

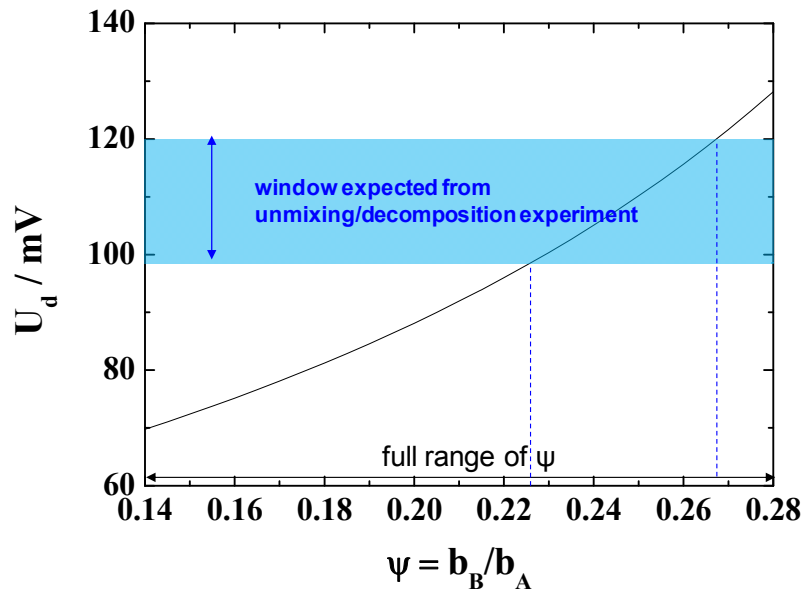


Fig. 4-5. The comparison of experimentally obtained range of U_d and that expected from the theoretical treatment for NiTiO_3 at 1300°C in air. The x-axis is the full range of ψ obtained from inert marker experiment.

(5) Proposal of effect of thermodynamic factor - BaTiO₃

This leads to a proposal for why no decomposition occurred in BaTiO₃. For BaTiO₃, the diffusion coefficient ratio may be very close to 1/2, or in terms of electrochemical mobilities, Ba and Ti may have nearly equal electrochemical mobilities. The cation diffusion coefficients in BaTiO₃ have been reported by Koerfer et al.[154] in single crystals, Wernicke[155] and Kitahara et al.[156] While Koerfer et al and Kitahara et al. reported that Ba is faster than Ti, Wernicke reported that Ba is the slowest species in BaTiO₃. The results are scattered and no conclusive proof has been found declaring which cation is faster. Actually, a simple way to find which cation is faster is, as shown previously, performing formation reaction with BaO and TiO₂, while applying inert markers. There are some problems for this. First, by looking at the phase diagram of the system BaO-TiO₂[157], shown in Fig. 4-6, one can notice that there are many other intermediate compounds around BaTiO₃, such as Ba₂TiO₄, BaTi₂O₅, BaTi₃O₇ and BaTi₄O₉. Therefore, a diffusion couple of BaO-TiO₂ would lead to formation of a series of phases instead of solely BaTiO₃. To obtain only BaTiO₃, a diffusion couple consisting of the adjacent phases is required. However, some additional phases have been said to be found than the ones shown in Fig. 4-6, i.e. there still seems to be some dispute regarding the phases that actually exist in the BaO-TiO₂. This is possible due to the existence of the Ruddlesden-Popper structure phases.

Many works on the cation diffusion in perovskites have been done using both solid state reaction method (diffusion couple) and SIMS analysis. To state the conclusion first, no concrete evidence on which cation is faster has been given. Generally, the A-site cations are deemed to be faster than the B-site cations due to their diffusion paths, as mentioned in Chapter 2. The A-site cations can move in <100> direction, while for B-site cations to jump from one site to another directly, which is in <110> direction, migration energy as large as four times that of A-site migration is required. This had been reported for LaMnO₃[34], LaGaO₃[33] and SrTiO₃[158,159]. Experimentally, the A-site cation was found to be faster in

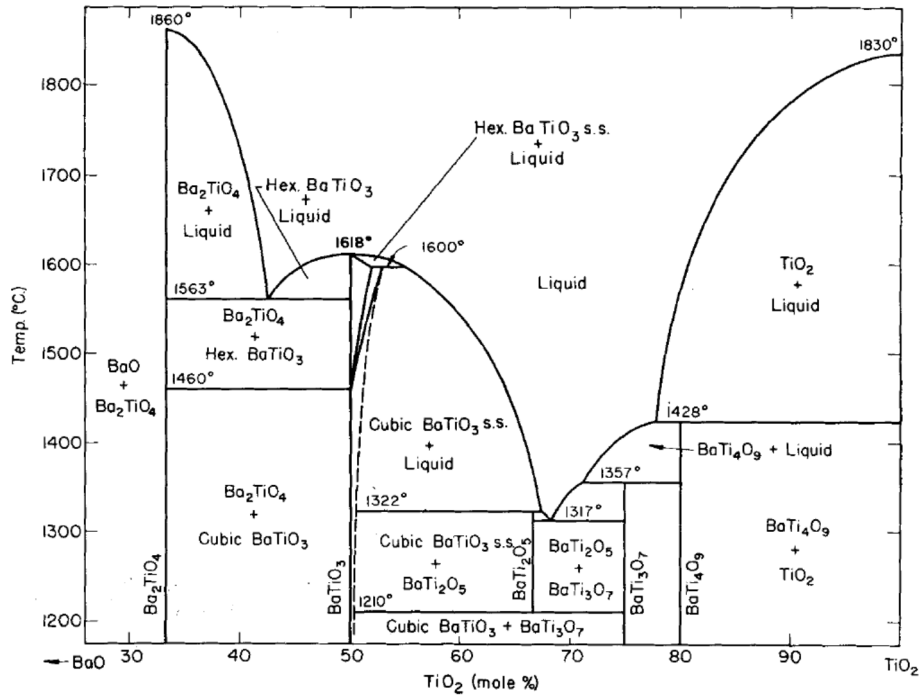
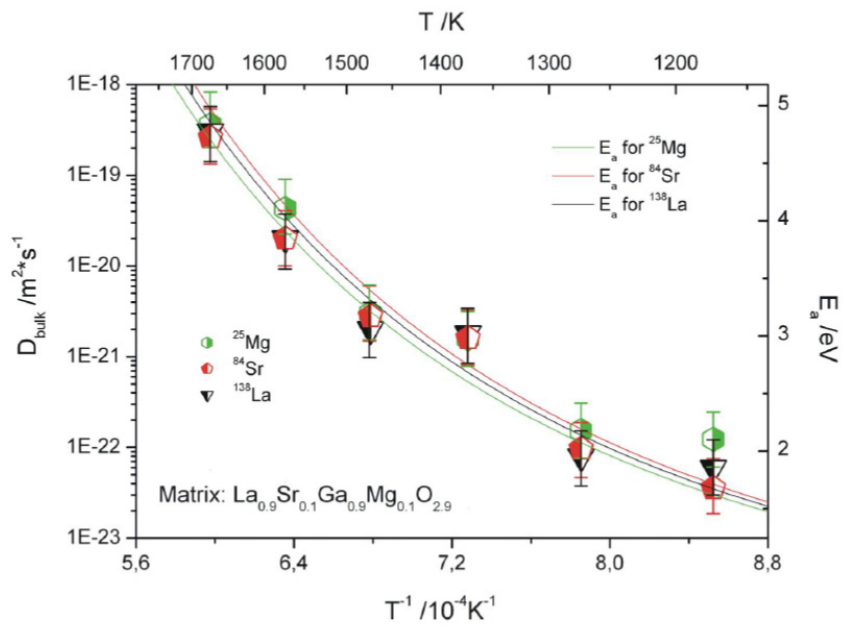
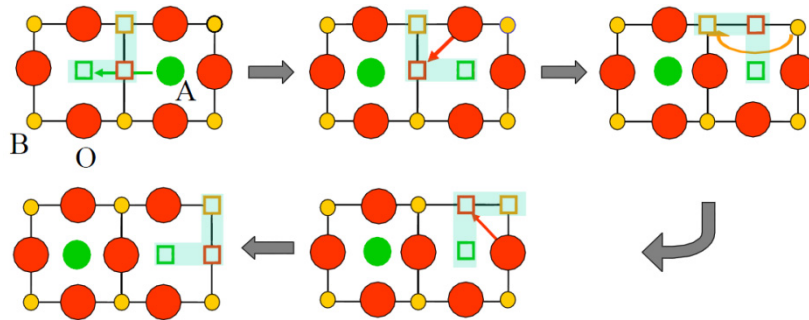


Fig. 4-6. Phase diagram of the system BaO-TiO₂. Unlike the phase diagram of the system NiO-TiO₂ (Fig. 3-4), various intermediate compounds exist around BaTiO₃. From Rase and Roy. [157]



(a)



(b)

Fig. 4-7. (a) The SIMS analysis result of LSGM from Schulz et al. La and Sr are A-site dopants while Mg is a B-site dopant. The SIMS analysis shows practically equal diffusion coefficients for both sites. (b) The proposed vacancy cluster mechanism. The clustered vacancies migrate through a sequence of vacancy jumps. After a sequence is completed, the whole vacancy cluster is migrated. From Schultz et al. [166]

LaCrO₃[160], YCrO₃[161] and NdCrO₃[162]. However, some works report rather that the B-site cations are faster than the A-site cations, such as in LaFeO₃[126], GdFeO₃[163], LaCoO₃[128] and LaMnO₃[164]. Recently, in the works by Kilo et al.[165] and Schultz et al.[166] they showed that the dopants in both A- and B-sites have practically the same diffusion coefficients from SIMS analysis and that they could possibly migrate by vacancy cluster mechanism, as shown in Fig. 4-7, which could explain the practically equal mobility of A- and B-site cations. However, the experimental observation of such vacancy clusters has not yet been provided. Also, their works were based on complex doped perovskites, wherein the dopants may enhance or deter the mobilities of the other ions. No such consideration has been given for pure perovskites.

In other words, combined with the experimental results for BaTiO₃ wherein no decomposition was observed even at applied voltages higher than the expected values[26], the cations Ba and Ti may have equal electrochemical mobilities. This would lead spontaneously to the non-occurring of kinetic unmixing and therefore decomposition. Concerning kinetic unmixing, however, another possibility can be proposed, even if the electrochemical mobilities of cations are quite different. This possibility is the thermodynamic factor of the system.

Let us take eq. (4-30) a bit further, for the treatment of kinetic unmixing. By rearranging and assuming the compound to be a semiconductor, eq. (4-30) can be rewritten as

$$\frac{\nabla \mu_{\text{BO}_2}}{i_{\text{appl}} F / \sigma_{\text{tot}}} = \frac{4\psi - 2}{1 + \psi} \quad (4-56)$$

Now, when one obtains concentration profiles to judge whether kinetic unmixing or decomposition occurred or not, one generally measures the molar composition ratios of A or B, not in chemical potential values as in eq. (4-56). Therefore we

must express eq. (4-56) in terms of the molar fraction of B (or A). By the definition of chemical potential and chain rule

$$\left(\frac{\partial \mu_{\text{BO}_2}}{\partial \ln x_{\text{B}}} \right) \frac{\nabla \ln x_{\text{B}}}{i_{\text{appl}} F / \sigma_{\text{tot}}} = \frac{4\psi - 2}{1 + \psi} \quad (4-57)$$

and by rearranging, with setting $\partial \mu_{\text{BO}_2} / \partial \ln x_{\text{B}} = f_{\theta}$,

$$\frac{\nabla \ln x_{\text{B}}}{i_{\text{appl}} / \sigma_{\text{tot}}} = \frac{1}{f_{\theta} / F} \frac{4\psi - 2}{1 + \psi}. \quad (4-58)$$

The term $\partial \mu_{\text{BO}_2} / \partial \ln x_{\text{B}} = f_{\theta}$ is the thermodynamic factor of the system with units of J/mol (in other literature the thermodynamic factor is defined as $\partial \ln a_{\text{B}} / \partial \ln x_{\text{B}}$, with a_{B} being the activity of B, in which case the thermodynamic factor would be dimensionless). Therefore f_{θ} / F has units of V and is coined as the *voltage equivalent of thermodynamic factor* U^* or

$$U^* = \frac{f_{\theta}}{F}. \quad (4-59)$$

Also, the term $\nabla \ln x_{\text{B}}$ can be approximated as $\Delta \ln x_{\text{B}} / \ell$ for a narrow range of x_{B} , and since the resulting $i_{\text{appl}} \ell / \sigma_{\text{tot}}$ in the denominator of the left-hand side of eq. (4-58) is equal to the applied voltage U , eq. (4-59) can be modified to

$$\frac{\Delta \ln x_{\text{B}}}{U} = \frac{1}{U^*} \frac{4\psi - 2}{1 + \psi} \quad (4-60)$$

and again, for a narrow range of x_{B} , according to the Taylor series

$\ln(1+z) \approx z - \frac{1}{2}z^2 + \frac{1}{3}z^3 \mp \dots$, $\Delta \ln x_B$ can be approximated as

$$\Delta \ln x_B = \ln \frac{x_B''}{x_B'} = \ln \left(1 + \frac{x_B'' - x_B'}{x_B'} \right) \approx \frac{x_B'' - x_B'}{x_B'} = \frac{\Delta x_B}{x_B'}, \quad (4-61)$$

and therefore eq. (4-60) can be approximated as

$$\frac{x_B'' - x_B'}{x_B'} \approx \frac{U}{U^*} \frac{4\psi - 2}{\psi + 1}. \quad (4-62)$$

Let us take a closer look at eq. (4-62). Eq. (4-62) states that, when an electric field U is applied to a material, kinetic unmixing would occur, provided that $\psi \neq 1/2$ (or, in terms of electrochemical mobilities, $z_A D_A \neq z_B D_B$). However, when we apply the electric field, it is scaled by the thermodynamic factor-equivalent U^* . If $0 < U^*/V < 1$, the voltage U one applies will have enhancing effect. If $U^*/V > 1$, the effect of the applied voltage U will be reduced. For an ideal solution the value will be 0.14 V at 1573K ($U^* = RT/F$). However, intermediate compounds cannot be ideal solution, as that would occur in a complete solid solution. As U^* is crucial in determining how much the applied voltage U is scaled, one must find what the physical meaning of U^* is and what the value of U^* would be for the systems in consideration.

Let us assume that the system ABO_3 is a binary solution of AO and BO_2 . Also, let us assume for simplicity that ABO_3 is the sole intermediate compound in the system $AO-BO_2$. The thermodynamic factor in this case is the curvature of the integral molar free energy of mixing of the solution, ΔG^M . Mathematically it is expressed as[167]

$$f_0 \equiv \frac{\partial \mu_{\text{BO}_2}}{\partial \ln x_B} = x_A x_B \frac{\partial^2 \Delta G^M}{\partial x_B^2}. \quad (4-63)$$

Physically, the thermodynamic factor resembles the restorative force of the system. When a system is exposed to a driving force, so that the composition is moved from the equilibrium composition x_B^{eq} to a composition close to it, say x_B^{df} (df signifying driving force) there is inevitable increase in Gibbs free energy. As a system in nature thrives for equilibrium, the composition moves back to the equilibrium composition while emitting the energy. When the curvature is large, then the slope of the Gibbs free energy is also large, meaning that to create an equal amount of shift in composition in two different material systems, the system with larger thermodynamic factor requires larger driving force and the subsequent restorative force would also be larger. Therefore, the system with larger thermodynamic factor would be harder to both unmix and to decompose. This is schematically illustrated in Fig. 4-8.

An intermediate compound is taken to be near-stoichiometric, so the mixing free energy curve can be assumed to be quite sharp. Because of this sharpness, one can assume the tip of the mixing free energy curve as a quadratic function with respect to x_B (or x_A) and that it is symmetric with respect to $x_B^0 \approx 0.5$. The slope is taken as α and the mixing free energy can be represented as

$$\Delta G^M = \frac{1}{2} \Delta G_f^0 + \alpha (x_B - x_B^0)^2 \quad (4-64)$$

where $\frac{1}{2} \Delta G_f^0$ is introduced instead of ΔG_f^0 because for the solution AO-BO₂ the energy (which is the depth of the curve with respect to $\Delta G^M = 0$) is halved. ΔG_f^0 in this case is the formation free energy for ABO₃. By the equilibria between the

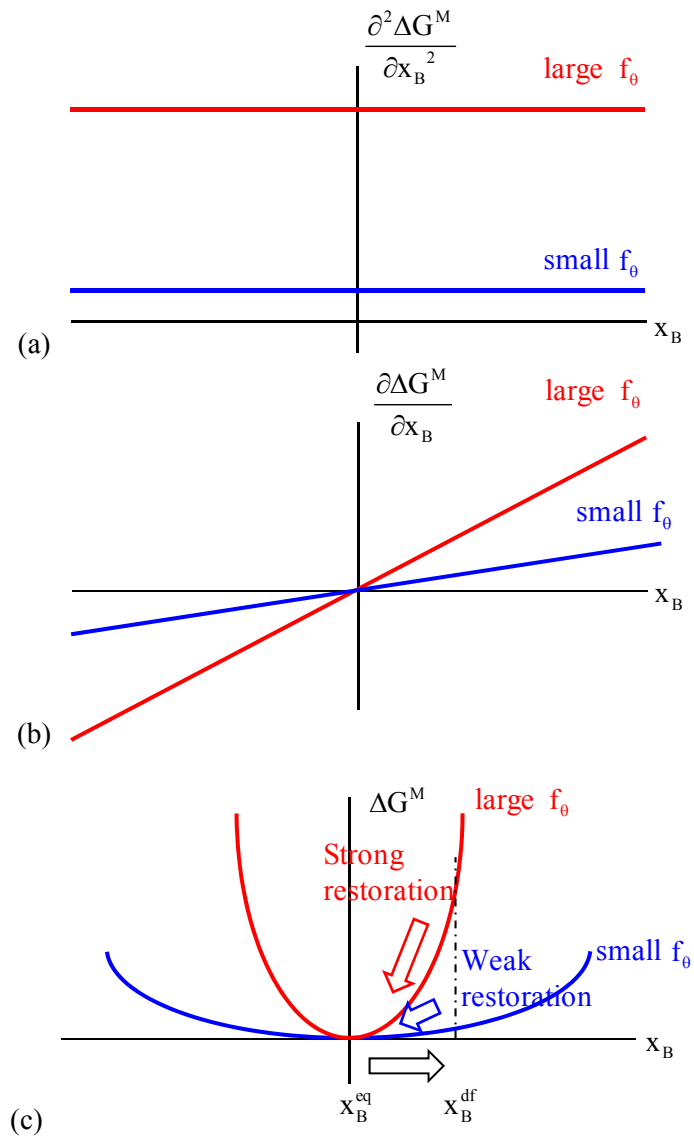


Fig. 4-8. A schematic representation of (a) the curvature of ΔG^M , (b) the slope of composition of the intermediate compound would be $A_{0.5}B_{0.5}O_{1.5}$, so the formation ΔG^M and (c) ΔG^M itself. Illustrations not to scale. In (c), the strong and weak restoration for systems with large/small thermodynamic factor is shown when the composition of the system is moved from its equilibrium composition x_B^{eq} to x_B^{df} .

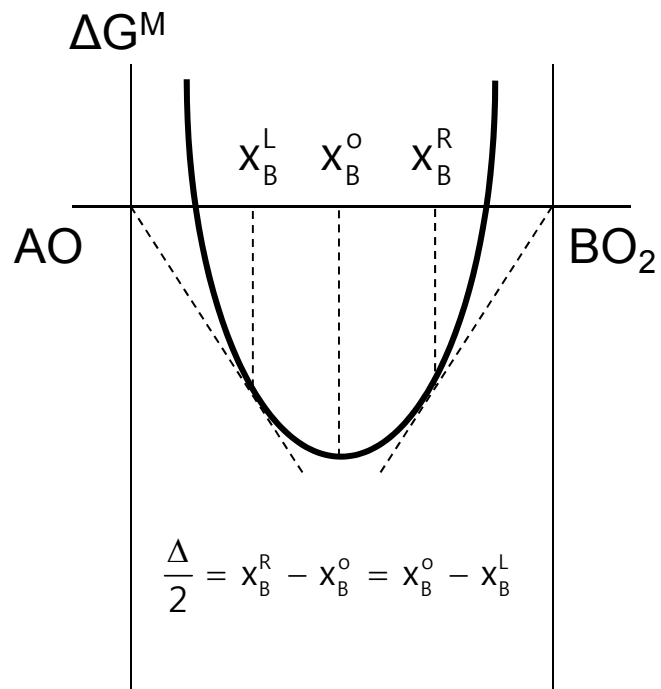


Fig. 4-9. The relationship between the integral mixing free energy and the width of the stability limit.

solution ABO_3 and each component oxide the following relations are valid:

$$\Delta\bar{G}_{AO}^M \Big|_{x_B=x_B^L} = 0 = \Delta G^M - \frac{d\Delta G^M}{dx_B} x_B^L \quad (4-65a)$$

$$\Delta\bar{G}_{BO_2}^M \Big|_{x_B=x_B^R} = 0 = \Delta G^M + \frac{d\Delta G^M}{dx_B} (1 - x_B^R) \quad (4-65b)$$

where x_B^L and x_B^R are the molar fraction of B at the AO-saturated and BO_2 -saturated ABO_3 , respectively. The compositions according to position are given as in Fig. 4-9.

$\Delta\bar{G}_{AO}^M$ and $\Delta\bar{G}_{BO_2}^M$ are the relative partial molar Gibbs free energies of mixing of AO and BO_2 . They are obtained from differentiating the mixing free energy ΔG^M

$$\Delta G^M = x_A \Delta\bar{G}_{AO}^M + x_B \Delta\bar{G}_{BO_2}^M . \quad (4-66)$$

The total differential of eq. (4-66) results in

$$d\Delta G^M = x_A d\Delta\bar{G}_{AO}^M + x_B d\Delta\bar{G}_{BO_2}^M + \Delta\bar{G}_{AO}^M dx_A + \Delta\bar{G}_{BO_2}^M dx_B . \quad (4-67)$$

However, by Gibbs-Duhem equation, $x_A d\Delta\bar{G}_{AO}^M + x_B d\Delta\bar{G}_{BO_2}^M \approx 0$, so eq. (4-67) is simplified to

$$d\Delta G^M = \Delta\bar{G}_{AO}^M dx_A + \Delta\bar{G}_{BO_2}^M dx_B . \quad (4-68)$$

By differentiating eq. (4-68) with respect to x_A , one gets

$$\frac{d\Delta G^M}{dx_A} = \Delta \bar{G}_{AO}^M - \Delta \bar{G}_{BO_2}^M . \quad (4-69)$$

Multiplying eq. (4-69) by x_B and adding eq. (4-66) to it results in

$$\Delta G^M + x_B \frac{d\Delta G^M}{dx_A} = (x_B + x_A) \Delta \bar{G}_{AO}^M = \Delta \bar{G}_{AO}^M \quad (4-70a)$$

and an analogous treatment with x_B results in

$$\Delta G^M + x_A \frac{d\Delta G^M}{dx_B} = \Delta \bar{G}_{BO_2}^M . \quad (4-70b)$$

The partial molar Gibbs free energy of mixing of AO is the y-axis intercept of the tangential line to ΔG^M at $x_A=1$. As ABO_3 is assumed to be the only intermediate compound available in this case, the tangential line drawn at $x_B = x_B^L$ would meet at $\Delta G^M = 0$ at $x_A=1$. This is because AO and ABO_3 are in equilibrium at $x_B = x_B^L$, thus eq. (4-65a). The same principle is applied to BO_2 , therefore eq. (4-65b).

Since we assumed that the curve is symmetric with respect to x_B^o , the range of nonmolecularity is given as

$$x_B^R - x_B^o = x_B^o - x_B^L = \frac{1}{2} \Delta x_B^{\max} . \quad (4-71)$$

By eq. (4-71), eqs. (4-65a) and (4-65b) become redundant. When one inserts eq. (4-65a) or eq. (4-65b) into eq. (4-64), one gets

$$\frac{1}{2}\Delta G_f^o + \alpha(x_B^L - x_B^o)^2 - 2\alpha(x_B^L - x_B^o)x_B^L = 0. \quad (4-72)$$

By expanding,

$$\frac{1}{2}\Delta G_f^o + \alpha(x_B^o - x_B^L)(x_B^o + x_B^L) = 0. \quad (4-73)$$

Since $x_B^o = 0.5$ and we assumed that the phase stability range is very narrow, $x_B^o + x_B^L \approx 1$. Inserting eq. (4-71) into eq. (4-73) one obtains

$$\alpha \approx -\frac{\Delta G_f^o}{\Delta x_B^{\max}} \quad (4-74)$$

and eq. (4-64) is then completed as

$$\Delta G^M = \frac{1}{2}\Delta G_f^o - \frac{\Delta G_f^o}{\Delta x_B^{\max}}(x_B - x_B^o)^2. \quad (4-75)$$

Now we can find the thermodynamic factor according to eq. (4-63). Inserting eq. (4-75) into eq. (4-63) results in

$$f_\theta = x_A x_B \left(-2 \frac{\Delta G_f^o}{\Delta x_B^{\max}} \right) \quad (4-76)$$

and since $x_A x_B \approx 0.25$ because $x_B^o = 0.5$, the final expression for the thermodynamic factor is

$$f_{\theta} \approx -\frac{\Delta G_f^{\circ}}{2\Delta x_B^{\text{tot}}} \quad (4-77)$$

and the voltage equivalent of thermodynamic factor U^* is

$$U^* = \frac{f_{\theta}}{F} \approx -\frac{\Delta G_f^{\circ}}{2F\Delta x_B^{\text{max}}} \quad (4-78)$$

Since $\Delta G_f^{\circ} < 0$, the value of U^* will be positive in all cases. The voltage equivalent of thermodynamic factor increases with higher absolute value of ΔG_f° and narrower phase stability regime Δx_B^{max} . This means that the slope of ΔG^M becomes steeper with higher U^* . Therefore, for even a small extent of unmixing to occur, a large amount of energy input or driving force is required, i.e. the restorative force is large.

Let us take the experiments and put it through the theory. For NiTiO_3 at 1300°C , the phase stability limit was given from the EPMA analysis as $x_B = 0.482 \pm 0.006$ and $x_B = 0.524 \pm 0.006$, giving the stability regime width as $\Delta x_B^{\text{max}} \geq 0.042 \pm 0.012$. With the Gibbs free energy of formation value of $-8,502 \text{ J/mol}$ [110], the voltage equivalent of thermodynamic factor for the system of NiTiO_3 is calculated according to eq. (4-63) as

$$U^* \leq 1.1 \text{ V}, \quad (4-79)$$

which means that the electric field we apply to is decreased by a factor of c.a. 1.1.

For BaTiO_3 , $\Delta G_f^{\circ} = -146,187 \text{ J/mol}$ [111] and $\Delta x_B^{\text{max}} = 0.003$ at 1500 K , so the voltage equivalent of thermodynamic factor is

$$U^*=250 \text{ V.}$$

(4-80)

This indicates that in order to achieve the same extent of unmixing in NiTiO_3 and BaTiO_3 , one must input c.a. 250 times more driving force for BaTiO_3 . In other words, it becomes much harder to observe the same amount of kinetic unmixing, provided that the diffusion coefficient ratio of BaTiO_3 and NiTiO_3 are similar. It was mentioned at the beginning of this section that the cations Ba and Ti may have equal electrochemical mobilities, but as no information is available for the diffusion coefficients of Ba and Ti in BaTiO_3 another feasible possibility for such behavior of BaTiO_3 , which is the thermodynamic factor or the voltage equivalent U^* . From thermodynamic principles it has been shown that, assuming the diffusion coefficient ratio to be similar, unmixing would become extremely hard to observe with increasing U^* , which is the case for BaTiO_3 .

To summarize this Chapter, the following have been done: (i) theoretical derivation of critical Po_2 ratio, according to Schmalzried, which is used as a reference work, (ii) novel theoretical derivation of critical decomposition voltage U_d , (iii) comparison of experimental results obtained from NiTiO_3 with theoretical expectations, therefore confirming the theory, and (iv) possible reasons for the behavior of BaTiO_3 besides the electrochemical mobilities being equal (in which we have no experimental proof on), with emphasis on the thermodynamic factor of the system.

5. The effect of electric field on formation reaction

(1) The literature on electric field and formation reaction

Electric field, as the most abundant driving force we have in our surroundings, affects all kinds of solid state reactions, either as the primary driving force or secondary driving force. In Chapters 2 to 4, kinetic unmixing and decomposition under electric field had been thoroughly discussed. Electric field, however, does not only affect unmixing and decomposition of a material. It can also alter the kinetics of formation reaction, which is the inverse reaction of decomposition. This aspect is discussed in this Chapter.

A formation reaction without electric field as the secondary driving force proceeds in a parabolic manner under steady state, as shown in Chapter 4. The driving force for such reaction is the chemical potential gradient of the reacting species (such as the end members AO_x - BO_y). The reaction is a purely diffusion-driven reaction. When electric field is applied, the two driving forces act constructively or destructively, depending on the direction of the electric field. This is similar to kinetic unmixing and decomposition, where there also are two acting driving forces. However, in case of kinetic unmixing and decomposition, the two driving forces act destructively, as the diffusion driving force tends to annihilate the concentration gradient built up by electric field.

There are a few literatures concerning the effect of electric field on the formation of oxides. Mackenzie et al. in their series article reported the result of interdiffusion under electric field for $CaO-Al_2O_3$ and $MgO-Al_2O_3$. The first article[168] dealt with powder mixture of $3CaO:Al_2O_3$. The powder mixture was put under electric field with field strength of zero to 1.0×10^5 V/m. Various phases were produced: C_5A_3 , C_3A , $C_{12}A_7$, CA_2 , CA and CA_6 (C: CaO and A: Al_2O_3). An interesting point was that the intensity of phases measured by x-ray diffraction was higher at the (+) side than at the (-) side, for all phases. However, it seems that the powder specimen

was not sintered or packed, meaning that while exposed to electric field at high temperatures there would be continuous grain growth and shrinkage, i.e. the microstructure is not stable. Nevertheless, they speculated that the incorporation of Ca ion into Al_2O_3 is enhanced where the Ca-containing component is more positive than the aluminum component. However, no evidence that such is the case is given in the article.

Their second article[169] reported the results of formation reactions in polycrystalline $\text{CaO-Al}_2\text{O}_3$ pellets. A typical elemental scan result of the reaction zone is given in Fig. 5-1. The configuration $(-)\text{CaO-Al}_2\text{O}_3(+)$ showed reduced reaction zone while $(+)\text{CaO-Al}_2\text{O}_3(-)$ showed increased reaction zone. An unexpected observation is that the unelectrolyzed (zero field) sample showed a greater degree of diffusion compared to the electrolyzed ones, even the configuration $(+)\text{CaO-Al}_2\text{O}_3(-)$. The authors proposed that a greater degree of sintering occurred due to the electric field, which would decrease the density of grain boundaries and therefore the grain boundary diffusion, which is suggested to play an important role in the interdiffusion of $\text{CaO-Al}_2\text{O}_3$ [170]. The thickness according to polarity suggests that Ca is faster than Al in the reaction zone, which according to x-ray diffraction is consisted of various phases such as C_5A_3 , C_{12}A_7 , CA_6 , CA and CA_2 . The distribution of the phases also follows the tendency of the overall thickness, i.e. the individual phases are detected in a wider regime when the polarity is set as $(+)\text{CaO-Al}_2\text{O}_3(-)$ compared to the $(-)\text{CaO-Al}_2\text{O}_3(+)$ case.

Their third article[171] was analogous to the second article, except that the material system was changed to $\text{MgO-Al}_2\text{O}_3$, which would be easier for analysis since there is only one intermediate compound, compared to the $\text{CaO-Al}_2\text{O}_3$ system which has numerous intermediate phases. Mg was found to be the dominant diffusing species, and the penetration depth was the deepest for $(+)\text{MgO-Al}_2\text{O}_3(-)$ case and the thinnest for unelectrolyzed case, as shown in Fig. 5-2. However, this result seems to be questionable. Assuming that the diffusion of Mg is dominant, the migration of

Mg will be inhibited when the polarity is set as (-)MgO-Al₂O₃(+), meaning that the penetration depth should be the thinnest for this case, rather than the unelectrolyzed case. This aspect was not discussed in the article.

After Mackenzie et al., Johnson et al. provided research on the spinels MgFe₂O₄[172,173] and MgIn₂O₄[124]. Johnson et al. deposited iron oxide film on bulk MgO substrate by pulsed laser deposition to the thickness of approximately 600 nm. Thin film geometry was used to exclude the complexities arising from the polycrystalline samples used by Mackenzie et al. The galvanic cell was set up in the configuration (-)Fe₂O₃-MgO(+). The result under electric field shows that the spinel phase MgFe₂O₄ is formed, but also another MgO layer is formed on the opposite surface of MgFe₂O₄. This is because the divalent Mg ions are driven past the spinel layer to combine with oxygen to form MgO. For comparison an identical film substrate without electric field was put under equivalent thermal annealing. The comparison between the two cells show that the thickness of MgFe₂O₄ spinel was thicker under electric field and that the extra formation of MgO on the opposite surface happened only under electric field. However, no result was reported for the case where the polarity is set in the reverse direction, and no quantitative data were given in terms of thickness.

The experiment for MgIn₂O₄ was done in a similar manner. Pulsed laser deposition was used to deposit MgIn₂O₄ and In₂O₃ films on single crystal MgO substrate, with the resulting thin films approximately 1.5 μm in thickness. The diffusion couples were placed between platinum electrodes, with the configuration (+)MgO-MgIn₂O₄-In₂O₃(-). A control diffusion couple was also prepared, without electric field. The effect of electric field was that mass transport toward the (-) electrode occurred, moving the original interface into the MgO substrate (this is shown by the movement of inert platinum markers). In this article the thickness of the resultant spinel layers did not differ greatly, with or without electric field. This seems to be because of the short reaction time (0.2 hours), which seems to be too

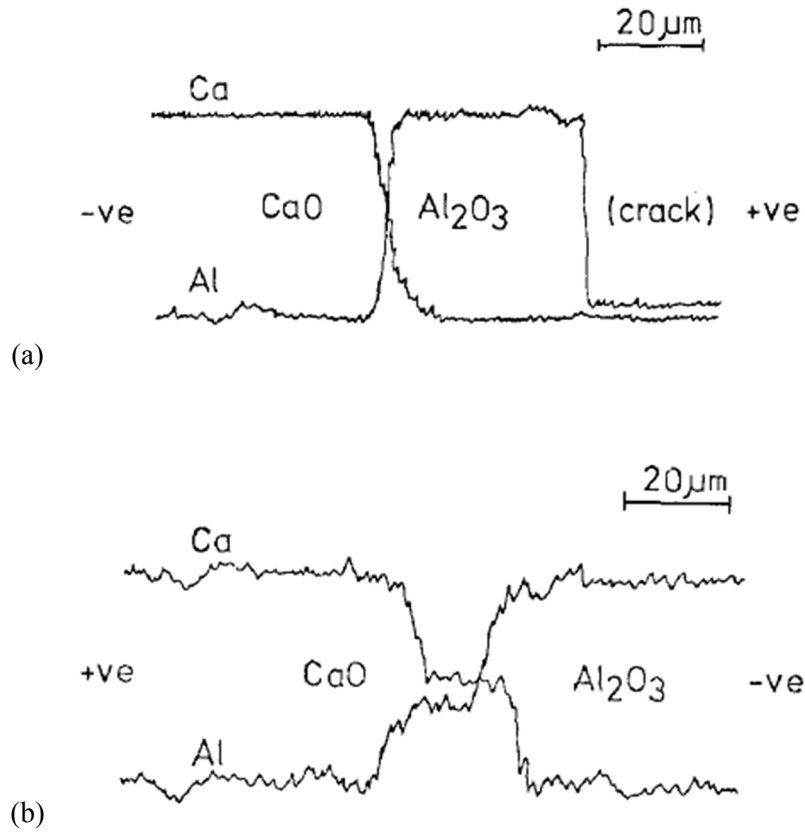
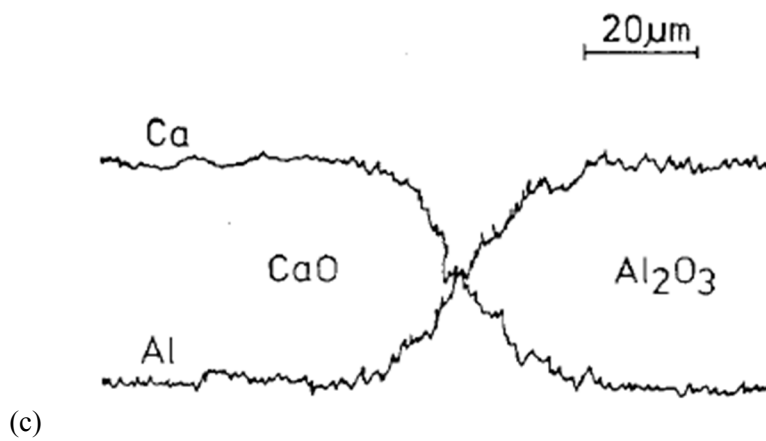


Fig. 5-1. The elemental line scans across the reactions zone of CaO-Al₂O₃ diffusion couples, (a) (-)CaO-Al₂O₃(+), (b) (+)CaO-Al₂O₃(-) and (c) unelectrolyzed, reacted at 1250°C for 4 hours under electric field of 6.0×10^4 V/m. From Mackenzie et al. [169] (continued in the next page)



(continued) Fig. 5-1. The elemental line scans across the reactions zone of CaO-Al₂O₃ diffusion couples, (a) (-)CaO-Al₂O₃(+), (b) (+)CaO-Al₂O₃(-) and (c) unelectrolyzed, reacted at 1250°C for 4 hours under electric field of 6.0×10^4 V/m. From Mackenzie et al. [169]

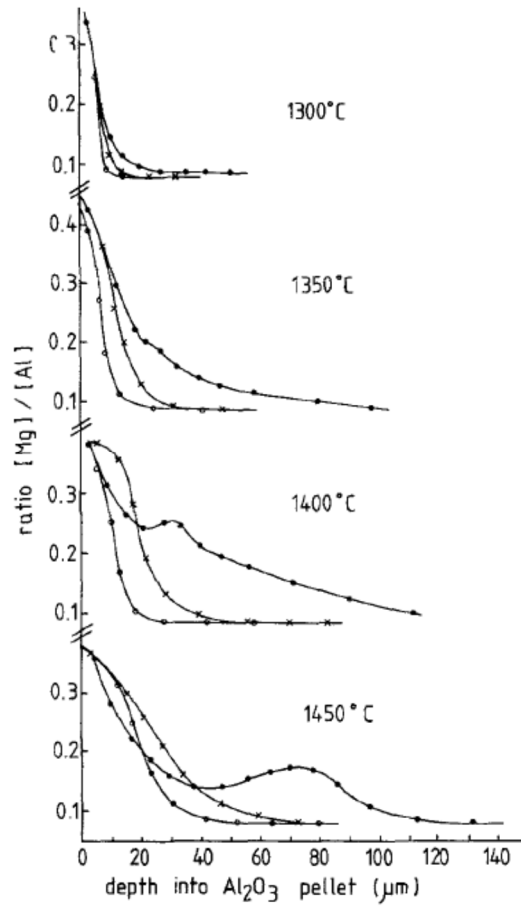


Fig. 5-2. Diffusion profiles of Mg in electrolyzed and unelectrolyzed MgO/Al₂O₃ couples at various temperatures, annealed for 48 hours with mean electric field strength of 4.93×10^4 V/m. -○-: unelectrolyzed, -×-: (-)MgO-Al₂O₃(+), -●-: (+)MgO-Al₂O₃(-). From Mackenzie et al. [171]

short to show any meaningful difference in formation kinetics. Again, only one polarity was examined (the polarity which accelerates the faster cation species); the opposite case was not discussed.

A more theoretical and thorough analysis of effect of electric field on formation reaction was done by Korte et al.[125,174,175], also for the system MgO-In₂O₃. A theoretical derivation of the layer growth under electric field is provided (will be given in the next section) along with the microstructure evolution arising from large angle boundaries. The experimental results of growth under electric field and without electric field is as shown in Fig. 5-3. The thickness results under electric field had large errors, due to the unstable microstructure. Again only one polarity is discussed ((+)MgO-In₂O₃(-)).

The literature up to now lack theoretical treatment, with the exception of Korte et al. Also, the analysis for both polarities have not been done. Thus, in this Chapter the objective is to setup a master equation that governs the growth kinetics under electric field (this had been done by Korte et al.) and confirm that the equation is feasible through comparison with the experimental results. Also, the displacement of platinum markers under electric field is described qualitatively.

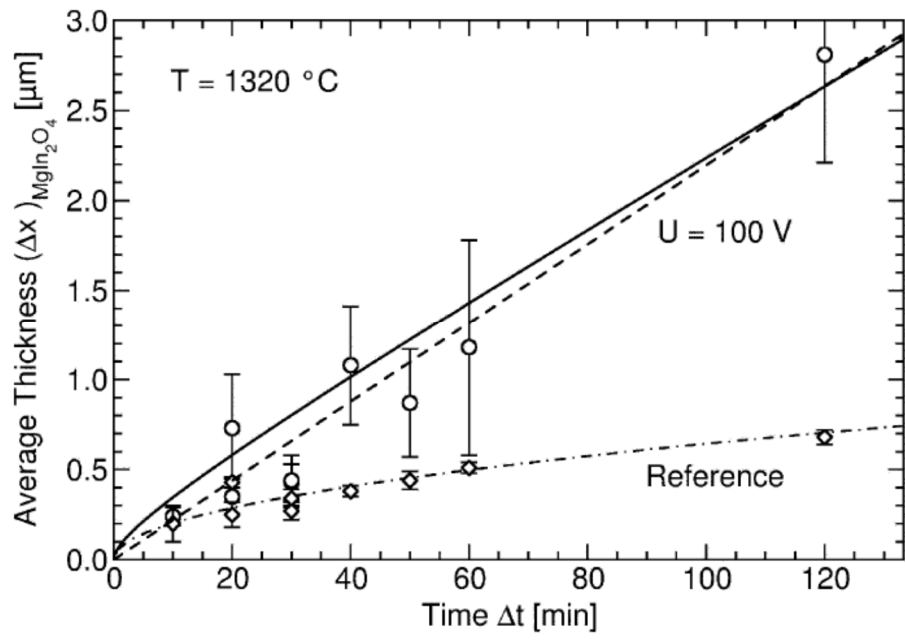


Fig. 5-3. The thickness of the spinel layer as a function of time. From Korte et al. [175]

(2) Theoretical derivation of formation kinetics under electric field

Let us derive the master equation for formation kinetics under electric field. This had been done by Korte et al. and is presented here, with slight modifications and assumptions to fit for the system in hand. The following assumptions are made: (i) local equilibrium prevails, (ii) virtually constant transference numbers in the phase ABO_3 , (iii) the compound ABO_3 is a semiconductor and (iv) the electrodes are reversible for oxygen.

The close-circuit condition is given as

$$\sum_k i_k = i_{\text{appl}} = -\frac{\sigma_A}{2F} \nabla \eta_{A^{2+}} - \frac{\sigma_B}{4F} \nabla \eta_{B^{4+}} + \frac{\sigma_e}{F} \nabla \eta_e. \quad (5-1)$$

The oxygen component is neglected here. By local equilibrium, $\nabla \eta_{A^{2+}} = \nabla \mu_A - 2\nabla \eta_e = \nabla \mu_{AO} - 2\nabla \eta_e$, $\nabla \eta_{B^{4+}} = \nabla \mu_B - 4\nabla \eta_e = \nabla \mu_{BO_2} - 4\nabla \eta_e$ and by Gibbs-Duhem equation $\nabla \mu_{AO} + \nabla \mu_{BO_2} = \nabla \mu_{ABO_3} \approx 0$. Therefore eq. (5-1) can be modified to

$$\nabla \eta_e = \frac{t_A}{2} \nabla \mu_{AO} + \frac{t_B}{4} \nabla \mu_{BO_2} + \frac{i_{\text{appl}} F}{\sigma_{\text{tot}}}. \quad (5-2)$$

The flux of ions, from the definition $j_k = -\frac{D_k c_k}{RT} \nabla \eta_k$, after applying local equilibrium and eq. (5-2), can be written as

$$j_{A^{2+}} = j_A = -\frac{D_A c_A}{RT} \left(1 - t_A + \frac{1}{2} t_B \right) \nabla \mu_{AO} + \frac{t_A}{2F} i_{\text{appl}}, \quad (5-3a)$$

$$j_{B^{4+}} = j_B = -\frac{D_B c_B}{RT} (1 - t_B + 2t_A) \nabla \mu_{\text{BO}_2} + \frac{t_B}{4F} i_{\text{appl}}. \quad (5-3b)$$

The terms in the parentheses can be assumed as unity, since the compound is a semiconductor. The total flux of ABO_3 , j_{ABO_3} , is defined as $j_A - j_B$, which gives

$$\begin{aligned} j_{\text{ABO}_3} &= j_A - j_B = \frac{D_A c_A}{RT} \nabla \mu_{\text{BO}_2} + \frac{t_A}{2F} i_{\text{appl}} + \frac{D_B c_B}{RT} \nabla \mu_{\text{BO}_2} - \frac{t_B}{4F} i_{\text{appl}} \\ &= \frac{D_A c_A + D_B c_B}{RT} \nabla \mu_{\text{BO}_2} + \left(\frac{t_A}{2} - \frac{t_B}{4} \right) \frac{i_{\text{appl}}}{F}. \end{aligned} \quad (5-4)$$

By steady state assumption, $\nabla \mu_{\text{BO}_2} \approx -\Delta G_f^\circ / \Delta x$, and eq. (5-4) is rewritten as

$$j_{\text{ABO}_3} = \frac{d\Delta x}{V_m dt} = -\frac{D_A c_A + D_B c_B}{RT} \frac{\Delta G_f^\circ}{\Delta x} + \left(\frac{t_A}{2} - \frac{t_B}{4} \right) \frac{i_{\text{appl}}}{F}. \quad (5-5)$$

Let us compare eq. (5-5) with eq. (4-44). The only difference is the last term on the right-hand side in eq. (5-5) which corresponds to the external constant current. The solving of eq. (5-5), however, gives a different result from eq. (4-44) because of that very term. Eq. (5-5) can be rewritten to separate the variables as

$$\frac{d\Delta x}{-\frac{D_A + D_B}{RT} \frac{\Delta G_f^\circ}{\Delta x} + \left(\frac{t_A}{2} - \frac{t_B}{4} \right) \frac{i_{\text{appl}} V_m}{F}} = \frac{d\Delta x}{\frac{k_p}{\Delta x} + k_{\text{elf}}} = dt \quad (5-6)$$

where k_p is the parabolic rate constant defined as in eq. (4-30) and k_{elf} the newly introduced electric field term defined as

$$k_{\text{elf}} = \left(\frac{t_A}{2} - \frac{t_B}{4} \right) \frac{i_{\text{appl}} V_m}{F}. \quad (5-7)$$

One should note that the electric field term is expressed as the difference of the cation transference numbers (and therefore diffusion coefficients). This signifies that, the applied electric field will enhance the motion of one cation species but will reduce the motion of the other species. This is because the cations have same polarity. The integration of eq. (5-6) is done by using the integral relation

$$\int \frac{dz}{A/z+B} = \frac{Bz - A \ln(A+Bz)}{B^2} \quad (5-8)$$

and results in the following equation, which is the master equation for growth under electric field:

$$t = \frac{\Delta x}{k_{\text{elf}}} - \frac{k_p}{k_{\text{elf}}^2} \ln \frac{k_p + k_{\text{elf}} \Delta x}{k_p} \quad (5-9)$$

Instead of the form $\Delta x = \Delta x(t)$ the resulting equation is in the inverse function form $t = t(\Delta x)$. Eq. (5-9) consists of two terms, a linear term $\Delta x / k_{\text{elf}}$ and a logarithmic term $\frac{k_p}{k_{\text{elf}}^2} \ln \frac{k_p + k_{\text{elf}} \Delta x}{k_p}$. The linear term corresponds to a direct electric field effect and reflects Faraday's law, which states that the amount of reaction product is proportional to the flown charge, or $n \propto It$ (n : number of moles of product, I : constant current, t : time). The logarithmic term represents a combination of diffusion and electric field contribution.

When the applied electric field approaches zero ($k_{\text{elf}} \rightarrow 0$), eq. (5-9) should become the parabolic rate law $(\Delta x)^2 = 2k_p t$. This is done by using the Taylor series for natural logarithm, as in eq. (4-61), $\ln(1+z) \approx z - \frac{1}{2}z^2 + \frac{1}{3}z^3 \mp \dots$ while

setting $z = k_{\text{elf}}\Delta x / k_p$. As $k_{\text{elf}} \rightarrow 0$, $z \rightarrow 0$ so the logarithm can be approximated as

$$\frac{k_p}{k_{\text{elf}}^2} \ln \frac{k_p + k_{\text{elf}}\Delta x}{k_p} = \frac{\Delta x}{k_{\text{elf}}} - \frac{1}{2} \frac{(\Delta x)^2}{k_p}. \quad (5-10)$$

Inserting eq. (5-10) into eq. (5-9) yields the parabolic rate law. At the beginning of the formation reaction, the effect of diffusion is dominant because the concentration gradient at the boundary is theoretically infinity. As time passes the diffusion driving force is decreased with increasing layer thickness, while the effect of electric field is held constant and therefore the growth by electric field dominates at longer durations (according to Korte et al, when $\Delta x \geq 36k_p / k_{\text{elf}}$ eq. (5-9) can be approximated by linear rate law with errors less than 10%).

The effect of applied electric field can be qualitatively explained as follows. When the electric field is applied (+)AO_x-BO_y(-), the A cations will be driven by the field while the migration of B cations toward AO_x will be reduced compared to the zero field case. If the A cations are the faster species, this would lead to thicker layer of ABO_{x+y}, as the faster species are more accelerated. If the field direction is reversed to (-)AO_x-BO_y(+), the faster species A is hindered. Although the migration of B cations toward AO_x will be enhanced, the migration of A cations toward BO_y, which has larger effect, will be reduced more than the enhancement of the motion of B cations, therefore reducing the layer thickness of ABO_{x+y}. Therefore, generally, with $D_A > D_B$, the layer thickness of ABO_{x+y} will be in the order of (+)AO_x-BO_y(-) > zero field > (-)AO_x-BO_y(+). This is schematically shown in Fig. 5-4.

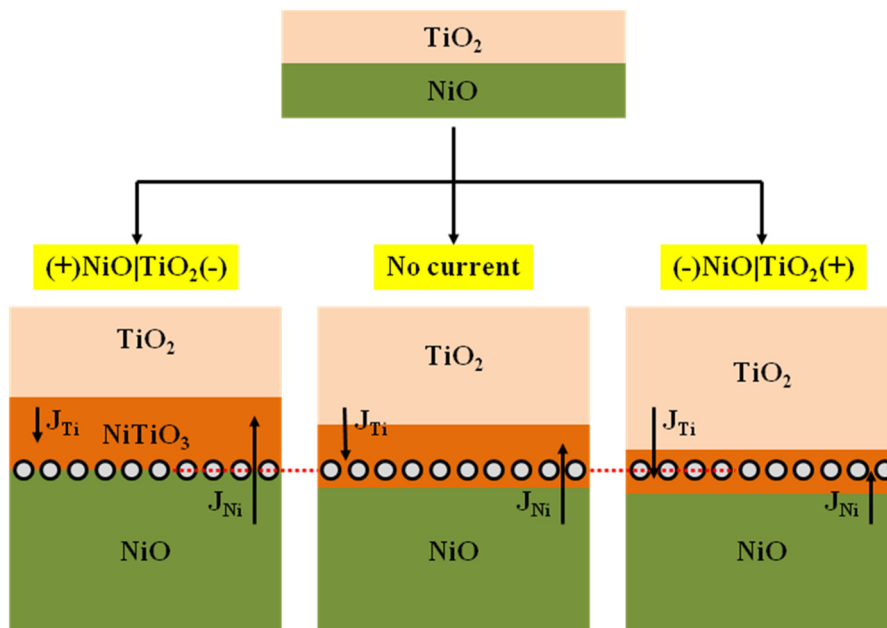


Fig. 5-4. Schematic diagram of how the layer thickness will be affected by electric field, with $A=\text{Ni}$ and $B=\text{Ti}$, drawn for $D_{\text{Ni}} > D_{\text{Ti}}$. The circles represent inert markers.

(3) Experimental results and discussion

The experimental setup was the same as previously mentioned in Chapter 3. Electric field was applied to the whole setup shown in Fig. 3-10 (b) by means of a galvanostat. A constant current of 0.4 A and other magnitudes was applied for three different cases: (i) no current, (ii) (+)NiO-TiO₂(-) and (iii) (-)NiO-TiO₂(+). As soon as the current was passed for a desired duration at 1300°C, the current was turned off and the cell was taken out of the furnace immediately and quenched in air. The analysis was done by XRD and SEM.

Fig. 5-5 shows Fig. 3-21 (a), which showed the formation reaction result for the case with no current, along with the cases with applied electric current. In Chapters 3 and 4 it was shown that $\Delta x_B < \Delta x_A$ and therefore $D_B < D_A$, so that Ni is the faster diffusing species in NiTiO₃. According to our expectations, the NiTiO₃ layer thickness would then be in the order of (+)NiO-TiO₂(-) > zero field > (-)NiO-TiO₂(+). Fig. 5-6 shows that this is indeed true. Although not visible in the SEM images, the platinum inert markers were found to be completely shifted to the NiO/NiTiO₃ boundary, again signifying the enhancement in migration of Ni.

Typical microstructure of the (+)NiO-TiO₂(-)case is shown in Fig. 5-6. One can immediately notice that the microstructure in this case is not stable and that the formed NiTiO₃ layer seems even porous. Due to these microstructure roughness, it was difficult to exactly measure the thickness of the layer with high precision, which is reflected by the large error values in Fig. 5-5. The porosity of the layer suggests that the measured thickness may be overestimated. Although it was not stated, the theoretical analysis provided in the previous section deals with layers that are practically fully dense. If the formed layer is as porous as those shown in Fig. 5-6, when the layer is compacted to nearly 100% density, the layer would be thinner. Such porous nature seems to come from the excessive transport of Ni, wherein the lattice becomes unstable due to the excessive transport. This seems to

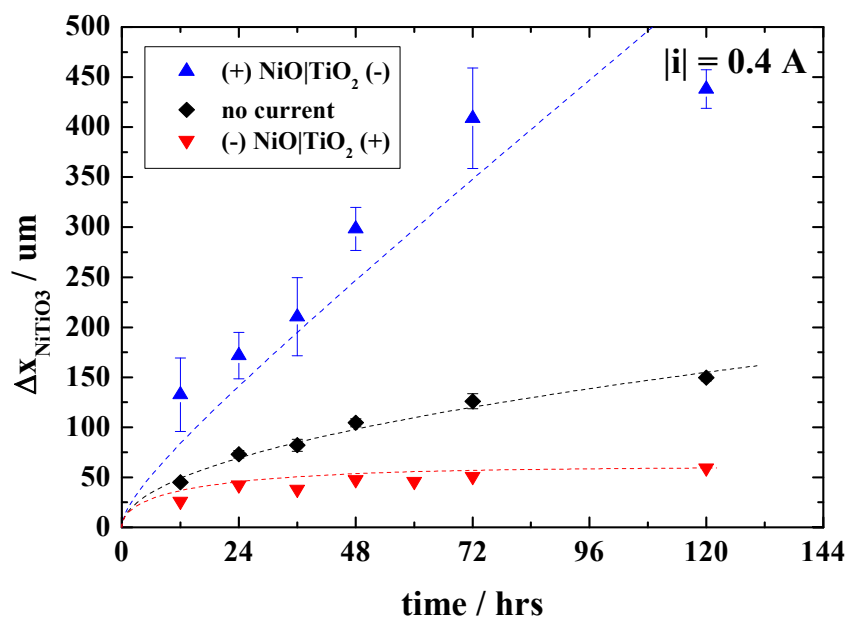


Fig. 5-5. The thickness of the formed NiTiO₃ layer according to the polarity as function of time. The "no current" case is equivalent to Fig. 3-21 (a). The dotted lines are best fit to eq. (5-9).

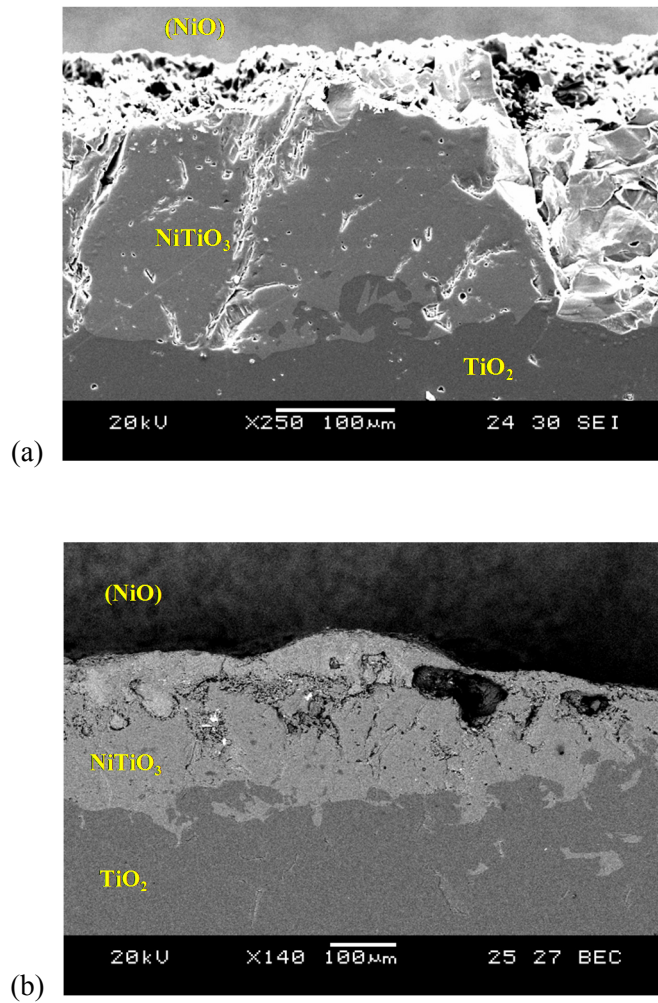


Fig. 5-6. Microstructure of the NiTiO_3 layer after formation under constant current of 0.4 A in the configuration (+)NiO-TiO₂(-) (a) for 24 hours and (b) for 12 hours at 1300°C. The NiO pellet fell off spontaneously and therefore is written in parentheses. One can see that the microstructure is very rough.

be related to the anomalous voltage behavior shown in Fig. 5-7. The voltage was measured in a semi-4 probe configuration. An abrupt voltage plateau appears for all cases, lasting for c.a. 20 to 30 ks. This can be qualitatively explained to be due to pore or cavity formation by excessive Ni transport, as the resistance of the whole setup increases to about five times.

The microstructure of the opposite case (-)NiO-TiO₂(+) is shown in Fig. 5-8. Unlike the other two cases, in this case the NiO pellet did not spontaneously fall off and stayed intact. Two characteristic features can be found. The first is that the platinum inert markers which represent the original interface are shifted toward TiO₂, meaning that the migration of Ti exceeded that of Ni. This of course is because the electric field enhanced the movement of Ti while the movement of Ni is reduced.

The second characteristic is the formation of channels in the NiO pellet, which was not observed for the (+)NiO-TiO₂(-) case. This seems to be due to the migration and pile-up of cation vacancies at the NiTiO₃/TiO₂ interface. TiO₂ is known to have titanium interstitials as majority cation defects[176], while NiTiO₃ and NiO[177] both have cation vacancies as majority cation defects. When the electric field is applied as (-)NiO-TiO₂(+) the cation vacancies will migrate toward TiO₂. Since TiO₂ cannot incorporate these vacancies they pile up and eventually grow along the grain boundaries like pinholes toward the (-) electrode. This is schematically expressed in Fig. 5-10.

The voltage-time plot under constant current for the case (-)NiO-TiO₂(+) does not show any anomalous behavior as for (+)NiO-TiO₂(-). After an initial jump, the voltage continuously decreases. The decreasing tendency is correct, as the total conductivity of TiO₂ is much larger than those of NiO and NiTiO₃. As the volume percent of TiO₂ decreases, it is natural for the total resistance to decrease.

Let us return to Fig. 5-5. The dotted lines in Fig. 5-5 are the best fitted results to eq. (5-9). The fitting parameters were k_p and k_{elf} and the results are shown in Table 5-1. Looking at the table, one can notice that the magnitude of k_{elf} for the two field-driven cases is different. Eq. (5-7) states that the value of k_{elf} depends on the applied current, which is equal for the two cases. Therefore, theoretically the k_{elf} values obtained from the two cases should have the same magnitude but opposite polarity. It should be noted that the microstructure of the (+)NiO-TiO₂(-) case was unstable and porous, while that of the (-)NiO-TiO₂(+) case was stable and fully dense. Therefore, the k_{elf} value obtained for the (+)NiO-TiO₂ case may be overestimated. Also, for the (-)NiO-TiO₂(+) case, when steady state is reached the thickness of the formed layer is given by setting eq. (5-5) to be zero, i.e.

$$\frac{d\Delta x}{dt} = \frac{k_p}{\Delta x} + k_{\text{elf}} = 0, \quad \Delta x = -\frac{k_p}{k_{\text{elf}}} \quad (5-11)$$

The steady state layer thickness is calculated as (61 ± 2) μm , which in accordance with the data points in Fig. 5-6 at 120 hours, (59.4 ± 1.4) μm . This gives more proof that the value $|k_{\text{elf}}| = (4.61 \pm 0.06) \times 10^{-8}$ cm/s is more feasible than $(1.08 \pm 0.14) \times 10^{-7}$ cm/s .

The displacement of inert platinum markers is an interesting case. Fig. 5-10 shows the relative placement of the inert markers as function of applied electric current at 72 hours. The definition of Δx_A and Δx_B is as shown in Fig. 4-4. The layer thickness is the highest for the (+)NiO-TiO₂(-) case and the thinnest for the (-)NiO-TiO₂(+) case. However, above a certain current magnitude, the layer thickness again grows, as the thickness for $I = -1.0$ A is larger than that of $I = -0.2$ or -0.4 A. This is, as stated before, due to the Ti migration which is enhanced by the electric field. The inert markers are practically on the NiO/NiTiO₃ interface for the (+)NiO-TiO₂(-) case, but shifts toward the NiTiO₃/TiO₂ interface with increasing current in

the (-)NiO-TiO₂(+) direction, to such extent that the Ti migration becomes larger than the Ni migration. Qualitative explanation is possible as above. The mathematical expression for the behavior of inert markers is not yet complete and will be presented in the future.

From the results presented, it is clear that the external electric field, which acts as secondary driving force in the formation reaction, affects solid state formation reaction greatly, both in terms of microstructure and thickness. The density of the layer can be controlled, along with the microstructure and even the porosity, by electric field. Certainly, the extent of such effects will be decided by the properties of the material, but nonetheless these results could be applied usefully i.e. when one wishes to obtain porous structures (for example, porous solid oxide fuel cell cathodes may be obtainable by this method).

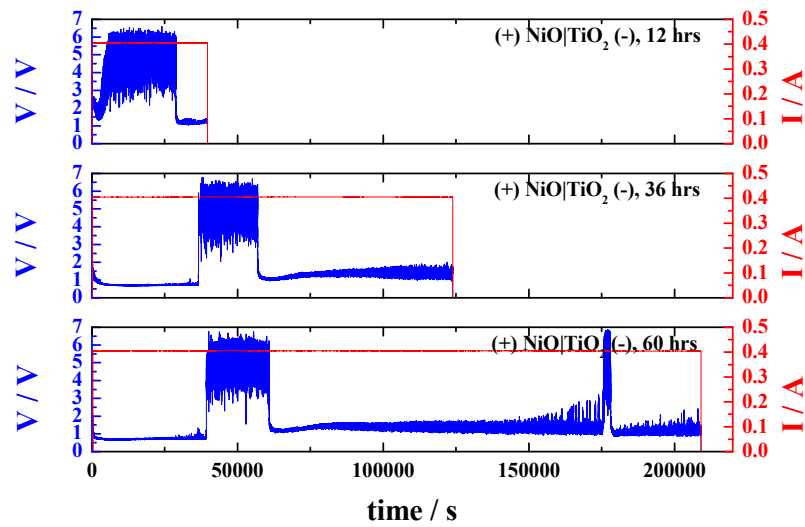
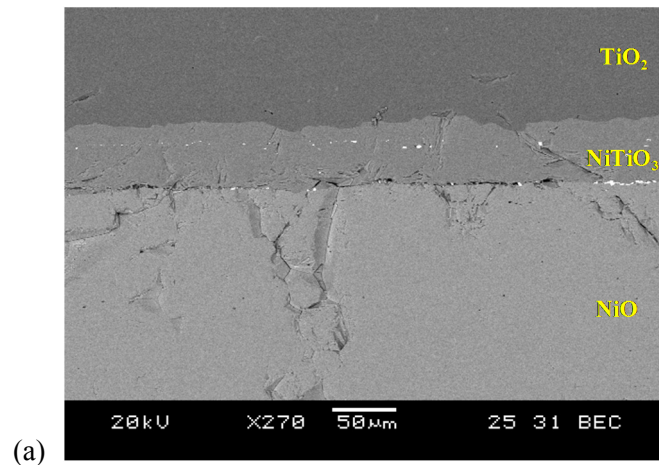
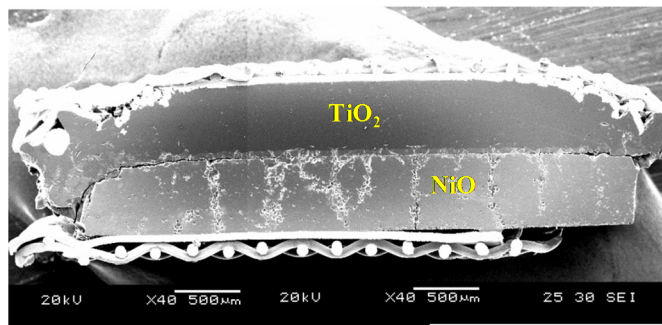


Fig. 5-7. The voltage-time plot under constant current of 0.4 A at 1300°C, for durations of 12, 36 and 60 hours in the configuration (+)NiO-TiO₂(-). All cases show an abrupt increase in the voltage lasting for about 20~30 ks.



(a)



(b)

Fig. 5-8. Microstructure of the NiTiO_3 layer after formation under constant current of 0.4 A in the configuration (-)NiO-TiO₂(+) for 48 hours, with (a) the enlarged view of the reaction zone and (b) the overall specimen. The NiO pellet was intact. The white particles in NiTiO_3 shown in (a) are platinum inert markers.

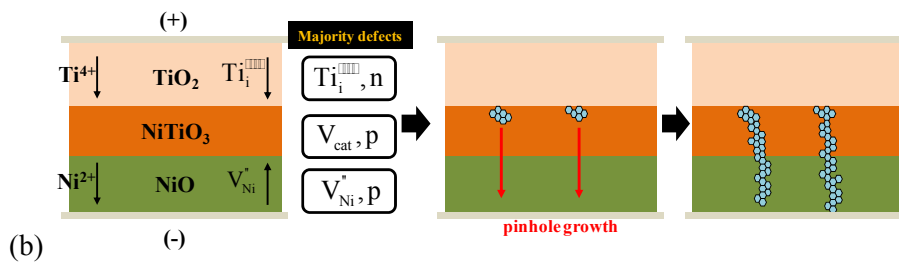
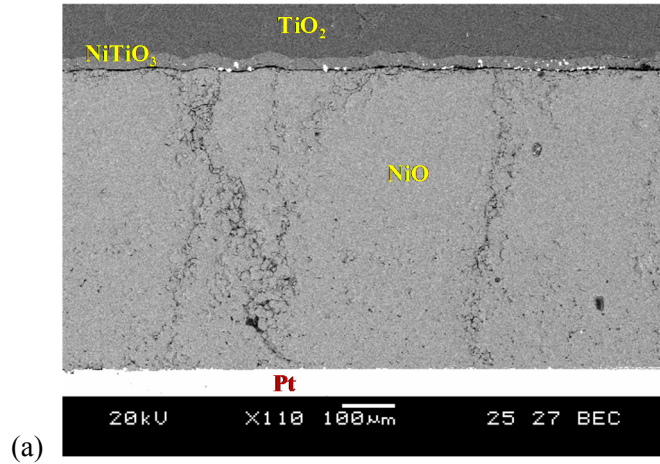


Fig. 5-9. (a) Enlarged view of the channels formed, (b) schematic illustration of the formation of vacancy channels or pinholes in NiTiO₃ and NiO for the configuration (-)NiO-TiO₂(+). The cation vacancies pile up at the NiTiO₃/TiO₂ boundary, then grow along the grain boundaries.

	(+)NiO-TiO ₂ (-)	zero field	(-)NiO-TiO ₂ (+)
$k_p / \text{cm}^2/\text{s}$	$(2.81 \pm 0.11) \times 10^{-10}$		
$k_{\text{elf}} / \text{cm}/\text{s}$	$(1.08 \pm 0.14) \times 10^{-7}$	-	$-(4.61 \pm 0.06) \times 10^{-8}$

Table 5-1. The fitted parameters according to eq. (5-9) for the data points shown in Fig. 5-6. It should be noted that the k_{elf} value for (+)NiO-TiO₂(-) may be overestimated.

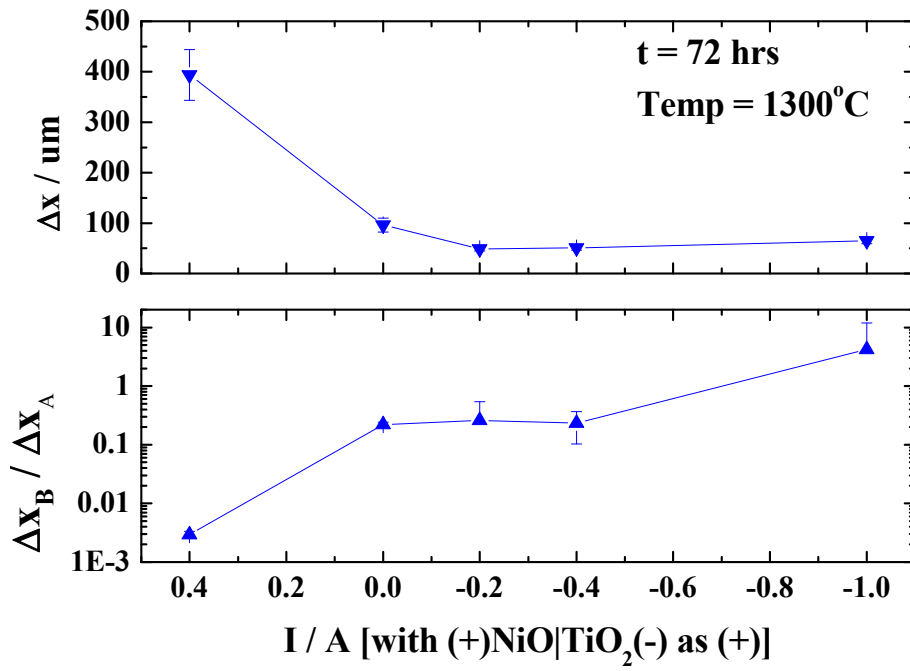


Fig. 5-10. The total layer thickness (top) and the placement of platinum inert markers (bottom) for NiO-TiO₂ diffusion couple at 1300°C for 72 hours.

6. Summary and future work

In this thesis, the effect of electric field on the degradative phenomena and formation reaction have been discussed. For the degradative phenomena of kinetic unmixing and decomposition, whereas numerous results were seen under P_{O_2} gradient, very few works were done with electric field as driving force. Especially, no work on the kinetic decomposition under electric field was found. Therefore, this thesis was done to set up a master equation that governs kinetic decomposition under electric field and confirming the equation. Afterwards, the effect of electric field on formation reaction was accounted for.

To do this, the basic principles of kinetic unmixing and decomposition were given, followed by a thorough survey of the literature up to now concerning kinetic unmixing and decomposition, in Chapter 2. The numerical works were only slightly mentioned as they are not the main point in this thesis. A model system of $NiTiO_3$ was selected due to the simplicity of phase diagram and low value of formation free energy. In Chapter 3, kinetic unmixing and decomposition was performed on $NiTiO_3$ pellets galvanostatically at $1300^\circ C$ in air. To convert the applied constant current into applied voltage the total conductivity of the system was first measured.

Various magnitudes of driving force were applied to the $NiTiO_3$ pellets. For all specimens electrotransport was confirmed by the anode carving into the specimen and novel matrix forming at the cathode. For specimens below a certain threshold driving force, only kinetic unmixing occurred according to the EPMA profile analysis. However, above this threshold driving force both unmixing and decomposition occurred. A jump in concentration profile was observed at the electrode vicinities to the ratio of $Ti/Ni=500$ at the anode and $Ti/Ni=0.1$ at the cathode. The concentration profiles were in agreement with the previously reported

results by Schmalzried and Laqua under P_{O_2} gradient. Also, XRD of the electrodes showed small but detectable amount of TiO_2 at the anode and NiO at the cathode.

In Chapter 4, the master equation for kinetic decomposition was derived from two conditions: (i) steady state and (ii) closed-circuit condition. From the master equation it became evident that the diffusion coefficient ratio of cations A and B is the critical factor in determining the threshold voltage for decomposition, U_d . To measure this ratio, solid state reaction of $NiO-TiO_2$ was done, and with Pt inert markers the diffusion coefficient ratio was obtained as $D_B/D_A=0.21\pm 0.07$. The diffusion coefficient ratio was inserted into the master equation. The experimentally obtained range of U_d (97~120 mV) and the theoretically expected U_d (69~128 mV) coincided within the error bounds. Also, the possible reasons for the un-unmixing and un-decomposing nature of $BaTiO_3$ were proposed, based on the thermodynamic factor of the system.

Chapter 5 showed the effect of electric field on the formation reaction. The master equation was derived by Korte et al., but experimental confirmation was not given. Therefore in this thesis quantitative analysis of the formation kinetics under electric field and microstructure characteristics were introduced. It was shown that the thickness and microstructure of the system is greatly affected by electric field, which can be used in industries.

For future work, reconfirmation of the decomposition voltage U_d should be done for other systems. Especially, the perovskite materials are of interest because $BaTiO_3$ showed neither kinetic unmixing nor decomposition. Whether this characteristic is solely for $BaTiO_3$ or common for all perovskite materials should be confirmed with a perovskite system wherein the diffusion coefficient ratio can be readily obtained. Even if the system is not a perovskite material, reconfirmation would be needed to further legitimize the decomposition voltage. Additional work on the formation reaction also should be done in a more systematic way, so that

accurate estimation of the microstructure and thickness can be made. Also, application to industry, such as making porous structures for solid oxide fuel cell cathodes, is another part that can be taken into account.

Reference

- [1] J. -H. Park and R. N. Blumenthal, "Electronic transport in 8 mole percent Y_2O_3 - ZrO_2 ," *J. Electrochem. Soc.* **136** (1989) 2867-2876
- [2] S. -H. Park, "Tailoring of electrolytic domain of ceria-based electrolytes with electron traps," Ph. D thesis, Seoul National University, Seoul, Korea (2008)
- [3] N. Sakai, H. Yokokawa, T. Horita, K. Yamaji, "Lanthanum chromite-based interconnects as key materials for SOFC stack development," *Int. J. Appl. Ceram. Technol.* **1** (2004) 23-30
- [4] J. W. Stevenson, T. R. Armstrong, R. D. Carneim, L. R. Pederson, W. J. Weber, "Electrochemical properties of mixed conducting perovskites $\text{La}_{1-x}\text{M}_x\text{Co}_{1-y}\text{Fe}_y\text{O}_{3-\delta}$," *J. Electrochem. Soc.* **143** (1996) 2722-2729
- [5] H. Kamata, Y. Yonemura, J. Mizusaki, H. Tagawa, K. Naraya, T. Sasamoto, "High temperature electrical properties of the perovskite-type oxide $\text{La}_{1-x}\text{Sr}_x\text{MnO}_{3-\delta}$," *J. Phys. Chem. Solids* **56** (1995) 943-950
- [6] J. H. Kuo, H. U. Anderson, D. M. Sparlin, "Oxidation-reduction behavior of undoped and Sr-doped LaMnO_3 nonstoichiometry and defect structure," *J. Solid State Chem.* **83** (1989) 52-60
- [7] J. Mizusaki, H. Tagawa, K. Naraya, T. Sasamoto, "Nonstoichiometry and thermochemical stability of the perovskite-type $\text{La}_{1-x}\text{Sr}_x\text{MnO}_{3-\delta}$," *Solid State Ion.* **49** (1991) 111-118
- [8] H. -S. Kim, H. -I. Yoo, "Compilation of all isothermal mass/charge transport properties of mixed conducting $\text{La}_2\text{NiO}_{4+\delta}$ at elevated temperatures," *Phys. Chem. Chem. Phys.* **13** (2011) 4651-4658
- [9] S. A. Long, R. N. Blumenthal, "Ti-rich nonstoichiometric BaTiO_3 : II, Analysis of defect structure," *J. Am. Ceram. Soc.* **54** (1971) 577-583
- [10] A. M. J. H. Seuter, "Defect chemistry and electrical transport properties of barium titanate," *Phil. Res. Repts. Suppl.* **3** (1974) 1-84
- [11] C. -R. Song, H. -I. Yoo, "Chemical diffusivity of $\text{BaTiO}_{3-\delta}$: defect-chemical analysis," *Phys. Rev. B* **61** (2000) 3975-3982

- [12] Z. P. Shao, W. S. Yang, Y. Cong, H. Dong, J. H. Tong, G. X. Xiong, "Investigation of the permeation behavior and stability of a $\text{Ba}_{0.5}\text{Sr}_{0.5}\text{Co}_{0.8}\text{Fe}_{0.2}\text{O}_{3-\delta}$ oxygen membrane," *J. Membr. Sci.* **172** (2000) 177-188
- [13] T. Lee, H. -I. Yoo, "Partial conductivities and Onsager transport coefficient matrix of $\text{BaCo}_{0.7}\text{Fe}_{0.22}\text{Nb}_{0.08}\text{O}_{3-\delta}$," *Solid State Ion.* **241** (2013) 5-11
- [14] H. B. Chung, K. Shin, J. M. Lee, "Phase-change characteristics of chalcogenide $\text{Ge}_1\text{Se}_1\text{Te}_2$ thin films for use in nonvolatile memories," *J. Vac. Sci. Technol.* **A25** (2007) 48-53
- [15] R. Venkatasubramanian, E. Siivola, T. Colpitts, B. O'Quinn, "Thin-film thermoelectric devices with high room-temperature figures of merit," *Nature* **413** (2001) 597-602
- [16] T. Okuda, K. Nakanishi, S. Miyasaki, Y. Tokura, "Large thermoelectric response of metallic perovskites: $\text{Sr}_{1-x}\text{La}_x\text{TiO}_3$ ($0 < x < 0.1$)," *Phys. Rev. B* **65** (2001) 113104
- [17] H. Ohta, "Thermoelectrics based on strontium titanate," *Mater. Today* **10** (2007) 44-49
- [18] N. Keawprak, R. Tu, T. Goto, "Thermoelectric properties of alkaline earth ruthenates prepared by SPS," *Mater. Sci. Eng. B* **161** (2009) 71-75
- [19] L. Bocher, M. H. Aguirre, D. Logvinovich, A. Shkabko, R. Robert, M. Trottman, A. Weidenkaff, " $\text{CaMn}_{1-x}\text{Nb}_x\text{O}_3$ ($x \leq 0.08$) perovskite-type phases as promising new high-temperature n-type thermoelectric materials," *Inorg. Chem.* **47** (2008) 8077-8085
- [20] K. Fujita, T. Mochida, K. Nakamura, "High-temperature thermoelectric properties of $\text{Na}_x\text{CoO}_{2-\delta}$ single crystals," *Jpn. J. Appl. Phys.* **40** (2001) 4644-4647
- [21] I. Terasaki, Y. Sasago, K. Uchinokura, "Large thermoelectric power in NaCo_2O_4 single crystals," *Phys. Rev. B* **56** (1997) R12685
- [22] G. Xu, R. Funahashi, M. Shikano, I. Matsubara, Y. Zhou, "Thermoelectric properties of the Bi- and Na-substituted $\text{Ca}_3\text{Co}_4\text{O}_9$ system," *Appl. Phys. Lett.* **80** (2002) 3760-3763

- [23] H. Ledbetter, H. Ogi, N. Nakamura, "Elastic, anelastic, piezoelectric coefficients of monocrystal lithium niobate," *Mech. Mater.* **36** (2004) 941-947
- [24] S. Shao, J. Zhang, Z. Zhang, P. Zheng, M. Zhao, J. Li, C. Wang, "High piezoelectric properties and domain configuration in BaTiO₃ ceramics obtained through the solid-state reaction route," *J. Phys. D* **41** (2008) 125408
- [25] R. Guo, L. E. Cross, S. -E. Park, B. Noheda, D. E. Cox, G. Shirane, "Origin of the high piezoelectric response in PbZr_{1-x}Ti_xO₃," *Phys. Rev. Lett.* **84** (2000) 5423-5426
- [26] H. -I. Yoo, C. -E. Lee, R. A. De Souza, M. Martin, "Equal mobility of constituent cations in BaTiO₃," *Appl. Phys. Lett.* **92** (2008) 252103
- [27] C. Tubandt, E. Lorenz, "Das elektrische Leitvermögen als Methode zur Bestimmung des Zustandsdiagramms binärer Salzgemische," *Z. Phys. Chem.* **87** (1914) 543-561
- [28] E. M. Levin, C. R. Robbins, H. F. McMurdie, "Phase diagrams for ceramists," ed. by M. K. Reser, The American Ceramic Society, Columbus, Ohio, 1969, Fig. 52
- [29] *ibid.* Fig. 220
- [30] *ibid.* Fig. 256
- [31] *ibid.* Fig. 228
- [32] *ibid.* Fig. 258
- [33] R. A. De Souza, J. Maier, "A computational study of cation defects in LaGaO₃," *Phys. Chem. Chem. Phys.* **5** (2003) 740-748
- [34] R. A. De Souza, M. S. Islam, E. Ivers-Tiffée, "Formation and migration of cation defects in the perovskite oxide LaMnO₃," *J. Mater. Chem.* **9** (1999) 1621-1627
- [35] M. S. Islam, "Ionic transport in ABO₃ perovskite oxides: a computer modeling tour," *J. Mater. Chem.* **10** (2000) 1027-1038
- [36] H. Schmalzried, *Chemical Kinetics of Solids*, VCH Verlag GmbH, Weinheim, Germany, 1995, p. 162-163

- [37] F. A. Kröger, H. J. Vink, "Relations between the concentrations of imperfections in crystalline solids," in *Solid State Physics*, vol. 3, ed. F. Seitz and D. Turnbull, Academic Press, New York, 1956
- [38] H. -S. Kim, H. -I. Yoo, "Defect-chemical analysis of the nonstoichiometry, conductivity and thermopower of $\text{La}_2\text{NiO}_{4+\delta}$," *Phys. Chem. Chem. Phys.* **12** (2010) 4704-4713
- [39] S. -H. Park, H. -I. Yoo, "Thermoelectric behavior of a mixed ionic electronic conductor, $\text{Ce}_{1-x}\text{Gd}_x\text{O}_{2-x/2-\delta}$," *Phys. Chem. Chem. Phys.* **11** (2009) 391-401
- [40] H. Schmalzried, W. Laqua, P. L. Lin, "Crystalline oxide solid solutions in oxygen potential gradients," *Z. Naturforsch.* **34a** (1979) 192-199
- [41] G. J. Yurek, H. Schmalzried, "Deviations from local thermodynamic equilibrium during interdiffusion of CoO-MgO and CoO-NiO," *Ber. Bunsenges. Phys. Chem.* **79** (1975) 255-262
- [42] G. Schwier, R. Dieckmann, H. Schmalzried, "Punktfehlstellen in Oxidmischphasen (I) Fehlstellenthermodynamik der Mischphasen $(\text{Co}_x\text{Mg}_{1-x})\text{O}$ und $(\text{Co}_x\text{Mg}_{1-x})_2\text{SiO}_4$," *Ber. Bunsenges. Phys. Chem.* **77** (1973) 402-408
- [43] H. Schmalzried, W. Laqua, "Multicomponent oxides in oxygen potential gradients," *Oxid. Met.* **15** (1981) 339-353
- [44] W. Laqua, E. W. Schulz, B. Reuter, "Phasenverhältnisse und Reaktionen im System NiO-TiO₂," *Z. Anorg. Allg. Chem.* **433** (1977) 167-180
- [45] A. Muan, "Equilibrium relations in the system NiO-TiO₂ in the temperature range 1300° to 1750°C," *J. Am. Ceram. Soc.* **75** (1992) 1357-1360
- [46] Y. Ueshima, H. Schmalzried, J. Koepke, "Demixing in oxygen potential gradients: two-phase systems and the morphological stability of the interface," *Ber. Bunsenges. Phys. Chem.* **92** (1989) 24-29
- [47] M. Martin, "Electrotransport and demixing in oxides," *Solid State Ion.* **136-137** (2000) 331-337
- [48] M. Martin, R. Schmackpfeffer, "Demixing in trivalent doped transition metal oxides exposed to an oxygen potential gradient," *Ber. Bunsenges. Phys. Chem.* **93** (1989) 1271-1275

- [49] M. Martin, "Demixing of oxides: influence of cross-terms in the transport coefficients," *Ceram. Trans.* **24** (1991) 91-102
- [50] J. R. Manning, "Diffusion and ionic conductivity: kinetic theory," in *Mass transport in oxides, Proceedings of a symposium held at the National Bureau of Standards, Gaithersburg, Md., Oct. 22-25, 1967*, ed. by J. B. Wachtman Jr. and A. D. Franklin, Nat. Bur. Stand. (US) Special Publication 296 (1968) 53-63
- [51] L. Zhang, G. E. Murch, "Computer simulation of the de-mixing in solid solution oxides," *Phil. Mag. A* **62** (199) 267-274
- [52] A. R. Allnatt, A. B. Lidiard, "Statistical theories of atomic transport in crystalline solids," *Rep. Prog. Phys.* **50** (1987) 373-472
- [53] M. Martin, R. Schmackpfeffer, "Demixing of doped oxides: influence of defect interactions," *Solid State Ion.* **72** (1994) 67-71
- [54] R. Schmackpfeffer, M. Martin, "Tracer diffusion and defect structure in Ga-doped CoO," *Phil. Mag. A* **68** (1993) 747-765
- [55] K. Vedula, "Modeling of transient and steady-state demixing of oxide solid solutions in an oxygen chemical potential gradient," *Oxid. Met.* **28** (1987) 99-108
- [56] T. Ishikawa, S. A. Akbar, W. Zhu, H. Sato, "Time evolution of demixing in oxides under an oxygen potential gradient," *J. Am. Ceram. Soc.* **71** (1988) 513-521
- [57] D. Monceau, C. Petot, G. Petot-Ervas, "Kinetic demixing profile calculation in oxide solid solutions under a chemical potential gradient," *Solid State Ion.* **45** (1991) 231-237
- [58] J. -O. Hong, O. Teller, M. Martin, H. -I. Yoo, "Demixing of mixed oxide (A,B)O in an oxygen potential gradient: numerical solution of the time evolution of the demixing process," *Solid State Ion.* **123** (1999) 75-85
- [59] I. V. Belova, M. J. Brown, G. E. Murch, "Analysis of kinetic demixing in a mixed oxide (A,B)O in an oxygen potential gradient," *Acta Mater.* **51** (2003) 1821-1826
- [60] I. V. Belova, M. J. Brown, G. E. Murch, "Analysis of kinetic demixing of (A,B)O oxides in an electric field and an oxygen potential gradient," *Solid State Ion.* **167** (2004) 175-182

- [61] M. J. Brown, I. V. Belova, G. E. Murch, "Prediction of kinetic demixing in a quaternary mixed oxide (A, B, C)O in an oxygen potential gradient," *Phil. Mag.* **83** (2003) 1855-1865
- [62] J. Wolfenstine, D. Dimos, D. L. Kohlstedt, "Decomposition of Ni_2SiO_4 in an oxygen potential gradient," *J. Am. Ceram. Soc.* **68** (1985) C117-C118
- [63] K. T. Jacob, A. K. Shukla, "Kinetic decomposition of Ni_2SiO_4 in oxygen potential gradients," *J. Mater. Res.* **2** (1987) 338-344
- [64] H. J. Windhager, G. Borchardt, "Tracerdiffusion und Fehlordnung in dem Orthosilikat Co_2SiO_4 ," *Ber. Bunsenges. Phys. Chem.* **79** (1975) 1115-1119
- [65] J. Hermeling, H. Schmalzried, "Tracerdiffusion of Fe-cations in olivine ($\text{Fe}_x\text{Mg}_{1-x}$) $_2\text{SiO}_4$ (III)," *Phys. Chem. Minerals* **11** (1984) 161-166
- [66] R. Weghöft, H. Schmalzried, "On the behavior of fayalite and olivine in oxygen potential gradients," *Mater. Sci. Forum* **7** (1986) 223-234
- [67] U. Brinkmann, W. Laqua, "Decomposition of Fayalite (Fe_2SiO_4) in an oxygen potential gradient at 1418 K," *Phys. Chem. Minerals* **12** (1985) 283-290
- [68] R. A. Giddings, R. S. Gordon, "Review of oxygen activities and phase boundaries in wüstite as determined by electromotive-force and gravimetric methods," *J. Am. Ceram. Soc.* **56** (1973) 111-116
- [69] D. C. Azubike, A. Chrysanthou, B. S. Terry, "Kinetic dissociation of nickel titanate and nickel tungstate in oxygen potential gradients," *J. Mater. Sci.* **29** (1994) 2957-2962
- [70] S. Sawada, "Thermal and electrical properties of tungsten oxide (WO_3)," *J. Phys. Soc. Jap.* **11** (1956) 1237-1246
- [71] E. M. Levin, C. R. Robbins, H. F. McMurdie, "Phase diagrams for ceramists," ed. by M. K. Reser, The American Ceramic Society, Columbus, Ohio, 1969, Fig. 2084
- [72] N. Cebasek, T. Norby, Z. Li, "Kinetic decomposition of a $\text{La}_2\text{NiO}_{4+\delta}$ membrane under an oxygen potential gradient," *J. Electrochem. Soc.* **159** (2012) F461-467
- [73] N. Cebasek, R. Haugsrud, Z. Li, J. Milosevic, J. B. Smith, A. Magraso, T.

- Norby, "Determination of the self-diffusion coefficient of Ni^{2+} in $\text{La}_2\text{NiO}_{4+\delta}$ by the solid state reaction method," *J. Electrochem. Soc.* **159** (2012) B702-B708
- [74] R. H. E. van Doorn, H. J. M. Bouwmeester, A. J. Burggraaf, "Kinetic decomposition of $\text{La}_{0.3}\text{Sr}_{0.7}\text{CoO}_{3-\delta}$ perovskite membranes during oxygen permeation," *Solid State Ion.* **111** (1998) 263-272
- [75] H. Yokokawa, T. Horita, N. Sakai, M. Dokiya, T. Kawada, "Thermodynamic considerations on interfaces in electrochemical devices," International Workshop on Ceramic Interfaces: Properties and Applications III, Kuranda, July, 1996
- [76] H. L. Lein, K. Wiik, T. Grande, "Kinetic demixing and decomposition of oxygen permeable membranes," *Solid State Ion.* **177** (2006) 1587-1590
- [77] B. Wang, B. Zydorczak, Z. -T. Wu, K. Li, "Stabilities of $\text{La}_{0.6}\text{Sr}_{0.4}\text{Co}_{0.2}\text{Fe}_{0.8}\text{O}_{3-\delta}$ oxygen separation membranes - effects of kinetic demixing/decomposition and impurity segregation," *J. Membr. Sci.* **344** (2009) 101-106
- [78] D. Schlehner, E. Wessel, L. Singheiser, T. Markus, "Long-term operation of a $\text{La}_{0.58}\text{Sr}_{0.4}\text{Co}_{0.2}\text{Fe}_{0.8}\text{O}_{3-\delta}$," *J. Membr. Sci.* **351** (2010) 16-20
- [79] B. Wang, B. Zydorczak, D. Poulidi, I. S. Metcalfe, K. Li, "A further investigation of the kinetic demixing/decomposition of $\text{La}_{0.6}\text{Sr}_{0.4}\text{Co}_{0.2}\text{Fe}_{0.8}\text{O}_{3-\delta}$ oxygen separation membranes," *J. Membr. Sci.* **369** (2011) 526-535
- [80] J. -I. Jung, D. D. Edwards, "Kinetic demixing/decomposition of $\text{Ba}_{0.5}\text{Sr}_{0.5}\text{Co}_x\text{Fe}_{1-x}\text{O}_{3-\delta}$," *J. Eur. Ceram. Soc.* **32** (2012) 3733-3743
- [81] D. T. Bray, U. Merten, "Transport numbers in stabilized zirconia," *J. Electrochem. Soc.* **111** (1964) 447-452
- [82] D. Monceau, M. Filal, M. Tebtoub, C. Petot, G. Petot-Ervas, "Kinetic demixing of ceramics in an electric field," *Solid State Ion.* **73** (1994) 221-225
- [83] O. Teller, M. Martin, "Kinetic demixing of (Co,Ni)O in an electric field," *Solid State Ion.* **101-103** (1997) 475-478
- [84] W. K. Chen, N. L. Peterson, "Cation diffusion, semiconductivity and nonstoichiometry in (Co,Ni)O crystals," *J. Phys. Chem. Solids* **34** (1973) 1093-1108

- [85] H. Schmalzried, "Behavior of (semiconducting) oxide crystals in oxygen potential gradients," *React. Solids* **1** (1986) 117-137
- [86] O. Teller, M. Martin, "Kinetic demixing of heterovalently doped CoO in an electric field," *Ber. Bunsenges. Phys. Chem.* **101** (1997) 1377-1380
- [87] J. -O. Hong, H. -I. Yoo, "Electrotransport-induced demixing in semiconducting $(\text{Mn}_x\text{Fe}_{1-x})_3\text{O}_4$," *Solid State Ion.* **113-115** (1998) 265-270
- [88] J. -H. Lee, H. -I. Yoo, "Electrochemical study of the cross effect between ion and electron flows in semiconducting CoO," *J. Electrochem. Soc.* **141** (1994) 2789-2794
- [89] D. P. Korfiatis, S. F. Potamianou, E. D. Gwagarakis, K. A. Th. Thoma, "Demixing profiles in oxides upon the application of an electric field," *Solid State Ion.* **136-137** (2000) 1367-1371
- [90] J. -O. Hong, H. -I. Yoo, O. Teller, M. Martin, J. Mizusaki, "Unmixing of a mixed oxide (A,B)O in an electric field: numerical solution of the time evolution of the unmixing process," *Solid State Ion.* **144** (2001) 241-248
- [91] P. Ruello, A. Rizea, C. Petot, G. Petot-Ervas, M. J. Graham, G. I. Sproule, "Kinetic demixing in yttria-doped zirconia part II - theoretical analysis," *Ionics* **7** (2001) 81-84
- [92] J. W. Gibbs, "On the equilibrium of heterogeneous substances," in *Transactions of the Connecticut Academy of Arts and Sciences, Vol. III, New Haven: Published by the Academy 1874 to 1878*, Tuttle, Morehouse & Taylor, New Haven, 1878, pp. 501-520
- [93] W. T. Petuskey, H. K. Bowen, "Thermal segregation of cations in iron aluminate spinels," *J. Am. Ceram. Soc.* **64** (1981) 611-617
- [94] H. Timm, J. Janek, "On the Soret effect in binary nonstoichiometric oxides - kinetic demixing of cuprite in a temperature gradient," *Solid State Ion.* **176** (2005) 1131-1143
- [95] S. A. Akbar, M. Kaburagi, H. Sato, R. Kikuchi, "Demixing of oxides under a temperature gradient," *J. Am. Ceram. Soc.* **70** (1987) 246-253

- [96] D. Monceau, C. Petot, G. Petot-Ervas, "Kinetic demixing profile calculation under a temperature gradient in multi-component oxides," *J. Eur. Ceram. Soc.* **9** (1992) 193-204
- [97] D. Dimos, J. Wolfenstine, D. L. Kohlstedt, "Kinetic demixing and decomposition of multicomponent oxides due to a nonhydrostatic stress," *Acta Metall.* **36** (1988) 1543-1552
- [98] W. A. Bassett, L. -C. Ming, "Disproportionation of Fe_2SiO_4 to $2\text{FeO}+\text{SiO}_2$ at pressures up to 250 kbar and temperatures up to 3000°C," *Phys. Earth Planet. Interiors* **6** (1972) 154-160
- [99] E. Ito, "High-pressure decompositions in cobalt and nickel silicates," *Phys. Earth Planet. Interiors* **10** (1975) 88-93
- [100] V. M. Goldschmidt, "Die Gesetze der Krystallochemie," *Naturwissenschaften* **14** (1926) 477-485
- [101] R. D. Shannon, "Revised effective ionic radii and systematic studies of interatomic distances in halides and chalcogenides," *Acta Cryst. A* **32** (1976) 751-767
- [102] J. Ko, C. Prewitt, "High-pressure phase transformation in MnTiO_3 from the ilmenite to the LiNbO_3 structure," *Phys. Chem. Mineral* **15** (1988) 355-362
- [103] J. A. Linton, Y. Fei, A. Navrotsky, "The MgTiO_3 - FeTiO_3 join at high pressure and temperature," *Am. Mineral.* **84** (1999) 1595-1603
- [104] C. Stüber, M. Lerch, W. Laqua, "The effect of an order-disorder transition on the high temperature electrical conductivity of NiTiO_3 ," *Z. Anorg. Allg. Chem.* **621** (1995) 1471-1477
- [105] M. Lerch, C. Stüber, W. Laqua, "Aspekte eines Hochtemperaturphasenübergangs in NiTiO_3 ," *Z. Anorg. Allg. Chem.* **594** (1991) 167-178
- [106] R. W. Taylor, H. Schmalzried, "The free energy of formation of some titanates, silicates, and magnesium aluminate from measurements made with galvanic cells involving solid electrolytes," *J. Phys. Chem.* **68** (1964) 2444-2449
- [107] L. Pejryd, "Solid state EMF study of the equilibrium $\text{Ni(s)}+\text{TiO}_2\text{(s)}+1/2\text{O}_2\text{(g)}=\text{NiTiO}_3\text{(s)}$ in the temperature range 1020-1520 K," *Acta*

- Chem. Scand. A* **38** (1984) 241-246
- [108] M. Lerch, W. Laqua, "Zur Thermodynamik und elektrischen Leitfähigkeit von NiTiO₃ und anderen oxidischen Phasen mit Ilmenitstruktur," *Z. Anorg. Allg. Chem.* **610** (1992) 57-63
- [109] G. M. Kale, "Electrochemical determination of Gibbs free energy of formation of NiTiO₃ (ilmenite)," *Metall. Mater. Trans. B* **29** (1998) 31-38
- [110] K. T. Jacob, V. S. Saji, S. N. S. Reddy, "Thermodynamic evidence for order-disorder transition in NiTiO₃," *J. Chem. Thermodynamics* **39** (2007) 230-235
- [111] I. Barin, *Thermochemical Data of Pure Substances*, VCH Verlags GmbH, Weinheim, 1993, vol. 1-2
- [112] H. Schmalzried, *Solid State Reactions, 2ed.*, Verlag Chemie, Weinheim, 1981, pp. 104-112
- [113] N. Cebasek, R. Haugrud, Z. Li, T. Norby, "Determination of chemical tracer diffusion coefficients for the La- and Ni-site in La₂NiO_{4+δ} studied by SIMS," *J. Am. Ceram. Soc.* **96** (2013) 598-605
- [114] A. D. Smigelskas, E. O. Kirkendall, "Zinc diffusion in alpha brass," *Trans. AIME* **171** (1947) 130-142
- [115] L. S. Darken, "Diffusion, mobility and their interrelation through free energy in binary metallic systems," *Trans. AIME* **175** (1948) 184-201
- [116] H. Nakajima, "The discovery and acceptance of the Kirkendall effect: The result of a short research career," *J. Mat.* **49** (1997) 15-19
- [117] R. W. Balluffi, S. M. Allen, W. C. Carter, *Kinetics of Materials*, John Wiley & Sons, Inc., Hoboken, New Jersey, 2005, pp. 163-167
- [118] R. E. Carter, "Mechanism of solid-state reaction between magnesium oxide and aluminum oxide and between magnesium oxide and ferric oxide," *J. Am. Ceram. Soc.* **44** (1961) 116-120
- [119] J. Gilewicz-Wolter, "Study of iron oxidation in sulfur dioxide atmospheres by means of the ³⁵S radioisotope," *Oxid. Met.* **11** (1977) 81-90
- [120] T. G. Finstad, M. W. Mayer, M. -A. Nicolet, "The formation of NiSi from Ni₂Si studied with a platinum marker," *Thin Solid Films* **51** (1978) 391-394

- [121] J. A. Costello, R. E. Tressler, "Oxidation kinetics of hot-pressed and sintered α -SiC," *J. Am. Ceram. Soc.* **64** (1981) 327-331
- [122] H. Sieber, D. Hesse, X. Pan, St. Senz, J. Heydenreich, "TEM investigations of spinel-forming solid state reactions: reaction mechanism, film orientation, and interface structure during MgAl_2O_4 formation on MgO (001) and Al_2O_3 ($1\bar{1}.2$) single crystal substrates," *Z. Anorg. Allg. Chem.* **622** (1996) 1658-1666
- [123] T. Narita, W. W. Smeltzer, "Sulfidation mechanism of an Fe-26.2 at.% Cr alloy at temperatures 973-1173 K in H_2S - H_2 atmospheres at sulfur pressures 10^4 - 10^6 Pa," *Oxid. Met.* **21** (1984) 57-69
- [124] M. T. Johnson, S. R. Gilliss, C. B. Carter, "Use of Pt markers in the study of solid-state reactions in the presence of an electric field," *Microsc. Microanal.* **4** (1998) 158-163
- [125] C. Korte, N. D. Zakharov, D. Hesse, "Electric field driven solid state reactions-microscopic investigation of moving phase boundaries in the system $\text{MgO}/\text{MgIn}_2\text{O}_4/\text{In}_2\text{O}_3$," *Phys. Chem. Chem. Phys.* **5** (2003) 5530-5535
- [126] J. B. Smith, T. Norby, "Cation self-diffusion in LaFeO_3 measured by the solid state reaction method," *Solid State Ion.* **177** (2006) 639-646
- [127] M. Palcut, K. Wiik, T. Grande, "Cation self-diffusion and nonstoichiometry of lanthanum manganite studied by diffusion couple measurements," *J. Phys. Chem. C* **111** (2007) 813-822
- [128] M. Palcut, K. Wiik, T. Grande, "Cation self-diffusion in LaCoO_3 and La_2CoO_4 studied by diffusion couple experiments," *J. Phys. Chem. C* **111** (2007) 2299-2308
- [129] C. B. Alcock, M. G. Hocking, S. Zador, "The corrosion of Ni in O_2 + SO_2 atmospheres in the temperature range 500-750°C," *Corrosion Sci.* **9** (1969) 111-122
- [130] K. Kowalska, E. Roszczynialska, T. Werber, "Effect of a marker material on the oxidation of nickel in sulfur dioxide," *Oxid. Met.* **15** (1981) 399-405
- [131] G. J. van Gorp, W. F. van der Weg, D. Sigurd, "Interactions in the Co/Si thin-film system. II. Diffusion-marker experiments," *J. Appl. Phys.* **49** (1978) 4011-4020

- [132] M. Bartur, M. -A. Nicolet, "Marker experiments for diffusion in the silicide during oxidation of PdSi, Pd₂Si, CoSi₂, and NiSi₂ films on <Si>," *J. Appl. Phys.* **54** (1983) 5404-5415
- [133] J. Tardy, K. N. Tu, "Solute effect of Cu on interdiffusion in Al₃Ti compound films," *Phys. Rev. B* **32** (1985) 2070-2081
- [134] L. Stolt, F. M. D'Heurle, "The formation of Cu₃Si: marker experiments," *Thin Solid Films* **189** (1990) 269-274
- [135] H. Schmalzried, "Chemical Kinetics of Solids," VCH Verlag GmbH, Weinheim, Germany, 1995, pp. 189-191
- [136] J. W. Gibbs, "On the equilibrium of heterogeneous substances," in *Transactions of the Connecticut Academy of Arts and Sciences, Vol. III, New Haven: Published by the Academy 1874 to 1878*, Tuttle, Morehouse & Taylor, New Haven, 1878, pp. 140-148
- [137] G. Wiedemann, *Die Lehre von der Electricität, 2ed*, Vieweg und Sohn, Braunschweig, Vol. 1 (1893) pp. 553-561, 815-819, Vol. 2 (1898) pp. 491-493
- [138] J. -M. Gaugain, "Note sur les signes électriques attribués au mouvement de la chaleur," *C R Séances Acad Sciences* **37** (1853) 82-84
- [139] H. Buff, "Über die elektrische Leitfähigkeit des erhitzten Glases," *Ann. Chem. Pharm.* **90** (1854) 257-283
- [140] H. Helmholtz, "On the Thermodynamics of Chemical Processes," in *Physical Memoirs Selected and Translated from Foreign Sources, Vol. I*, Physical Society of London, Taylor and Francis, 1888, pp. 43-97
- [141] G. Lewis, M. Randall, *Thermodynamics and the Free Energy of Chemical Substances*, McGraw-Hill Book Company, New York, London, 1923, pp. 168
- [142] F. Haber, A. Moser, "Das Generatorgas und das Kohlenelement," *Z. Elektrochem.* **11** (1905) 593-609
- [143] E. A. Guggenheim, *Thermodynamics, An Advanced Treatment for Chemists and Physicists*, Elsevier Science Publishing Company, New York, 1967, pp. 312

- [144] K. Kiukkola, C. Wagner, "Measurements on galvanic cells involving solid electrolytes," *J. Electrochem. Soc.* **104** (1957) 379-386
- [145] R. Benz, C. Wagner, "Thermodynamics of the solid system CaO-SiO₂ from electromotive force data," *J. Phys. Chem.* **65** (1961) 1308-1311
- [146] R. H. Gerke, "Temperature coefficient of electromotive force of galvanic cells and the entropy of reactions," *J. Am. Chem. Soc.* **44** (1922) 1684-1704
- [147] T. J. Webb, "The third law of thermodynamics and calculation of entropies," *J. Phys. Chem.* **29** (1925) 816-833
- [148] A. B. Newman, G. G. Brown, "Minimum voltage to reduce aluminum oxide," *Ind. Eng. Chem.* **22** (1930) 995-1000
- [149] P. Drossbach, "Das theoretische Potential des Aluminiums," *Z. Elektrochem.* **33** (1927) 114-117
- [150] P. Drossbach, "Die Zersetzungsspannung der Tonerde in geschmolzenem Kryolith-tonerdegemisch," *Z. Elektrochem.* **36** (1930) 179-181
- [151] M. DeKay Thompson, R. G. Seyl, "Depolarization by graphite anodes in the electrolysis of aluminum oxide," *Trans. Electrochem. Soc.* **64** (1933) 321-327
- [152] J. W. Cuthbertson, J. Waddington, "A Study of the cryolite-alumina cell with particular reference to decomposition voltage," *Trans. Farad. Soc.* **32** (1936) 745-760
- [153] C. Wagner, *Atom Movements*, American Society of Metals, Metals Park, Ohio, 1951, pp. 153-173
- [154] S. Koerfer, R. A. De Souza, H. -I. Yoo, M. Martin, "Diffusion of Sr and Zr in BaTiO₃ single crystals," *Solid State Sci.* **10** (2007) 725-734
- [155] R. Wernicke, "Defect chemistry and electrical conductivity of doped barium titanate ceramics: part 4. the kinetics of equilibrium restoration in barium titanate ceramics," *Philips Res. Rep.* **31** (1976) 526-543 (from Koerfer [154])
- [156] A. Kitahara, M. Nanko, K. Kawamura, T. Maruyama, "Diffusion coefficient of Ba²⁺ ion in BaTiO₃," *Electrochem. Soc. Proc.* **PV99-38** (1999) 534-545
- [157] D. E. Rase, R. Roy, "Phase equilibria in the system BaO-TiO₂," *J. Am. Ceram. Soc.* **38** (1955) 102-113

- [158] J. Crawford, P. Jacobs, "Point defect energies for strontium titanate: a pair-potentials study," *J. Solid State Chem.* **144** (1999) 423-429
- [159] M. J. Akhtar, Z. Akhtar, R. A. Jackson, C. R. A. Catlow, "Computer simulation studies of strontium titanate," *J. Am. Ceram. Soc.* **78** (1995) 421-428
- [160] T. Akashi, M. Nanko, T. Maruyama, Y. Shiraishi, J. Tanabe, "Solid-state reaction kinetics of LaCrO_3 from the oxides and determination of La^{3+} diffusion coefficient," *J. Electrochem. Soc.* **145** (1998) 2090-2094
- [161] K. Kawamura, A. Saiki, T. Maruyama, K. Nagata, "Diffusion coefficient of yttrium ion in YCrO_3 ," *J. Electrochem. Soc.* **142** (1995) 3073-3077
- [162] T. Akashi, Y. Mizuno, M. Nanko, T. Maruyama, A. Saiki, K. Tsukui, J. Tanabe, "Determination of diffusion coefficient of Nd^{3+} in NdCrO_3 based on solid state reaction," *Mater. Trans.* **42** (2001) 1411-1416
- [163] V. Buscaglia, M. T. Buscaglia, L. Giordano, A. Martinelli, M. Viviani, C. Bottino, "Growth of ternary oxides in the $\text{Gd}_2\text{O}_3\text{-Fe}_2\text{O}_3$ system. A diffusion couple study," *Solid State Ion.* **146** (2001) 257-271
- [164] S. Miyoshi, M. Martin, "B-site cation diffusivity of Mn and Cr in perovskite-type LaMnO_3 with cation-deficit nonstoichiometry," *Phys. Chem. Chem. Phys.* **11** (2009) 3063-3070
- [165] M. Kilo, M. A. Taylor, C. Argirusis, G. Borchardt, R. A. Jackson, O. Schulz, M. Martin, M. Weller, "Modeling of cation diffusion in oxygen ion conductors using molecular dynamics," *Solid State Ion.* **175** (2004) 823-827
- [166] O. Schulz, M. Martin, C. Argirusis, G. Borchardt, "Cation tracer diffusion of ^{138}La , ^{84}Sr and ^{25}Mg in polycrystalline $\text{La}_{0.9}\text{Sr}_{0.1}\text{Ga}_{0.9}\text{Mg}_{0.9}\text{O}_{2.9}$," *Phys. Chem. Chem. Phys.* **5** (2003) 2308-2313
- [167] D. R. Gaskell, *Introduction to the Thermodynamics of Materials*, Taylor & Francis, New York, London, 5th ed., 2003, pp. 211-261
- [168] K. J. D. Mackenzie, R. K. Banerjee, M. R. Kasaai, "Effect of electric field on solid-state reactions between oxides Part 1 Reaction between calcium and aluminium oxides," *J. Mater. Sci.* **14** (1979) 333-338

- [169] K. J. D. Mackenzie, R. K. Banerjee, "Effect of electric fields on solid-state reactions between oxides Part 2 Interdiffusion studies in polycrystalline calcium and aluminium oxide pellets," *J. Mater. Sci.* **14** (1979) 339-344
- [170] I. Kohatsu, G. W. Brindley, "solid state reactions between CaO and α -Al₂O₃," *Z. Phys. Chem. NF* **60** (1968) 79-89
- [171] K. J. D. Mackenzie, M. J. Ryan, "Effect of electric fields on solid-state reactions between oxides Part 3 Interdiffusion in polycrystalline magnesium and aluminium oxide pellets," *J. Mater. Sci.* **16** (1981) 579-588
- [172] M. T. Johnson, H. Schmalzried, C. B. Carter, "The effect of an applied electric field on a heterogeneous solid-state reaction," *Solid State Ion.* **101-103** (1997) 1327-1333
- [173] M. T. Johnson, C. B. Carter, H. Schmalzried, "Behavior of MgFe₂O₄ films on MgO in an electric field," *J. Am. Ceram. Soc.* **83** (2000) 1768-1772
- [174] C. Korte, N. Ravishankar, C. B. Carter, H. Schmalzried, "Kinetics of formation in an external applied electric field," *Solid State Ion.* **148** (2002) 111-121
- [175] C. Korte, B. Franz, D. Hesse, "Electric field driven solid state reactions - reactions kinetics and the influence of grain boundaries on the interface morphology in the system MgO/MgIn₂O₄/In₂O₃," *Phys. Chem. Chem. Phys.* **7** (2005) 413-420
- [176] D. -K. Lee, "Defect structure and mass/charge transport properties of TiO₂," Ph. D thesis, Seoul National University, Seoul, Korea (2005)
- [177] J. -Y. Jeong, "Ionic transference number and the charge of transport of Ni_{1-x}O," M. Sc. thesis, Seoul National University, Seoul, Korea (1997)

Appendix – data

(1) Total conductivity of NiTiO₃ in air

(a) I-V curve and linearity

Current / A	Voltage / V		
	1200°C	1300°C	1400°C
2E-5	0.00302	4.2004E-4	2.16779E-4
4E-5	0.00613	9.25586E-4	4.70079E-4
6E-5	0.00926	0.00143	7.1959E-4
8E-5	0.0124	0.00193	9.7165E-4
1E-4	0.01552	0.00244	0.00122
-2E-5	-0.00319	-5.88922E-4	-2.8645E-4
-4E-5	-0.0063	-0.00109	-5.38357E-4
-6E-5	-0.00944	-0.0016	-7.8972E-4
-8E-5	-0.01257	-0.0021	-0.00104
-1E-4	-0.01565	-0.00261	-0.00129
2E-4	0.03132	0.00496	0.00248
4E-4	0.0626	0.01	0.00499
6E-4	0.09371	0.01504	0.0075
8E-4	0.1247	0.02009	0.01002
1E-3	0.15587	0.02513	0.01253
-2E-4	-0.03147	-0.00513	-0.00255
-4E-4	-0.06268	-0.01016	-0.00505
-6E-4	-0.09378	-0.01522	-0.00758
-8E-4	-0.12485	-0.02026	-0.01009
-1E-3	-0.15611	-0.0253	-0.0126
0.002	0.31284	0.05043	0.02509
0.004	0.62658	0.1096	0.05017
0.006	0.93963	0.15147	0.07527
0.008	1.24852	0.2018	0.10039
0.01	1.55547	0.25224	0.12556

-0.002	-0.31348	-0.05063	-0.02516
-0.004	-0.62739	-0.10115	-0.05025
-0.006	-0.93926	-0.1516	-0.07537
-0.008	-1.54774	-0.20196	-0.10051
-0.01	-1.55543	-0.25248	-0.12564
0.02	3.12166	0.50284	0.25132
0.04	6.1439	1.00378	0.5017
0.06	9.1287	1.50214	0.75114
0.08	11.9283	1.98713	0.9985
0.1	14.9561	2.45571	1.24341
-0.02	-3.11388	-0.50417	-0.25142
-0.04	-6.06293	-1.00468	-0.50172
-0.06	-9.1282	-1.49809	-0.75092
-0.08	-12.0665	-1.97837	-0.9979
-0.1	-13.9137	-2.43882	-1.24146
Linearity	0.99868	0.99991	0.99878

(b) Arrhenian plot of total conductivity of NiTiO₃ in air (Fig. 3-12)

Temp / °C	T / K	1000/T / 1/K	σ / Scm ⁻¹	$\delta\sigma$ / Scm ⁻¹	% error
1200	1473.15	0.67882	0.02013	8.35575E-5	0.42
1300	1573.15	0.63567	0.12999	9.55511E-4	0.74
1400	1673.15	0.59768	0.27204	0.0023	0.85

(2) EPMA profiles of unmixing/decomposition experiment

(a) $U_{\text{appl}}=2.2 \text{ V}$

(i) Overall specimen (Fig. 3-17 (a))

Distance from anode / μm	Ti/Ni
0	1.10647
50	1.05637
100	1.03896
150	1.03299
200	1.02778
250	1.02845
300	1.02437
350	1.01639
400	1.00875
450	1.00321
500	1.00298
550	0.9988
600	0.98689
650	0.98631
700	0.98566
750	0.98148
800	0.97399
850	0.9652
900	0.96483
950	0.96567
1000	0.95946
1050	0.95503
1100	0.95133
1150	0.95749
1200	0.96313

1250	0.97116
1350	0.97419
1400	0.93732

(ii) Anode and cathode (Fig. 3-17 (b) and (c))

Anode		Cathode	
Distance from anode / μm	$\log(\text{Ti/Ni})$	Distance from Pt marker / μm	$\log(\text{Ti/Ni})$
2	2.72274	-2	-0.04783
4	2.82117	0	-0.11225
6	2.80933	2	-0.89874
8	2.78216	4	-0.88381
10	2.80238	6	-0.83498
12	2.75451	8	-0.83786
14	2.69854	10	-0.83156
16	2.6878	12	-0.83703
18	2.65382	14	-0.84503
20	2.47423	16	-0.8539
22	1.95787	18	-0.86475
24	2.4399	20	-0.86861
26	2.51504	22	-0.87707
28	2.26576	24	-0.88513
30	2.31621	26	-0.89004
32	2.1411	28	-0.89757
34	2.43001	30	-0.90349
36	2.3656	32	-0.9121
38	2.14009	34	-0.92334
40	2.3442	36	-0.91961
42	2.34905	38	-0.92598

44	2.19986	40	-0.93319
46	2.24225	42	-0.94231
48	2.20276	44	-0.94749
50	2.0902	46	-0.95383
52	0.94613	48	-0.95744
54	0.4628	50	-0.97279
		52	-0.97784
		54	-0.99787
		56	-1.04336

(b) $U_{\text{appl}}=0.3 \text{ V}$

(i) Overall specimen (Fig. 3-19)

Distance from anode / μm	Ti/Ni
65	1.08354
130	1.05654
195	1.06481
260	1.02645
325	1.01345
390	1.00631
455	0.98405
520	0.99346
650	0.94535
715	0.96471
780	0.96192
845	0.95318
975	0.96142
1105	0.96023
1235	0.93486

(ii) Anode and cathode

Anode		Cathode	
Distance from anode / μm	$\log(\text{Ti/Ni})$	Distance from Pt marker / μm	$\log(\text{Ti/Ni})$
0	2.12525	0	-0.04253
2	2.91126	2	-1.28993
4	2.76283	4	-2.05108
6	2.05443	6	-2.02656
8	2.74838	8	-2.04506
10	2.34824	10	-2.0487

12	2.15442	12	-2.01235
14	2.56671		
16	2.57892		
18	2.53572		
20	2.41844		
22	2.38105		
24	2.31171		
26	2.27663		
28	2.20044		
30	2.12671		
32	2.07346		
34	1.9942		
36	1.23183		
38	-0.5444		

(c) $U_{\text{appl}}=0.2 \text{ V}$

(i) Overall specimen

Distance from anode / μm	Ti/Ni
65	1.10654
130	1.04564
195	1.05135
260	1.01035
325	1.00846
390	0.99463
455	0.98135
520	0.95138
650	0.96318
715	0.96945
780	0.96165
845	0.95186
975	0.96615
1105	0.94035
1235	0.92945

(ii) Anode and cathode

Anode		Cathode	
Distance from anode / μm	$\log(\text{Ti/Ni})$	Distance from Pt marker / μm	$\log(\text{Ti/Ni})$
2	2.21037	-2	-0.03938
4	2.61048	0	-0.05269
6	2.59889	2	-0.78772
8	2.23412	4	-0.88435
10	2.0861	6	-0.89318
12	2.50842	8	-0.87387

14	2.479	10	-0.85119
16	1.76883	12	-0.85051
18	2.26687	14	-0.88433
20	2.30803	16	-0.91695
22	2.24495	18	-0.92937
24	2.17153	20	-0.92961
26	2.07347	22	-0.94183
28	0.44545		
30	0.01757		

(d) $U_{\text{appl}}=0.143 \text{ V}$

(i) Overall specimen

Distance from anode / μm	Ti/Ni
65	1.10201
130	1.00629
195	1.04193
260	1.01116
325	1.01722
390	0.99562
455	0.95248
520	0.9436
650	0.97937
715	0.98215
780	0.98098
845	0.99227
975	0.97156
1105	0.9798
1235	0.91484

(ii) Anode and cathode

Anode		Cathode	
Distance from anode / μm	$\log(\text{Ti/Ni})$	Distance from Pt marker / μm	$\log(\text{Ti/Ni})$
0	1.84104	0	-0.0531
2	2.21454	2	-0.91961
4	2.40531	4	-0.98728
6	2.23972	6	-1.00784
8	1.85553	8	-0.99987
10	2.27048	10	-0.98351

12	2.21038	12	-1.08604
14	2.08618	14	-1.14945
16	2.03698		
18	1.8204		
20	0.01024		

(e) $U_{\text{appl}}=0.120 \text{ V}$

(i) Overall specimen

Distance from anode / μm	Ti/Ni
65	1.06375
130	1.04856
195	1.04812
260	1.03262
325	1.03785
390	1.02864
455	1.01648
520	1.03275
650	1.04865
715	0.99423
780	0.94237
845	0.98146
975	0.97534
1105	0.96185
1235	0.93268

(ii) Anode and cathode

Anode		Cathode	
Distance from anode / μm	$\log(\text{Ti/Ni})$	Distance from Pt marker / μm	$\log(\text{Ti/Ni})$
0	2.3165	0	-0.04285
2	2.20564	2	-0.92378
4	2.54963	4	-0.94538
6	2.13409	6	-1.05067
8	1.94352	8	-0.98946
10	2.24391	10	-0.98351

12	2.22015	12	-1.06684
14	1.73425	14	-1.09342
16	1.58435		
18	0.94538		

(f) $U_{\text{app}}=0.097 \text{ V}$

(i) Overall specimen (Fig. 3-15 (a))

Line 1		Line 2	
Distance from anode / μm	Ti/Ni	Distance from anode / μm	Ti/Ni
0	0.99929	0	1.00826
50	1.00859	50	1.00782
100	1.01565	150	1.00021
150	1.00752	200	0.99481
200	1.00863	250	0.99635
250	0.99889	300	0.98485
300	1.00105	350	0.98281
350	0.99231	400	0.98792
400	0.99378	450	0.98215
450	0.98775	500	0.98378
500	0.97974	550	0.98306
550	0.97986	600	0.98131
600	0.98393	650	0.97384
650	0.98531	700	0.98033
700	0.98481	750	0.97151
750	0.98528	800	0.97772
800	0.98233	850	0.97693
850	0.97569	900	0.97236
900	0.97519	950	0.9767
1000	0.97465	1000	0.97946
1050	0.98443	1100	0.97707
1100	0.97624	1150	0.97686
1250	0.94689	1200	0.97317

(ii) Anode and cathode (Fig. 3-15 (b), (c))

Anode		Cathode	
Distance from anode / um	log(Ti/Ni)	Distance from Pt marker / um	log(Ti/Ni)
2	1.00306	2	0.98821
7	0.99471	4	0.99703
12	0.99776	6	0.98985
15	0.99482	8	0.98984
18	0.99553	10	0.98857
20	0.99353	12	0.98698
23	0.98976	14	0.98708
26	0.98894	16	0.98348
29	0.99224	18	0.97373
32	0.99224	20	0.98277
35	0.99235	22	0.99568
37	0.99341	24	0.9949
42	0.99153	26	0.98815
45	0.99212	28	0.997
47	0.98624	30	0.9834
		32	0.98971
		34	0.98864
		36	0.99539
		38	1.00052
		40	0.99836
		42	0.99304
		44	0.99678
		46	0.99633
		48	0.9922

(3) Cation mobility ratio ψ

time / hrs	ψ	$\delta\psi$	% error
24	0.24264	0.08961	36.93
48	0.24452	0.03028	12.38
72	0.22148	0.01988	8.98
120	0.12074	0.00492	4.07

(4) Formation experiment – layer thicknesses

(a) (+)NiO/TiO₂(-), |I_{app}|=0.4 A

t / hrs	$\Delta x_{tot} / \mu\text{m}$	$\Delta x_A / \mu\text{m}$	$\Delta x_B / \Delta x_A = \Delta x_{tot} / \Delta x_A - 1$
12	132.6±36.7	-	-
24	171.7±23.2	172.2±15.3	$(1.95 \pm 0.3) \times 10^{-3}$
36	210.5±39.1	-	-
48	283.2±21.5	255.1±23.0	0.110±0.014
60	-	-	-
72	393.6±50.2	407.6±18.9	0.034±0.005
120	423.0±19.3	430.4±51.7	0.017±0.002

(b) no external current

t / hrs	$\Delta x_{tot} / \mu\text{m}$	$\Delta x_A / \mu\text{m}$	$\Delta x_B / \Delta x_A = \Delta x_{tot} / \Delta x_A - 1$
12	45.0±18.0	-	-
24	73.1±13.3	58.8±11.0	0.24±0.09
36	82.2±12.1	-	-
48	119.6±6.2	96.1±6.9	0.24±0.03
60	-	-	-
72	96.0±13.8	103.2±3.5	0.221±0.020
120	148.9±2.5	132.9±3.1	0.121±0.005

(c) (-)|NiO|TiO₂(+), |I_{appl}|=0.4 A

t / hrs	$\Delta x_{tot} / \mu m$	$\Delta x_A / \mu m$	$\Delta x_B / \Delta x_A =$ $\Delta x_{tot} / \Delta x_A - 1$
12	26.0±3.3	13.2±6.4	0.9±0.6
24	42.4±3.8	18.6±4.4	1.3±0.4
36	38.1±7.5	-	-
48	47.6±4.0	15.1±4.2	2.2±0.8
60	46.0±6.2	-	-
72	50.8±3.9	17.4±11.1	1.9±1.4
120	59.4±1.4	16.1±12.7	2.7±2.2

‡ The large error values, especially in (a) and (c), come mainly from the unstable morphology of the grown layers.

(5) Formation experiment – at constant duration (Fig. 5-10)

$I_{\text{appl}} / \text{A}$	Δx_{tot}	$\Delta x_{\text{B}}/\Delta x_{\text{A}}=\Delta x_{\text{tot}}/\Delta x_{\text{A}}-1$
0.4	393.6±50.2	0.003±0.176
0	96.0±13.8	0.221±0.020
-0.2	48.7±4.1	0.261±0.284
-0.4	50.8±3.9	0.223±0.121
-1.0	65.0±6.0	4.18±9.60

Appendix – List of Publications and Presentations

(1) List of Publications

1. Han-Il Yoo, Sang-Hyun Park and Jakyu Chun, "Possible suppression of partial electronic conductivity of CeO₂-based electrolytes by electron traps," *ECS Transactions* **25** (2009) 1583-1592
2. Han-Il Yoo, Sang-Hyun Park and Jakyu Chun, "Suppression of electronic conductivity of CeO₂-based electrolytes by electron traps," *Journal of the Electrochemical Society* **157** (2010) B215-B219
3. Jakyu Chun and Han-Il Yoo, "Electric-field induced degradation of ionic solids," *Journal of the Korean Ceramic Society*, **49** (2012) 48-55
4. Jakyu Chun, Manfred Martin and Han-Il Yoo, "Electrotransport-induced unmixing and decomposition of ternary oxides," *Journal of Applied Physics* **117** (2015) 124504

(2) List of Presentations

1. Jakyu Chun and Han-Il Yoo, "Suppression of electronic conductivity of CeO₂-based electrolytes by electron traps," The 6th International Conference on Flow Dynamics, Sendai, Japan, Nov. 4th~Nov. 6th, 2009 (oral)
2. Jakyu Chun, Sang-Hyun Park and Han-Il Yoo, "Suppression of electronic conductivity of CeO₂-based electrolytes by electron traps," The Fall Meeting of the Korean Ceramic Society, Daejeon, Korea, Oct. 19th~20th, 2009 (oral)
3. Jakyu Chun, "The effect of electric field on the formation and decomposition of ternary compounds," The 13th Korean-Japan Students' Symposium, Seoul, Korea, Nov. 7th~9th, 2012 (oral)
4. Jakyu Chun and Han-Il Yoo, "Electric-field effect on decomposition and formation of ternary compounds," The 19th International Conference on Solid State Ionics, Kyoto, Japan, Jun. 2nd~7th, 2013 (poster)
5. Jakyu Chun, Manfred Martin and Han-Il Yoo, "Kinetic unmixing and decomposition in ternary oxides under electric field," The 20th International

Conference on Solid State Ionics, Keystone, Colorado, USA, Jun. 13th~19th, 2015
(poster)

한글 초록

고체산화물 연료전지 (SOFC), 다중층 세라믹 축전체 (MLCC), 열전재료 등의 형태로 산업 전반에서 사용되고 있는, 삼성분계 산화물 등의 다성분 물질이 구동 조건 하에 놓이게 되면 (즉 구동력 하에 놓이게 되면) 동역학적 조성분리 또는 상분리 같은 열화 현상이 일어난다. 이 현상들은 그 기원을 구성 양이온들의 확산 계수 (또는 이동도) 차이에 두고 있다. 그 화합물이 열역학적으로 안정한 영역에 있다고 해도 이런 종류의 조성분리와 상분리는 여전히 일어날 수 있으며 그 화합물이 전해질이건 반도체 물질이건 상관없이 일어날 수 있다. 현상들의 원인이 확산 계수의 차이이기 때문에 이 현상들은 “동역학적”이라고 부른다.

산소분압 물매 하에서의 동역학적 조성분리에 대해서는 많은 연구가 진행되어왔다. 산소분압 물매 하에서의 동역학적 상분리와 전기장 하에서의 조성분리에 대해서는 더 적은 수의 연구가 진행되었지만 전기장 하에서의 상분리에 대해서는 지금까지 보고된 바가 없다. Yoo 등이 BaTiO_3 에 대해서 보고한 바에 의하면 큰 크기의 전기장이 걸린 경우에도 동역학적 조성분리 및 상분리는 일어나지 않았다. 따라서 다음 사항들에 대해 질문을 가질 수 있다: (i) 전기장 하에서 동역학적 조성분리 및 상분리가 실제로 일어나는가 (ii) 만일 일어난다면 이 현상들은 항상 일어나는 것인가 아니면 일정한 조건을 만족해야만 일어날 수 있는가. 이런 연구 및 분석은 지금까지 전기장 하에서는 이루어진 바가 없다. 또한, 전기장이 이 현상들에만 영향을 미치는 것은 아니다. 오히려 상분리의 역반응인 형성 반응 같은 다른 현상에도 2차 구동력으로 (1차 구동력은 구성 성분의 화학포텐셜 물매) 영향을 줄 수 있다. 따라서 전기장 하에서의 형성 반응의 속도론 측면에서의 분석 역시 이루어져야 한다.

이런 질문들에 답하기 위해, 모델 삼성분계 물질계를 선택하였다. 모델 물질계로는 1300°C , 공기 분위기에서 NiO-TiO_2 계의 유일한 중간화합물인

NiTiO₃를 선택하였다. 판형(板形) NiTiO₃ 시편에 정전류를 가했으며 가한 정전류는 별도의 실험을 통해서 구한 NiTiO₃의 전기전도도 값을 이용하여 가한 전압 값으로 변환하였다. 시편들에는 각기 다른 크기의 정전류를 가했다. 어떤 일정한 크기의 전류 이하를 가해준 시편들의 경우는 조성분리만 일어났으며 그 이상을 가해준 시편들의 경우는 조성분리와 상분리가 모두 관찰되었다. 분석을 위해서 전자탐침미세분석 (EPMA)을 이용해서 농도 분포를 양극에서부터 음극까지 측정하였다. 전극 극부에는 X선 회절분석 (XRD)을 이용하여 상분리로 생성된 NiO와 TiO₂가 존재하는지 확인하였다. 전자탐침미세분석과 X선 회절분석 모두 조성분리와 상분리를 확증하였다.

주어진 화합물의 열화 현상을 이해하는데에는 임계 전압 (혹은 분해 전압) U_d 를 수학적으로 표현한 식의 존재가 중요하며 이 논문에서 유도되었다. 유도하는 과정에서 정류 상태 (steady state)와 닫힌 회로 조건 (closed circuit condition)의 두 조건을 사용하였다. 결과로 유도된 식은 예측했던 바와 같이 양이온 A와 B의 확산 계수의 비율이 U_d 를 결정하는데에 있어 중요한 인자로 작용함을 나타낸다. 이 비율을 얻기 위해서 NiO-TiO₂ 확산쌍을 만들었으며 동시에 열처리 전의 NiO/TiO₂ 초기 계면에 백금 비활성 표시자 (inert marker)를 발라놓았다. 열처리 후 비활성 표시자로부터 각각의 계면 (NiO/NiTiO₃, NiTiO₃/TiO₂)까지의 거리의 비율이 양이온들의 확산 계수의 비율이 된다. 확산쌍 실험으로부터 확산 계수의 비율 $D_B/D_A=0.21\pm 0.07$ 을 얻을 수 있었다. 조성분리/상분리 실험으로부터 얻은 U_d 와 이론 식으로부터 얻은 U_d 는 오차범위 내에서 합치했으며 이는 이론 식이 실제로 합당하다는 것을 의미한다. 또한, 앞서 언급했던 BaTiO₃의 경우 왜 특이한 거동을 보였는지에 대한 가능성 있는 이유들도 제안했다.

형성 반응에 미치는 전기장의 영향의 경우 그 이론 식은 Korte 등에 의해 유도되었지만 그 실험적인 증명은 주어지지 않았다. 따라서 본 논문에서는 전기장 하에서의 형성 반응의 속도론 및 미세구조 변화에 대한 정량적인 분석이 시도되었다. 형성된 생성물 층의 두께와 그 미세구조가 전기장에 의해 크게 영향을 받음을 볼 수 있었으며, 이는 산업의 측면에서 다양하게 응용

될 수 있는 부분이다.

키워드: 동역학적 조성분리, 동역학적 상분리, 양이온 이동도 (확산계수), 분해 전압, 삼성분계 ABO_3 화합물, 전기장, 형성 반응

학번: 2008-20680